MANIPULATION AND DETECTION OF ATOMS USING PLASMON-ENHANCED EVANESCENT WAVES OVER DIELECTRIC WAVEGUIDES

JOHNATHAN YIK

CENTRE FOR QUANTUM TECHNOLOGIES,

NATIONAL UNIVERSITY OF SINGAPORE

2015

THANKS AND ACKNOWLEDGEMENTS

This thesis was completed with the assistance and support of many people, without whom much of the work described here would not be possible.

Thanks should first go to my supervisors, Assoc. Prof. Bjorn Hessmo of the Centre for Quantum Technologies at the National University of Singapore, and Dr. Liew Yun Fook, of the National Metrology Centre in Singapore, firstly for their guidance during the writing of this thesis, and also for their support in obtaining the resources needed to finally complete the work described here.

Thanks also go to Dr. Chu Hong Son, of the Institute of High Performance Computing, for his assistance and advice on carrying out computational simulations of plasmonic structures, and his valuable instruction in operating the FDTD-Solutions software used to perform those simulations.

Most of all, thanks go to my parents, for their support over the years, and for their patience with many late nights, and holidays and weekends spent working, and far too much stress that I've been responsible for over the course of this PhD.

Contents

ABSTRACT

Atom chip devices confine atoms by using the superposition of magnetic fields due to a current along with a uniform external field, generating a linear magnetic potential well along the line of the current. These devices are used in atomic physics experiments due to their ability to produce extremely tight confinements. In particular, the high phase-space densities made available by tight confinements allow rapid creation of Bose-Einstein condensates, while the strength of the transverse confinement compared to the weak axial confinement allows 1-dimensional states of matter to be created and studied. To achieve such tight confinements, atoms must be trapped very close to the chip surface. However, detection of atoms is difficult at small separations from the surface. Additionally, irregularities in the current-carrying wires produce corrugations in the trapping potential, causing fragmentation of trapped atoms, as well as undesired excitations out of the ground state. In this thesis, the integration of optical waveguides on the surface of atom chips is proposed, in order to address the previously-mentioned problems with atom confinement near the chip surface. Using evanescent waves enhanced by metal wires emplaced on the waveguide surface, atoms may be detected via fluorescence imaging, or trapped using induced dipole potentials from oppositely detuned wavelengths of light coupled through the guide.

We report the results of finite-difference time-domain simulations of metal wires embedded on waveguide surfaces. Enhanced evanescent waves due to surface plasmons excited within the wires are calculated. The use of

these waves to carry out fluorescent imaging of atoms over the chip surface is examined. Fluorescent rates are calculated for the 5s-5p transition in rubidium, as well as the two-photon transition between the 5s and 4d states. In addition to this, we examine the dipole forces acting on atoms above the wires, in particular, of forces acting in opposite directions due to two oppositely-detuned wavelengths coupled down the same guide. By tuning the relative powers of the two modes, it is found possible to achieve a long, narrow trapping potential over the waveguide. Finally, we examine the use of such a trap for creating and manipulating 1-dimensional states of matter, in particular, the creation of 1-dimensional strings of impenetrable atoms, also known as Tonks-Girardeau gases, and compare the characteristics of such a gas created in the evanescent-wave dipole trap to previous experiments making use of crossed-beam optical lattice potentials.

List of Figures

1. INTRODUCTION

An atom chip is a device made up of several thin wires laid down on the surface of a wafer of silicon or some other substrate, in which the superposition of the magnetic field produced by current flowing through the wires, and a uniform external magnetic field, creates an elongated magnetic potential well, above and parallel to the chip wires, capable of confining neutral atoms. This potential well posesses high trapping frequencies in the transverse direction, while requiring only small amounts of power to maintain [1]. Such high trapping frequencies result in widely-separated energy levels of bound quantum states, and are thus useful for investigating highly-cooled states of matter. More precisely, the high trapping frequencies made available by atom chips allow rapid creation of Bose-Einstein condensates, in which a macroscopic population of bosonic atoms is cooled into the ground state, and begins to exhibit wave-like behaviour [2, 3].

Through careful arrangement of the wires on the chip, it is possible to implement various devices on the chip surface for the purpose of further interacting with the trapped condensate. Such devices include magnetic waveguides down which the matter wave is allowed to propagate [4–6]; atomic beam splitters for dividing the propagating matter wave [5, 7, 8]; magnetic conveyor belts capable of moving, splitting and recombining clouds of trapped atoms [9–11]; matter wave Michelson interferometers [12–14]; and magnetic diffraction gratings through which matter waves may be diffracted [15].

The high transverse trapping frequencies associated with atom chip po-

tential wells also enable the creation of more exotic states of matter. Where the transverse confinement of an atom chip trap is much greater than the axial confinement, it becomes possible to create 1-dimensional atom gases. The state of such gases is furthermore dependent on the ratio between the axial kinetic energies and the interatomic potential energies of the gas, characterised by the dimensionless parameter γ [16]. The ratio between the kinetic and interatomic potential energies in turn depends on the relative strengths of the transverse and axial trapping frequencies. These frequencies are easily adjusted over an atom chip, simply by tuning the strengths of the current through the wires and/or the external bias field. Taking advantage of this, experiments have prepared 1-dimensional gases over atom chips at varying values of γ, from a weakly-interacting state resembling an ideal Bose gas at very low γ, to a quasicondensate state at slightly higher γ in which density fluctuations are suppressed due to the slightly stronger interactions between atoms [17], to a state with even stronger interactions, in which density fluctuations are even more strongly suppressed [18]. The use of atom chips to attain even higher values of γ, entering the regime where the 1-dimensional gas forms the state of matter known as the Tonks-Girardeau gas, has also been proposed [19].

As the transverse trapping frequency of an atom chip potential increases, the height of the trapping potential over the surface of the chip becomes smaller. As the trap approaches the chip surface, corrugations begin to appear and grow at the bottom of the trapping potential [4, 20–22]. In turn, the presence of these corrugations induces undesirable effects on the atom cloud inside the potential. Such effects include fragmentation of the atom cloud [20, 21], excitation of atoms out of the ground state [4], or even the removal entirely of atoms from the trapping potential [20, 21]. These effects, however, can be overcome by the introduction of a rapid modulation to the

chip current [23], and by making use of advanced fabrication techniques [24] to minimise the imperfections in the wire causing such corrugations [25]. Using these techniques, atoms have been trapped in tight transverse potentials as low as 15 μm over the chip surface [18].

Detection of atoms above a chip is carried by illuminating the cloud with beams of laser light. The frequency of the incident light is chosen to be resonant with transitions of the trapped atoms. As the light passes through the atom cloud, photons are absorbed and then re-emitted in random directions via spontaneous emission. Atoms can then be detected by photographing the shadow left by photons scattered out of the beam. Alternatively, using an objective lens, or some other collector connected to a photon counter, scattered photons may be collected and detected, indicating the presence of atoms inside the detection region [26, 27].

For the purpose of detecting large clouds of atoms, atoms may be illuminated using wide, collimated beams of light and imaged using regular CCD cameras. To interact with atoms within the cloud on a finer scale, however, more precise tools are required. One means of acquiring such tools for the purpose of carrying out atomic physics experiments is to make use of optical components integrated onto the surface of the chip itself.

For the purpose of detecting trapped atoms, optical components have previously been integrated with atom chips in the form of optical fibres emplaced on the chip surface [28–33]. Absorption imaging of atoms was carried out by Quinto-Su *et. al.* [32], by measuring the attenuation of light coupled from the tip of a lensed fibre into the open end of a second fibre several millimetres away caused by atoms passing between the fibre tips. Using this method, atom clouds containing approximately 600 atoms were detected, with a lower limit on the size of the atom cloud being estimated at 100 atoms. A more refined detector using the same technique was implemented by Eriksson *et.*

al. [33], using two opposing tapered fibres mounted in silicon grooves to focus light into a much smaller volume, thus allowing much smaller atom clouds (on the order of 5-10 atoms in size) to be detected.

Using fluorescent imaging techniques, integrated-fibre devices capable of efficiently detecting single atoms were also implemented by Heine [29, 31] and Wilzbach [30] *et. al.*. In the experiments by these authors, light is focused from a tapered fibre into a very narrow spot size above a wire trap. Atoms passing through the spot scatter photons via spontaneous emission, which are then collected by a multi-mode fibre to be detected using a photon counter. In addition to achieving even higher detection efficiencies than [33], fluorescent integrated-fibre devices do not require coupling of light between the input and output fibres, and therefore may be constructed without the need for precise positioning of both fibres seen in [32] and [33].

While efficient detection of single atoms has been achieved in [29–31] using tightly-focused light from a tapered fibre, the region in which atoms may be detected using this method is constrained by the dimensions of the fibre. More precisely, it is not possible to detect atoms held closer to the surface of the chip than the centre of the fibre using this method. One objective of this thesis, therefore, is to investigate the use of evanescent waves of light travelling through dielectric waveguides to induce fluorescence in atoms. Such waveguides may be fabricated at any height above the chip surface, in particular, at heights smaller than the radius of the tapered fibre. By fabricating waveguide atom detectors on the atom chip surface at the desired height, atoms held lower than the radius of the optical fibre may be detected.

Another use for integrated optical components on atom chips is inspired by the use of dipole forces induced by strong evanescent waves around ultra-thin optical fibres to trap atoms around those fibres [34–36]. Of particular

interest is the use of evanescent fields from two oppositely-detuned wavelengths coupled down the same fiber to induce opposing dipole forces on the same atom, thereby creating an annular potential well centred on the fibre [34, 35]. Similarly, another goal of this thesis is the realisation of a tight, *linear* potential well using the evanescent waves of oppositely-detuned modes coupled down a waveguide emplaced on an atom chip. As in the case of the evanescent-wave atom detector, this waveguide dipole trap may be integrated with the surface of an atom chip. Here, magnetic fields generated by chip wires may be used to manipulate atoms within the trap.

Of particular interest to this thesis is the axial confinement of atoms within the 1-dimensional trap via magnetic potentials, and the ability to tune the relative strengths of the kinetic and interaction energies between the atoms by expanding the size of that axial confinement. By adjusting the relative strengths of the kinetic and interaction energies, it is possible to induce a phase shift in the trapped atoms from a three-dimensional condensate to a 1-dimensional gas of impenetrable atoms [37]. This form of matter, first described by Girardeau [38], has only previously been created using arrays of elongated potential wells generated using optical lattices [39–41].

Large arrays of 1-dimensional potential wells were created by Paredes *et. al.* [40] by intersecting the standing waves of two beams of red-detuned light at right angles. The effective interaction energies of atoms trapped within these wells were then tuned by ramping up a third red-detuned standing wave along the long axes of these potential. Using this method, Paredes *et. al.* were able to to increase the interaction to kinetic energy ratio sufficiently that a Tonks-Girardeau gas was formed.

An alternate approach to creating large arrays of 1-dimensional potential wells was taken by Kinoshita *et. al.* [39]. Here, standing waves of two beams of *blue*-detuned light were intersected. Using this procedure, 1-dimensional

potential wells were formed around the points where the nodes of both standing waves intersected, as opposed to the antinodes in the case of Paredes. The resulting potential wells were much tighter than those created using the red-detuned light, and thus, formation of a Tonks-Girardeau gas was achieved simply by ramping up the crossed-beam array around a previously-trapped atom cloud.

Finally, Tonks-Girardeau gases were achieved in the work of Haller *et. al.* [41] by tuning the interaction strength of the atoms using Feschbach resonances. Using these resonances, atoms in a 1-dimensional trap were first transformed from a non-interacting, quasi-condensate state into a Tonks-Girardeau gas with strong repulsive interatomic interactions. Again using Feschbach resonances, the sign of the atomic interaction was reversed, transforming the ordinary Tonks-Girardeau gas into a metastable state known as the super Tonks-Girardeau gas, which retains the structure of the Tonks-Girardeau gas even while the atomic interactions become attractive rather than repulsive.

The experiments described in [40], [39] and [41] make use of 1-dimensional potential wells created by crossing standing-wave beams at right angles. By necessity, each experiment therefore creates and makes use of large arrays of such wells. In experiments where such arrays are used, measurements are therefore taken as averages over the entire ensemble of 1-dimensional gases. It is therefore not possible to study quantities associated with a single example of a Tonks-Girardeau gas, such as the density distribution and interatomic correlations, using such an experimental set up.

By use of the waveguide dipole trap, a single example of this state of matter can be created and studied in isolation. In particular, not only may the quantities mentioned above be easily measured, but it is also possible, using this device, to examine the transition of the atoms from the condensate

to the 1-dimensional gas of impenetrable atoms.

In summary, in this thesis, we investigate the integration of optical components comprised of dielectric waveguides on atom chip surfaces for two purposes. Firstly, we propose a device capable of detecting atoms within a small region via fluorescence. As the region illuminated by this device is small, it is believed that our device may be capable of detecting single atoms. Furthermore, as waveguides may be fabricated on the surface of the chip at any given height, such a detector is not subject to the constraints imposed by the radius of the optical fibre to which fibre-based detectors are susceptible. Secondly, using the same device, we propose an evanescent wave-based dipole trapping potential capable of achieving high transverse confinements similar to those theoretically available using an atom chip, while avoiding the previously-mentioned issues with corrugation of the potential well associated with confinement close to the surface of the atom chip, and investigate the feasibility of using this device to create 1-dimensional gases similar to those observed by [39–41].

The outline of this thesis is as follows:

In Chapter 2, the background to the research performed for this thesis is discussed, including a short discussion of the atom chip, the ways in which these devices are useful for carrying out experiments on cold atoms, and the rationale for integrating optical components with them. As an introduction to a potential application of such optical components, we then briefly discuss some methods of detecting atoms held inside an atom trap. An introduction to optical waveguides–the basic component of the sort of optical devices this thesis is intended to explore–is given, including a brief digression on materials used to construct such devices, which in turn influence the choice of parameters for the simulations carried out in this thesis. Finally, we discuss shortly the theory behind surface plasmon polaritions on metal structures,

which may be used to enhance the evanescent wave above the waveguide surface. In the context of this thesis, the enhanced evanescent waves over such structures enable the effective coupling of light to trapped atoms, and thus are fundamental to the applications of optical devices proposed here.

In Chapter 3, the methods used to carry out the simulations used in this thesis are discussed. Trial modes of a rectangular waveguide are generated using 1-dimensional solutions of the Maxwell wave equation. These modes are then propagated down finite-difference time-domain(FDTD) simulations of the waveguide, and the change in the mode shape as it travels down the guide is observed. Eigenmodes are extracted from the simulation when the shape of the mode stabilizes. Next, FDTD simulations of metal wires emplaced along the centerline of dielectric waveguides are described. From these calculations, the enhanced evanescent wave produced by such structures is calculated.

In Chapter 4, the results of the simulations described in the previous chapter are discussed. Methods used to monitor the change of the mode shape as it propagates through the guide are described. Changes in the mode shape are analysed for waveguides of different dimensions. From these results, we obtain estimates for the minimum dimensions of a square waveguide capable of supporting a confined mode. Next, we analyse the effects of the metallic wire above the waveguide. In particular, we analyse the enhancement of fluorescence of the 5s-5p transition in rubidium due to the presence of the enhanced evanescent wave.

In Chapter 5, a possible application of enhanced evanescent fields over waveguides is explored. A dipole force trap is created out of evanescent waves of two modes coupled down the same waveguide, each detuned in opposite directions from the 780nm transition of rubidium. The trapping frequencies associated with the resulting potential well are calculated. Using a harmonic approximation for the energy levels of bound states within the

well, the energy levels of the ground states are estimated, and in turn used to estimate whether or not trapping is possible in the potential well.

Finally, in Chapter 6, the applicability of the enhanced evanescent wave device to other purposes is discussed. The use of the enhanced evanescent wave to excite multiple-photon transitions is explored. Rates of fluorescence are calculated for the two-photon absorption between the 5s and 4d states. From these calculations, we analyse the feasibility of carrying out fluorescent detection of atoms using this transitions. We then conclude the chapter by analysing the characteristics of atoms trapped in the potential well discussed in Chapter 5, focusing on the relationship between the transverse trapping frequencies of the potential and the 1-dimensional scattering length between atoms. We discuss the possibility of using such potentials to achieve a 1-dimensional state of matter–the Tonks-Giraredeau gas, and compare the expected parameters of such a gas created in the evanescent wave dipole trap with values obtained from previous experiments using crossed-beam optical lattice potentials.

2. THEORY AND BACKGROUND

2.1 An introduction to the atom chip

2.1.1 Physics of the atom chip

An atom possessing a magnetic moment $\vec{\mu}$ experiences a potential V, given by:

$$V = -\vec{\mu} \cdot \vec{B}, \tag{2.1}$$

where $\vec{\mu} = \mu_B g_F \vec{F}$, and μ_B is the Bohr magneton, g_F is the Landé g-factor, and $\vec{F}$ is the total atomic spin.

Where the motion of the atom relative to the magnetic field is slow, the direction of $\vec{F}$ follows the direction of $\vec{B}$. In this limit of adiabatic motion relative to the field, the potential experienced by the atom then becomes:

$$V = \mu_B g_F m_F |\vec{B}| \tag{2.2}$$

Atom chips are devices that generate magnetic fields for trapping neutral atoms. A typical atom chip consists of a simple pattern of wires laid down on top of a substrate. Passing current through the wires generates a magnetic field according to the Biot-Savart law for infinitely thin wires,

$$B(\vec{r}) = \frac{\mu_0 I}{4\pi} \int \frac{d\vec{l} \times (\vec{l} - \vec{r})}{|\vec{l} - \vec{r}|^3}, \tag{2.3}$$

where $|\vec{l}|$ is the length of the wire. Suppose that our chip consists of a long,

thin, straight wire stretching from one edge of a substrate to the other. The magnetic field due to the current passing through the wire then becomes:

$$B = \frac{\mu_0 I}{2\pi r} \tag{2.4}$$

This chip is then placed within a uniform, external magnetic field, parallel to the plane of the substrate and perpendicular to the wire. The uniform field will then cancel out the field generated by the current passing through the wire at a height

$$\rho_0 = \frac{\mu_0 I}{2\pi B_{ext}} \tag{2.5}$$

where B_{ext} is the strength of the external field, and ρ_0 is the height of the minima above the chip surface. The resulting field minimum extends along the entire length of the wire. The fields surrounding this minima generate a potential around the minima confining the atoms to its vicinity.

The shape of the potential can be changed by varying the pattern of the wire on the chip. To create a well of a given length, for example, one may bend the wire into a U-shape, with the centre of the U at the desired length, and the legs of the U parallel to the external field [9, 42].

Atoms in potentials with minima at zero are susceptible to being ejected from the trap via Majorana spin-flip transitions. At the zero-point of the potential, the direction of the field reverses abruptly. This results in a non-adiabatic change in the field experienced by the particle which can induce the particle's spin relative to the field to reverse, transforming the attractive magnetic potential into a repulsive one. To minimise loss of atoms from magnetic traps, a bias field parallel to the central wire is introduced. On an atom chip, this can be accomplished by bending the wire into a Z-shape, instead of a U [9, 42, 43].

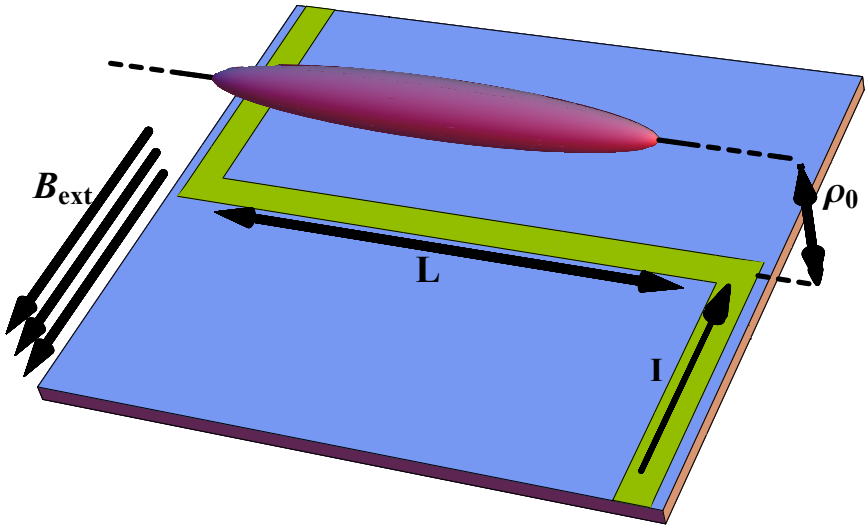

Fig. 2.1: A simplified drawing of a z-shaped atom chip trap. A wire laid down on a silicon substrate is bent into a z-shape, where the portion of the wire that forms the middle of the z is of length L. A current I is passed through the wire, and the chip is placed within a uniform external magnetic field of strength B_{ext}. A potential well is formed by superposition of the current magnetic field and the external field at a distance ρ_0 given by Eq.(2.5).

The magnetic field strength at the trap bottom then becomes: [42]:

$$B_0 = \frac{4\mu_0}{\pi} \frac{I\rho_0}{4\rho_0^2 + L^2} \tag{2.6}$$

where L is the length of the trap. Assuming $\rho_0 \ll L$, we can assume this value remains relatively constant around the bottom of the potential well.

Near the centre of the well, the magnetic field strength is approximated by a Taylor series:

$$B(\rho) = B_0 + \frac{B''(\rho_0)}{2}\rho^2 + \dots \tag{2.7}$$

where ρ is the radial coordinate from the centre of the well, ρ_0, and $B''(\rho_0)$ is the second derivative of the magnetic field strength at the well centre.

Assuming higher powers of ρ are negligible, the resulting scalar potential is:

$$V = \mu_B g m_F (B_0 + \frac{B''(\rho_0)}{2}\rho^2) \tag{2.8}$$

The form of this potential is characteristic of a simple harmonic oscillator. A particle within this potential will oscillate about the axis of the trap with a frequency

$$\omega_\perp = \sqrt{\frac{\mu_B g m_F B''(\rho_0)}{m}} \tag{2.9}$$

where m is the mass of the particle. One may then write the potential V as

$$V = \frac{1}{2} m {\omega_\perp}^2 \rho^2 \tag{2.10}$$

By writing:

$$B(\rho) = \sqrt{\left(\frac{\mu_0 I}{2\pi\rho} - \frac{\mu_0 I}{2\pi\rho_0}\right)^2 + {B_0}^2}, \tag{2.11}$$

carrying out the second differentiation with respect to ρ, and finally substituting ρ_0 into ρ, we obtain:

$$\frac{d^2B}{d\rho^2}|_{\rho=\rho_0} = \frac{\mu_0}{16\pi}\frac{I(L^2 + 4\rho_0^2)}{\rho_0^5} \tag{2.12}$$

which becomes, in the limit $L \gg \rho_0$,

$$\frac{d^2B}{d\rho^2}|_{\rho=\rho_0} \simeq 2B_{ext}^5 L^2 (\frac{\pi}{\mu_0 I})^4 \tag{2.13}$$

It can be seen from these equations that the frequency of oscillation varies proportionately with $B_{ext}^{5/2}$ and inversely with I^2. With a strong external field interacting with a small current, large values of $d^2B/d\rho^2$, and thus high $\omega_\perp$, can be created.

Along the axis of the potential well, the magnetic field varies as:

$$B(z) = \frac{\mu_0 I}{4\pi}\left[\left(\frac{(L/2+z)}{(L/2+z)^2+{\rho_0}^2} - \frac{L/2-z}{(L/2-z)^2+{\rho_0}^2}\right)^2 + \left(\frac{\rho_0}{(L/2+z)^2+{\rho_0}^2} + \frac{\rho_0}{(L/2-z)^2+{\rho_0}^2}\right)^2\right]^{\frac{1}{2}}, \quad (2.14)$$

taking the centre of the wire to be at $z_0 = 0$. Again, performing second differentiation with respect to z, one obtains:

$$\frac{d^2B}{dz^2}|_{z=z_0} = \frac{\mu_0 I}{4\pi}\frac{8(L^4+16L^2{\rho_0}^2-16{\rho_0}^4)}{\rho_0(L^2+4{\rho_0}^2)^3}, \quad (2.15)$$

which again, in the limit $L \gg \rho_0$, becomes:

$$\frac{d^2B}{dz^2}|_{z=z_0} \simeq \frac{4B_{ext}}{L^2} \quad (2.16)$$

From Eqs.(2.13) and (2.16) it can be seen that, in the limit $L \gg \rho_0$, $(d^2B/d\rho^2)|_{\rho=\rho_0} \gg (d^2B/dz^2)|_{z=z_0}$. In turn, this means that the trapping frequency of the magnetic potential well in the transverse plane is much greater than the frequency of the same well in the axial direction.

2.1.2 Applications, advantages and limitations of atom chips

As seen in Eq.(2.13), very high trap frequencies, allowing very tight confinements of atoms, are achievable using atom chip traps. By ramping up the external magnetic field, it is thus possible to compress a gas of trapped atoms to high densities, with correspondingly high rates of collision between atoms. This allows rethermalisation of the gas to take place rapidly after radio-frequency evaporation is carried out, which in turn enables rapid cooling of the gas into a Bose-Einstein condensate [3]. Similarly, by increasing

the transverse confinement of the trap relative to the axial confinement, it is possible to create and manipulate the state of a 1-dimensional gas of neutral atoms. Thus, atom chips have also been found useful for the investigation of 1-dimensional states of matter [17, 18, 44].

From Eq.(2.5), increasing the external field brings the bottom of the potential well closer to the surface of the chip. Hence, in order to obtain high trapping frequencies, it is conversely necessary for the atoms to be brought closer to the surface. Experimentally, tight trapping of 1-dimensional atom gases over an atom chip has been achieved with atom-to-surface distances as low as 15 μm [18].

As mentioned in the previous chapter, the concern of this thesis is with manipulating and interacting with atoms held very close to atom chip surfaces. In subsequent sections, therefore, the use of optical components integrated with the chip surface to interact with such atoms will be explored–in particular, the use of dielectric waveguides fabricated directly on the chip surface to transport light to trapped atoms, and the use of plasmonic structures emplaced on waveguides to enhance the coupling between light travelling through the guide and atoms trapped directly over the same guide. To properly begin the discussion, however, it is necessary to start first with the uses of light in interacting with trapped atoms.

2.2 Detection of trapped atoms on a chip

2.2.1 Interacting atoms and light

Having acquired a cloud of trapped atoms, it is then desirable to extract some meaningful scientific data from it. This is in turn accomplished by measuring the interaction of the atom cloud with beams of incident light. The strength of this interaction is characterised by the scattering cross-section,

which represents the probability that an incident photon scattering off an atom. For incident light at frequency ω, the scattering cross-section is given by:

$$\sigma = \frac{\sigma_0}{1 + 4\Delta^2} \tag{2.17}$$

where $\sigma_0 = 3\lambda^2/2\pi$ is the scattering cross-section of light resonant to the atomic transition with wavelength λ_0 and corresponding frequency ω_0, and $\Delta = (\omega - \omega_0)/\Gamma$ is the detuning of the incident light normalised to the atomic linewidth Γ.

From Eq.(2.17), it can be seen that as the frequency of incident light ω diverges from ω_0, the scattering cross-section decreases with the square of the detuning. The scattering cross-section, and hence the strength of the atom-light interaction, is therefore strongest where the incident light is resonant with an atomic transition of wavelength λ_0.

2.2.2 Absorption imaging of trapped atoms

In typical atom chip experiments, involving large numbers of atoms, detection of the atom cloud is performed by measuring the absorption of resonant light passing through the atom cloud [26, 45]. By capturing images of an empty beam of light with a camera and comparing them with images where atoms have been trapped inside the cloud, it is possible to determine the change in intensity of the beam as it passes through an atom cloud, and thus the column density of atoms in the cloud [45]:

$$\frac{I_{att}}{I_0} = e^{-\rho_{at}\sigma_0} \tag{2.18}$$

where ρ_{at} is the column density of the atom cloud, σ_0 is the scattering cross-section of the atoms in resonant light, I_{att} is the intensity of light attenuated

by passing through the cloud of atoms, and I_0 is the intensity of the unattenuated light. Using this technique, light reaching the camera is attenuated according to the thickness of the atom cloud through which it has passed. The picture captured by the camera thus forms a density profile of the cloud over space.

The precision of such intensity measurements is given by the signal-to-noise ratio. For a measurement of the intensity of an attenuated beam passing through a cloud of atoms, this quantity is given by:

$$SNR = \sqrt{j_{in}\tau}\frac{1-\exp(-\rho_{at}\sigma_0)}{\sqrt{\exp(-\rho_{at}\sigma_0)}} \tag{2.19}$$

where j_{in} is the incoming photon flux experienced by the atom and τ is the duration of the imaging pulse.

From Eq.(2.19), it can be seen that the signal-to-noise ratio for detection of trapped atoms using absorption imaging is largest where ρ_{at} is also large. Conversely, in the limit where ρ_{at} is small, the signal to noise ratio approximates to $SNR \simeq \sqrt{j_{in}\tau}\rho_{at}\sigma_0$. For sufficiently small ρ_{at}, therefore, the signal to noise ratio approaches zero, and no useful information can be obtained using absorption imaging.

As mentioned in the previous chapter, part of the intention of this thesis is to investigate devices capable of holding and detecting the 1-dimensional state of matter known as the Tonks-Girardeau gas. Such a gas is created when the interaction strength between atoms is large compared to the total kinetic energy of the system. As will be explained in Sec.(6.3), such conditions are achieved at very low atom densities. To image such a gas, therefore, a different method–one in which the accuracy of the image is not so strongly reliant on the density of the atoms–is desired. For small numbers of atoms,

fluorescent atom imaging appears to be a superior imaging method.[1]

2.2.3 Fluorescence imaging of trapped atoms on atom chips

Light that is absorbed by atoms in the path of an imaging beam is later released via spontaneous emission. This process is completely random, and photons emitted in this manner may emerge with equal probability along any direction. Using a microscope objective fitted to a camera, these photons can be captured to create an image of the atoms within the cloud, with a signal to noise ratio given by [28]:

$$SNR = \eta\sigma_0\sqrt{\frac{I\tau}{Af_b + \eta\sigma_0}} \tag{2.20}$$

where I is the intensity of incident light, σ_0 is the resonant scattering cross section, η is the number of collected photons, τ is the duration of the imaging pulse, A is the size of the region being imaged, and f_b is the fraction of light scattered from other objects within the beam. Depending on the microscope objective used, this method is therefore capable of high resolutions, being able to image single atoms on individual sites of optical lattices [27, 47, 48].

One method of conveying light to atoms for the purposes of fluorescent imaging is the use of optical fibres mounted on a chip surface. Using focused light from the tip of a tapered fibre, experiments as atom spectroscopy [31], density cross-sections of the atom cloud [31, 32], and correlation measurements of atoms within the cloud [29, 31] have been carried out. One limitation of this technique, however, is that the region accessible by the light is

[1] The signal-to-noise ratio of images taken using absorption imaging of atom clouds is high for large ρ_{at}. For sufficiently large ρ_{at}, however, it becomes possible that light travelling through the cloud is almost completely attenuated. Variations in the column density beyond this point are thus inaccessible using absorption imaging techniques. To image clouds with extremely high ρ_{at}, phase-shift techniques, such as those described in [46], are employed. As the ultimate focus of this thesis is on the detection of small atom clouds with low ρ_{at}, discussion of this method of imaging atom clouds has been limited to this footnote.

limited to the volume directly adjacent to the centre of the fibre tip. Tightly confined gases, which must be trapped closer to the chip surface, may not be illuminated in this manner. In the following section, we discuss a proposed device intended to address this issue, as well as the fragmentation of the atom gas caused by the roughening of the potential when atoms are trapped very close to the chip surface.

2.3 Optical waveguides on atom chips

Having noted the issues concerning the tight trapping of atoms close to the chip surface, and the detection of atoms by fluorescent imaging, this thesis intends to explore a proposed device similar to the aforementioned chip-mounted fibres that addresses these issues. Consider an optical waveguide mounted upon a chip surface. Light is carried to the vicinity of the trapped atoms by the waveguide,and illuminates and couples to those atoms by the evanescent wave along the exposed top surface of the waveguide. Where the wave is close to resonance, it excites electrons within the atoms, which then spontaneously decay, producing fluorescence. Conversely, if the wave is detuned from resonance sufficiently that the detuning greatly exceeds the Rabi frequency of the transition, the atoms then experience a potential inversely proportional to the strength of the detuning. Two waves detuned in opposite directions from the same transition exert opposite potentials on a single atom. When coupled through the same waveguide, the potentials arising from both waves can thus be combined to form a tight, transversely-confining potential well.

A waveguide consists of a core of high refractive index surrounded by materials with lower refractive indices. The amplitude of a monochromatic wave of light travelling through this guide is distributed over and around the

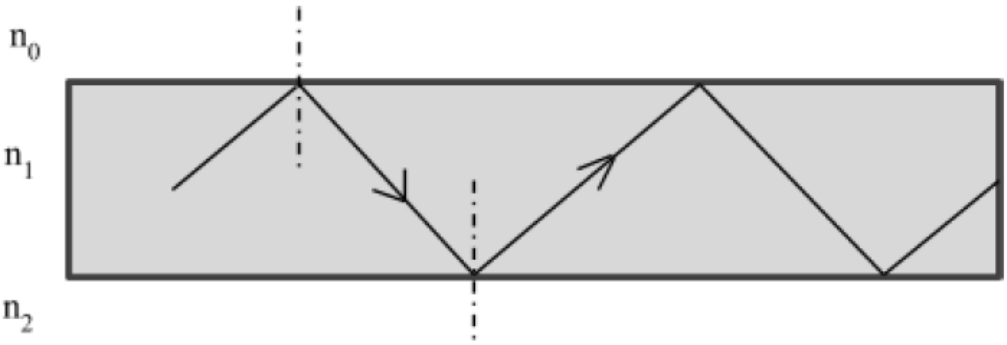

Fig. 2.2: A ray-optical representation of light propagating through a waveguide with refractive index n_1, surrounded on either side by materials with refractive indices n_0 and n_2, with $(n_0, n_2) < n_1$. Light incident on the boundary of the waveguide core (shaded in grey) undergoes total internal reflection, travelling back into the waveguide core until it hits the opposite boundary of the core, undergoing total internal reflection a second time. This process repeats itself indefinitely, or at least, until the light exits the end of the waveguide core

region of the waveguide core in a manner governed by the Maxwell Wave Equations:

$$(\nabla^2 - \frac{n(\mathbf{r})^2}{c^2}\frac{\partial^2}{\partial t^2})\mathbf{E} = 0, \tag{2.21}$$

$$(\nabla^2 - \frac{n(\mathbf{r})^2}{c^2}\frac{\partial^2}{\partial t^2})\mathbf{H} = 0, \tag{2.22}$$

where $n(\mathbf{r})$ is the refractive index at $\mathbf{r}$, the electric field $\mathbf{E}$ is of the form $\mathbf{E} = \mathbf{E}(x, y) \exp i(\beta z + \omega t)$, and the magnetic field $\mathbf{H}$ is of similar form to $\mathbf{E}$.

The solutions of this equation govern the shapes of modes travelling though a given waveguide, and depend strongly both on the optical properties of the core and its surrounding material, as well as the physical dimensions of said core. Moreover, where the optical properties of the material surrounding the guide are anisotropic, such as when the upper surface of a rectangular core is exposed to vacuum, a lower limit exists for the dimensions of the waveguide, beyond which confined solutions of Eq.(2.21) do not exist.

To produce waveguides capable of guiding light, it is therefore necessary to know the minimum size at which said solutions of Eq.(2.21) for confined modes exist. In this next section, we discuss a known method for deriving approximate solutions of this equation for rectangular waveguides, and its applicability to the conditions encountered in this thesis.

2.3.1 Analytical solutions of the rectangular waveguide.

By performing the second differentiation of z and t from Eq.(2.21), and then eliminating the periodic term from both sides of the result, the following eigenvalue equation is obtained.

$$({\nabla_{xy}}^2 + \frac{n(\mathbf{r})^2\omega^2}{c^2})E(x,y) = \beta^2 E(x,y), \tag{2.23}$$

No exact analytical solution exists for this equation in the case of a rectangular waveguide. For a waveguide in which the modes are well-confined, close approximations of two modes may be found using the methods described in [49]–one in which the dominant transverse components of the electromagnetic field are E_y and H_x, and another in which the dominant components of the field are E_x and H_y. The approximate solutions for the mode with E_y and H_x dominant are given below, with each index i referring to the approximate solution of the equation in the corresponding numbered region from Fig.(2.3a)[2]

[2] For this mode, small nonzero values of H_z, E_x and E_z also exist. These are however negligible compared to the H_x and E_y components, and thus have been ignored.

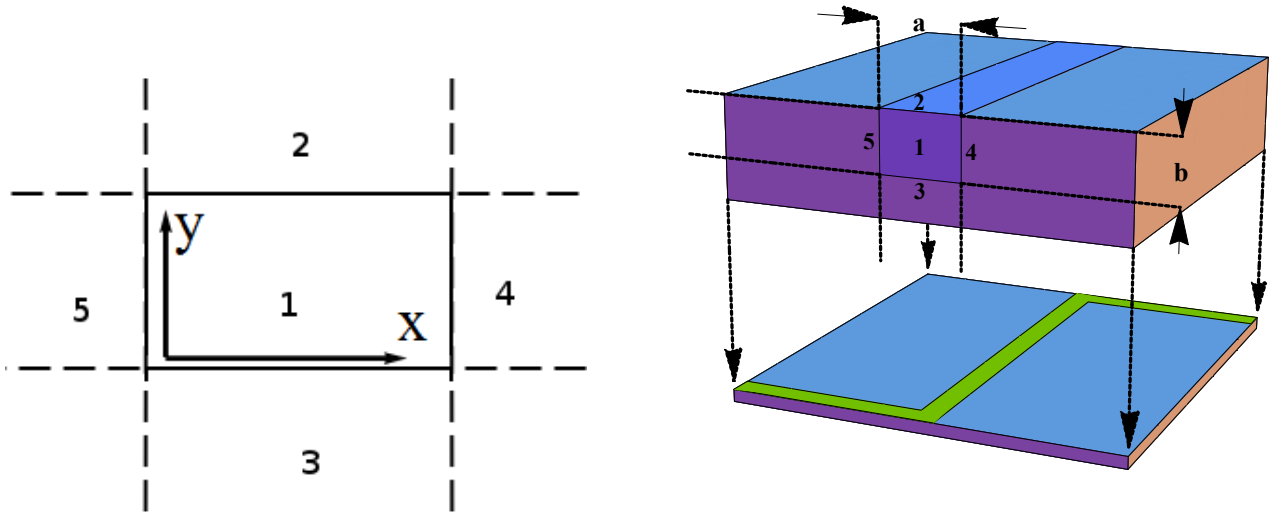

(a) (b)

Fig. 2.3: a). A cross-sectional representation of a rectangular waveguide surrounded on all four sides by materials with lower refractive indices. An analytical approximation for the modes of the waveguide is obtained by expressing those modes as the products from in Eq.(2.24), with each index i referring to the corresponding numbered region on the diagram. b). 3-D representation of a dielectric waveguide of width b and height a embedded in a cladding layer that is in turn laid over an atom chip, with the top surface of the waveguide exposed to vacuum. Regions analogous to those marked out in Fig.(2.3a) are themselves marked out round the waveguide edges.

$$H_x = \exp i(\beta z - \omega t) \begin{cases} M_1 \cos(k_{x1}x + \alpha)\cos(k_y y + \beta) \\ M_2 \cos(k_{x1}x + \alpha)\exp(ik_{y2}y) \\ M_3 \cos(k_{x1}x + \alpha)\exp(-ik_{y3}y) \\ M_4 \exp(ik_{x4}x)\cos(k_y y + \beta) \\ M_5 \exp(-ik_{x5}x)\cos(k_y y + \beta) \end{cases} \tag{2.24}$$

$$E_y = \frac{k^2 {n_i}^2 - {k_y}^2}{\omega \epsilon_0 {n_i}^2 k_z} H_x \tag{2.25}$$

Similarly, approximations for E_x and H_y can be found by substituting $H_x \to E_x$, $\epsilon_0 \to \mu_0$, and vice versa.

To find the transverse components of the wavevector for this waveguide,

electric and magnetic fields and field gradients are matched along the boundaries using the appropriate boundary conditions:

$$\epsilon_1 E_{\perp 1} = \epsilon_2 E_{\perp 2} \tag{2.26}$$

and

$$E_{\parallel 1} = E_{\parallel 2} \tag{2.27}$$

where ϵ_1 and ϵ_2 are the dielectric constants of the two media and $E_\perp$ and $E_\parallel$ are the perpendicular and tangential components of the electric field respectively, and:

$$\mu_1 H_{\perp 1} = \mu_2 H_{\perp 2} \tag{2.28}$$

and

$$H_{\parallel 1} = H_{\parallel 2} \tag{2.29}$$

where μ_1 and μ_2 are the permeabilities of the two media and $H_\perp$ and $H_\parallel$ are respectively the perpendicular and tangential components of the magnetic field.

In the case where E_y and H_x are dominant, the following equations for the horizontal and vertical components of the wave vector are obtained:

$$k_x a = \pi p - \tan^{-1} k_x \xi_4 - \tan^{-1} k_x \xi_5 \tag{2.30}$$

$$k_y b = \pi q - \tan^{-1} \frac{{n_3}^2}{{n_1}^2} k_y \eta_3 - \tan^{-1} \frac{{n_2}^2}{{n_1}^2} k_y \eta_2 \tag{2.31}$$

where p and q are the number of maxima of the electric field amplitude along the x- and y- axes respectively, a and b are the horizontal and vertical dimensions of the waveguide, and:

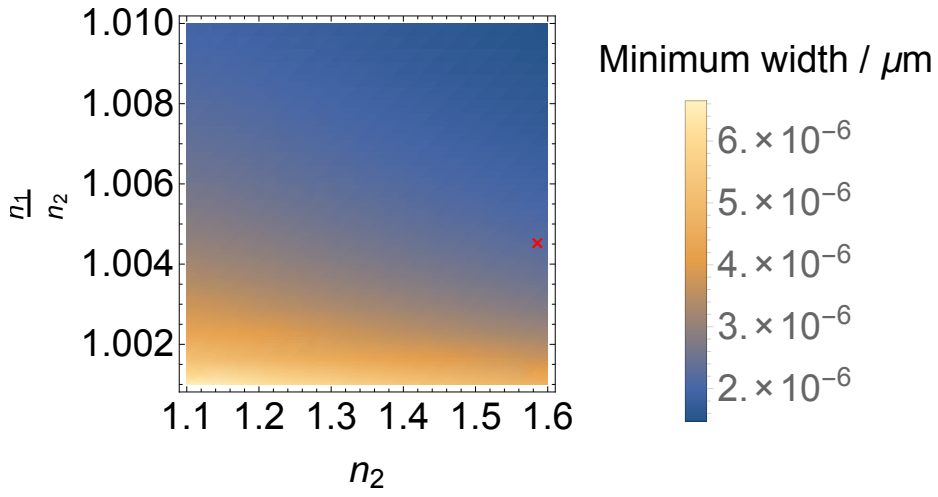

Fig. 2.4: Plot of minimum sizes required to support a guided mode of a square waveguide consisting of a core with refractive index n_1 surrounded on the sides and bottom by a cladding of refractive index n_2, and with the top surface of the guide exposed to vacuum, in terms of n_2 and the ratio n_1/n_2.

$$\xi_i = \frac{1}{|k_i|} \tag{2.32}$$

$$\eta_i = \frac{1}{|k_i|} \tag{2.33}$$

By writing the arctangent terms in Eqs.(2.30) and (2.31) as a power series, expressions for the ξ and η terms may be found:

$$\xi_i = \frac{A_i}{\pi}[1 - (\frac{A_i}{a}\frac{1}{1 + \frac{A_4 + A_5}{\pi a}})^2]^{-\frac{1}{2}} \tag{2.34}$$

$$\eta_i = \frac{A_i}{\pi}[1 - (\frac{A_i}{b}\frac{1}{1 + \frac{{n_2}^2{A_2}^2 + {n_3}^2{A_3}^2}{\pi {n_1}^2 b}})^2]^{-\frac{1}{2}} \tag{2.35}$$

, where $A_i = \lambda_0/2\sqrt{{n_1}^2 - {n_i}^2}$.

The terms ξ_i and η_i are reciprocals of the exponential decay constant of the field outside the waveguide core. The value of β for a given waveguide may then be calculated from the values of ξ and η.

In the case of the mode where E_x and H_y are dominant, a similar procedure can be used to generate values of ξ_i and η_i from Eqs.(2.24) and(6.16) after performing the relevant substitutions of E_x for H_x, ϵ_0 for μ_0, and vice versa.

Naively, it is possible to use Eqs.(2.34) and (2.35) to derive minimum values of a and b necessary for a given waveguide to support propagating modes(see Fig.(2.4). For such modes to exist, ξ_i and η_i must be real and positive. One may then obtain the minimum values of a and b by solving the resulting inequalities. In the case of light with wavelength 1000 nm coupled through the guide, this is found to be 2.2 μm. However, recalling that Eqs.(2.34) and (2.35) represent power series of the arctangent terms in Eqs.(2.30) and (2.31) in $\xi_i k_x$ and $\eta_i k_y$, the approximation above ceases to be valid where the size of the guide is only slightly larger than the minimum size.

To write Eqs.(2.30) and (2.31) as power series, $\xi_i k_x$ and $\eta_i k_y$ must be small. In turn, this requires that k_i in Eqs.(2.32) and (2.33) is large. In physical terms, this indicates that the approximation given by Eqs.(2.34) and (2.35) applies only where the evanescent wave decays rapidly outside the waveguide boundary, and therefore that the mode is well contained inside the guide. Conversely, where one or more of the evanescent waves extends far beyond the edges of the guide, the approximation given by Eqs.(2.34) and (2.35) does not hold. In the case of a waveguide only slightly larger than the minimum size required to sustain a travelling mode, one would expect large evanescent waves to extend beyond the waveguide boundary. In place of the power series given by Eqs.(2.34) and (2.35), therefore, we instead turn to numerical methods of determining the properties of a waveguide mode under such conditions, in order to solve Eqs.(2.24) and (6.16). Using such methods, we will be able accurately calculate mode profiles and k-vectors associated

with light propagating through the waveguide.

2.4 Waveguide materials: fabrication and optical properties

While this thesis is mostly concerned with simulations of light propagating through waveguides, some words regarding the choice of materials for fabricating actual waveguides is necessary, by way of explanation of the choices for the parameters of the simulations discussed here.

Naively, one may construct a dielectric waveguide by simply selecting any two substances with appropriate refractive indices and placing them together. A large variety of inorganic dielectric materials exists, with an equally large range of refractive indices to choose from. Such materials are typically deposited on surfaces using various forms of physical vapor deposition [50]. In the case of atom chips, structures are already present on the surface in the form of trapping wires, with typical thicknesses between 1 to 5 μm [1]. Physical vapor deposition of material over a surface with such structures can yield uneven results, in particular, uneven distribution of material due to shadowing of areas from the incoming atom flux [51]. More importantly, the shape of the wires on the chip surface may be carried through to the top of the deposited layer, resulting in an uneven surface on which it is not possible to construct a usable waveguide.

A far simpler alternative to physical vapor deposition of inorganic dielectrics is to construct the waveguide out of layers of organic photoresists. Deposition of these materials is comparatively easy, requiring only regular spin coating and ultraviolet lithography techniques. As such materials are semi-fluid when deposited, the surface of a spincoated layer will level itself out over the chip wires. One method of fabricating a waveguide, composed of an optically dense core surrounded by a less dense cladding, is described in

[52]. A base layer of SU-8 is laid down on top of the atom chip, exposed to ultraviolet light, and cured in the usual fashion. A second layer is then laid over the first to the desired thickness of the waveguide. The intended core region of the waveguide is masked off, while the rest of the layer is exposed to ultraviolet light. The sample is then baked in order to induce cross-linking between the SU-8 molecules. In the exposed region, this takes place at low temperatures, forming a solid polymer structure out of which the solvent evaporates as the temperature increases. In the masked region, cross-linking only takes place after the solvent has evaporated, allowing the molecules to have collapsed on each other. The photoresist inside this region is therefore slightly denser than in the exposed region, and possesses a slightly larger refractive index.

Using the method described above, waveguides of several microns' thickness can be fabricated using standard photolithography equipment. The calculations performed in this thesis were carried out with the intention of obtaining parameters for the eventual fabrication of actual waveguides for experimental purposes. The materials that were chosen for this simulation reflect this intention–as differentially cured SU-8 guides are easily fabricated using equipment available at our lab, all simulations have been carried out using these materials.

2.5 Evanescent-waves and surface plasmon polaritons

In the final section of this chapter, we wish to discuss the incorporation of plasmonic structures into our waveguides. Surface plasmon polaritons are electromagnetic oscillations propagating along the boundary between a metal and a dielectric. Such oscillations arise from resonances between the electromagnetic field and the free electrons within the metal, and take the

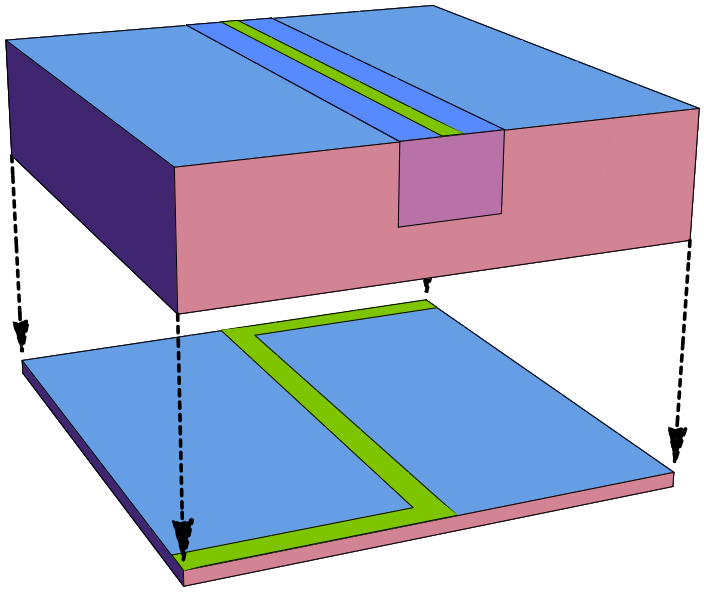

Fig. 2.5: Drawing of a plasmonic structure emplaced on the top surface of the waveguide from Fig(2.3b), which is in turn emplaced on top of an atom chip. Surface plasmons are excited by light passing through the waveguide, enhancing the evanescent wave over the top of the waveguide. The enhanced evanescent wave is then used either to detect or to tightly confine atoms held over the waveguide surface.

form:

$$E = E_0 e^{i(k_z z \pm k_y(y) y + \omega t)}, \tag{2.36}$$

where k_z is the component of the wavevector at frequency ω along the metal surface, $k_y(y)$ is the component of the wavevector perpendicular to the surface, the value of which depends on the sign of y, and $\sqrt{\epsilon} k_0 = \sqrt{{k_x}^2 + {k_y}^2}$, where ϵ is the dielectric constant, and $k_0 = \omega/c$. Here, the metal-dielectric interface is taken to be at $y = 0$, k_y is given by [53]:

$$k_y = \begin{cases} \frac{2\pi}{\lambda} \sqrt{\frac{{\epsilon_0}^2}{\mathrm{Re}(\epsilon_1)+\epsilon_0}} & y > 0 \\ \frac{2\pi}{\lambda} \sqrt{\frac{[\mathrm{Re}(\epsilon_1)]^2}{\mathrm{Re}(\epsilon_1)+\epsilon_0}} & y < 0 \end{cases} \tag{2.37}$$

where ϵ_1 is the complex dielectric constant of the metal. Of particular importance here is the fact that $\mathrm{Re}(\epsilon_1) < 0$. Furthermore, in the case of

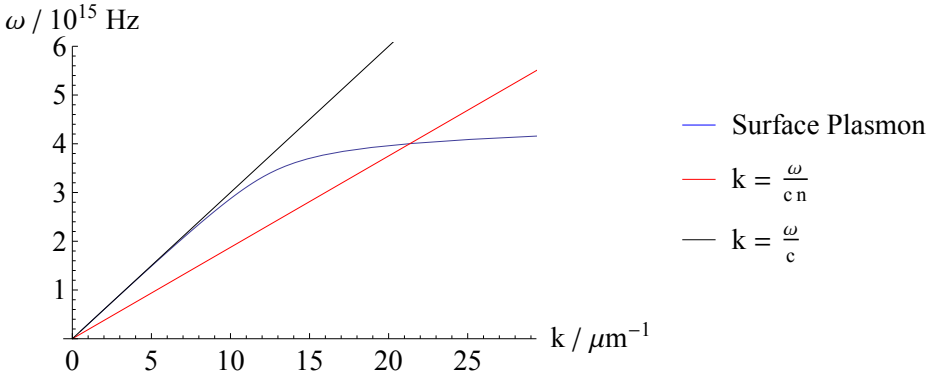

Fig. 2.6: Plot of the dispersion relation of a surface plasmon propagating along a metal-vacuum boundary, along with the dispersion relation of light travelling through a vacuum, $k = \omega/c$, and the dispersion relation of light travelling through a medium with refractive n, $k = \omega/(cn)$. Note that the line representing propagation of light through a vacuum does not intersect the dispersion curve of the surface plasmon anywhere except at the origin, preventing coupling between the vacuum and the surface plasmon. It is however possible for coupling to occur between light travelling through a medium with refractive index n and the surface plasmon.

near-infrared light propagating along a gold-vacuum interface, $|\,\mathrm{Re}(\epsilon_1)| \gg \epsilon_0$ (From [54], $60 < |\,\mathrm{Re}(\epsilon_1)| < 100$ for $0.7\ \mu\mathrm{m} < \lambda < 2\ \mu\mathrm{m}$). Substituting these values into Eq. (2.37), it is shown that $k_y|_{y<0} \gg k_y|_{y>0}$, and therefore that the evanescent wave of the surface plasmon decays much slower in the vacuum than it does in the gold. The vast majority of the oscillating electric field of the surface plasmon, and by extension, the energy of the oscillation, is thus concentrated in the region immediately above the metal surface.

The particular importance of this result lies in the fact that when energy from incident light is coupled into the oscillation, most of that energy is concentrated in the evanescent wave extending into the vacuum. By placing a metal structure on the upper surface of a waveguide, and allowing light to couple in to it, the evanescent wave over the surface may therefore be enhanced locally above that structure.

To couple light at frequency ω into a surface plasmon, the component of the wavevector $\mathbf{k}_0$ parallel to the surface, where $|\mathbf{k}_0| = \omega/c$, must match

the wavenumber k_z of the surface plasmon along the metal-vacuum interface. The value of k_x is in turn given by the dispersion relation:

$$k_z = \frac{\omega}{c}\sqrt{\frac{\epsilon_1\epsilon_0}{\epsilon_1+\epsilon_0}} \tag{2.38}$$

For complex ϵ_1, a complex k_z is obtained, where:

$$\mathrm{Re}(k_z) = \frac{\omega}{c}\sqrt{\frac{\mathrm{Re}(\epsilon_1)\epsilon_0}{\mathrm{Re}(\epsilon_1)+\epsilon_0}} \tag{2.39}$$

$$\mathrm{Im}(k_z) = \frac{\omega}{c}\left(\frac{\mathrm{Re}(\epsilon_1)\epsilon_0}{\mathrm{Re}(\epsilon_1)+\epsilon_0}\right)^{\frac{3}{2}}\frac{\mathrm{Im}(\epsilon_1)}{2\,\mathrm{Re}(\epsilon_1)^2} \tag{2.40}$$

In the case of complex k_z, coupling is achieved by matching the horizontal component of $\mathbf{k}_0$ to $\mathrm{Re}(k_z)$.

In the case of light incident on a metal surface from vacuum, $\mathrm{Re}(k_z) > k_0$ (see Fig.(2.6)). It is therefore not possible to couple light directly from a vacuum into the surface plasmon. Light is instead coupled into the plasmon either by using a grating to impart the necessary momentum to the incident wave, or by coupling the light into the metal through an optically denser medium, such that the wavenumber of the incident light is multiplied by the refractive index of the medium.

In this thesis, we are concerned with the second method of coupling light to a surface plasmon. The structures studied here include rectangular waveguides with metal wires emplaced on their top surfaces. Surface plasmons are then excited inside the wires by light coupled through the waveguide underneath. A brief explanation of the mechanics of this excitation is therefore also necessary.

A thin metal layer lies on top of a dielectric substrate with refractive index n. The top of the layer is in turn exposed to vacuum. Light with

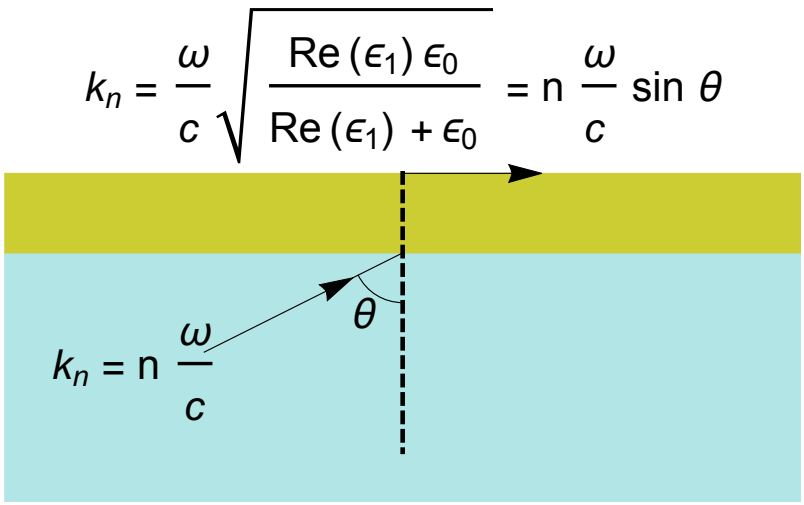

Fig. 2.7: Sketch of method for coupling between light travelling in a medium with refractive index n and a surface plasmon propagating at a metal-air interface, as described by Eq.(2.41).. Light with frequency ω travelling through the medium intersects the medium-metal boundary at incident angle θ, which is chosen such that the component of k_n parallel to the boundary is equal to the wavenumber of the plasmon, k_{Plas}, given by Eq.(2.38).

frequency ω propagates through the medium with wavenumber nk_0, where $k_0 = \omega/c$. When the light is incident on the bottom of the metal layer at an angle θ, coupling is then achieved with the surface plasmon *on top* of the metal layer, at the metal-vacuum boundary, at:

$$nk_0 \sin\theta = k_0\sqrt{\frac{\mathrm{Re}(\epsilon_1)\epsilon_0}{\mathrm{Re}(\epsilon_1)+\epsilon_0}} \tag{2.41}$$

The equations in this section represent a simplified version of actual structures studied in this thesis. The description of surface plasmons propagating over a narrow wire, as opposed to the simple slablike structures described here, is complicated by various factors, including the finite horizontal dimensions of the wire it self, as well as the effects of plasmon waves reflecting off the wire edges. Furthermore, in contrast to the case of the dielectric slab, it is not always possible to control the incident angle θ of light reaching the boundary of a waveguide. Where θ is far from the resonant angle given in

Eq.(2.41), the electromagnetic fields of the incident light instead couple to the free electrons in the metal as a forced damped oscillation. The surface plasmon oscillations of a wire over a dielectric waveguide are therefore far harder to describe analytically than the simplified model used in this section.

In subsequent chapters, as an alternative to analytical methods, we use numerical techniques to calculate the electromagnetic fields produced by surface plasmons excited in a metal wire by light travelling through the waveguide underneath the wire. The results of these calculations are then used to predict the fluorescence and the dipole force potentials experienced by neutral atoms over the wire.

3. MATHEMATICAL AND COMPUTATIONAL METHODS FOR WAVEGUIDE SOLUTION

3.1 Introduction

In this chapter, the methods used to obtain computational results for modes of waveguides, and for the enhanced evanescent fields generated by metal wires, are discussed. Principally, finite-difference time-domain simulations were used to obtain solutions to these problems, in particular, the use of the free software package MEEP to simulate the propagation of modes down a waveguide, as well as the commercial FDTD-Solutions software released by Lumerical Solutions Inc., for simulating the response of metal structures over waveguides to light coupled into said waveguides.

The structures investigated in this thesis take the form of long, rectangular dielectric waveguides, embedded within a surrounding dielectric layer of lower refractive index. The top surface of the waveguide is flush with the top surface of the surrounding dielectric, allowing the evanescent wave of the mode travelling through the guide to extend into the vacuum above. As an initial approximation, trial functions of the principle mode are generated by solving the 1-dimensional Maxwell wave equation for the electric field along the $x-$ and $y-$axes through the centerline of the guide. The trial function is then formed from the product of these solutions, and input into a finite-difference time-domain simulation as the amplitude function of a two-dimensional electromagnetic source.

To refine the approximation formed by the trial function, finite-difference time-domain simulations of the waveguides are carried out. Simulated light is propagated down these waveguides from a source defined at one end of the guide. The mode shape of the light emitted by this source is given by the trial functions, which can in turn be expressed as a Fourier series. The eigenmodes of the Maxwell wave equation through the waveguide can similarly be expressed as a slightly different Fourier series. As the trial mode propagates down the guide, those Fourier components of the trial function which are not also part of the waveguide mode escape the waveguide and are removed from the simulation by the perfectly-matched layer, leaving behind only those which do make up the mode. To assess the ability of a set of square waveguides of varying dimensions to support a guided mode, this procedure is carried out, and the change in the transverse amplitude function is monitored as the light propagates through the guide.

Finally, having examined the ability of our waveguides to carry guided modes of light, a new element is added to those simulations in the form of a metal wire emplaced down the centerline of the exposed top surface of the waveguide. Via coupling between the mode of the guide and surface plasmons within the wire, the evanescent field is enhanced within the region directly above the wire. Using FDTD simulations, profiles of the evanescent electric field within the area of a few square microns around the wire are calculated. From this calculation, and from the simulations of the waveguide mode above, data used to derive results reported in Chapters. 4, 5 and 6 is obtained.

3.2 Numerical Solutions for Waveguide Modes

3.2.1 Introduction and justification

Computational methods of electromagnetics have been well developed as means of studying electric and magnetic fields passing through and around objects of various shapes and materials [55]. In the following section, I describe the very first simulations to be carried out for the purposes of this thesis. These initial simulations were approached from the perspective of a newcomer to computational electromagnetics. Hence, ease of implementation and simplicity were desired when selecting a method of solving waveguide modes. It was also desired that such a method be easy to implement.

The most direct means of solving the Maxwell wave equation for modes of a waveguide involves generating and diagonalising a matrix representing the operators that make up the equation. The set of guided modes available for a given waveguide is then given by the eigenvectors of this matrix. To obtain accurate solutions, it is necessary to discretise the field at a large number of points across the region over which the equation is being solved. A very large vector is therefore required to express a solution for the wave equation, which in turn requires that we generate and diagonalise a very large matrix. Unfortunately, the process of diagonalising such a matrix is computationally challenging, even with a very sparse matrix and using the most efficient eigensolvers available. Some less intensive means of solving the Maxwell wave equation is therefore desired.

Ideally, any issues arising from the difficulty of implementing a numerical solver for the modes of a waveguide may be sidestepped by making use of commercial software created to carry out such calculations. At the time this stage of the thesis project was carried out, only limited access to such software was available. Rather than make use of such commercial software, it

was therefore decided to take advantage of various free, open-source solutions already available.

Other techniques available for carrying out simulations of waveguide modes include both finite-difference time-domain as well as finite-element methods (FEM). Using the first method, fields over the area to be simulated are discretised over a rectangular grid. Starting from an initial electromagnetic oscillation placed at a selected location in the comptational region, the propagation of electromagnetic waves from this location is then calculated by solving Ampere's and Faraday's laws over each grid cell. Using this method, a waveguide mode is found by allowing the waves originating from the initial oscillation to propagate through the guide until a steady state is reached.

By contrast, finite element methods involve discretising the computational region in the form of a collection of triangular elements of variable sizes. The size of each element in turn depends on the size of the structure being simulated–elements simulating fields near a large structure are themselves large, while elements in the vicinity of a smaller structure are similarly reduced in size. This allows structures with very large differences in size to be efficiently simulated in a finite-element calculation. A "stiffness matrix", representing the operators of the Maxwell wave equation, is generated from the structure of all the combined elements. Solutions of the equation are then obtained from an initial trial solution using a method of weighted residuals. Using FEM, one may find a waveguide mode simply by solving the wave equation across a transverse cross-section of the guide.

On the surface, FEM appears to be preferable to FDTD, in particular, for the task of solving for the modes of a waveguide. Rather than calculate the evolution of a wave through the waveguide for an indeterminate period of time until a steady state is reached, waveguide modes may be found using the finite-element method by solving a single matrix eigenvector equation.

In addition to this, while grid points must be defined over the entirety of the computational cell in the case of the FDTD simulation, one only needs to define elements over the transverse cross-section of the waveguide. Not only does a finite element calculation of a waveguide mode require less memory than an FDTD simulation, one may theoretically obtain desired results much faster using FEM than is possible using FDTD.

An inverse to these arguments, it must be noted that, using the FDTD method, the propagation of the EM wave through the guide is calculated explicitly, using simple difference equations involving field values at adjacent points in the computational grid. This is in contrast to the grid of triangular elements used in the FEM calculation, which requires considerable computation just to set up. Additionally, considerably more background knowledge is required in order to set up the triangular grid than is necessary for the FDTD calculation. In the interests of being able to set up and run simulations within a reasonable amount of time, FDTD simulations appear to be preferable to FEM.

The deciding factor in chosing FDTD methods over FEM was the existence of `MEEP` [56], a completed, free FDTD software package capable of carrying out evaluations out of the box. This text-based solver was also chosen over other, more graphically polished packages due to the availability of comprehensive, yet easily-comprehensible and easily-accessed documentation.

Here, an approximation of the mode of a waveguide is constructed out of two one-dimensional solutions of the Maxwell wave equation along the transverse axes of the guide. This trial mode is then used to construct an amplitude function for light to be propagated down the guide. Changes in the mode shape as the light propagates down the guide are observed, and true modes of the waveguide are considered to be found once the mode shape

stabilizes.

3.2.2 Generation of Waveguide Trial Modes

The mode of a rectangular waveguide may be found by solving Eq.(2.23). One approximate solution of this equation for the rectangular guide is given by Eq.(2.24). As an alternative, the solution to the equation may be found numerically by generating trial modes and propagating them through a simulated guide, allowing those Fourier components of the test mode that are not confined modes of the waveguide to propagate out of the computational cell.

To minimise the time required for extraneous Fourier components to be removed from the cell, it is desirable to select a test mode to be as close to the actual mode as possible. To do this, an approximation similar to that given in Eq.(2.24) is proposed–the Maxwell wave equation is solved in 1-dimension along the axes running through the centerline of the waveguide core. The wave equation is thus reduced from two dimensions to one, and is thus much easier to solve numerically:

$$(\frac{\partial^2}{\partial x^2} + \frac{n(x)^2\omega^2}{c^2})E(x) = \beta^2 E(x) \tag{3.1}$$

Discretisation of the Maxwell Wave Equation

To solve Eq.(3.1) numerically over the domain x, we reduce x from a continuous variable to a set of N equally spaced points: $(x_1, x_2, .., x_N)$. The solution can then be expressed as an N-dimensional vector:

$$E(x) = \begin{pmatrix} E(x_1) \\ E(x_2) \\ \vdots \\ E(x_N) \end{pmatrix}. \tag{3.2}$$

When $\delta x = x_{i+1} - x_i$ is sufficiently small, the second differentiation operator is approximated by:

$$\frac{\partial^2 E}{\partial x^2} \simeq \frac{1}{\delta x}\left(\frac{E(x_{i+1}) - E(x_i)}{\delta x} - \frac{E(x_i) - E(x_{i-1})}{\delta x}\right) \tag{3.3}$$

$$= \frac{E(x_{i+1}) - 2E(x_i) + E(x_{i-1})}{\delta x^2} \tag{3.4}$$

or, expressed in the form of an $N \times N$ matrix as an operator on the vector $E(x)$:

$$\frac{\partial^2 E}{\partial x^2} = \frac{1}{\delta x^2} \begin{pmatrix} -2 & 1 & 0 & ... & ... & 0 \\ 1 & -2 & 1 & ... & ... & 0 \\ 0 & 1 & -2 & ... & ... & 0 \\ \vdots & & \ddots & & & \\ \vdots & & & \ddots & & \\ 0 & ... & ... & 1 & -2 & 1 \\ 0 & ... & ... & 0 & 1 & -2 \end{pmatrix} \begin{pmatrix} E(x_1) \\ E(x_2) \\ E(x_3) \\ \vdots \\ E(x_{N-1}) \\ E(x_N) \end{pmatrix}. \tag{3.5}$$

The second term in Eq.(3.1) is written as an $N \times N$ diagonal matrix with elements $(\omega^2/c^2)\mathcal{N}$ where $\mathcal{N} = (n(x_1), n(x_2), ..., n(x_N))$. The equation can then be solved by taking the sum of the two matrices, and calculating the eigenvectors of the resulting system.

Code for generating the operator matrix was implemented in C. The

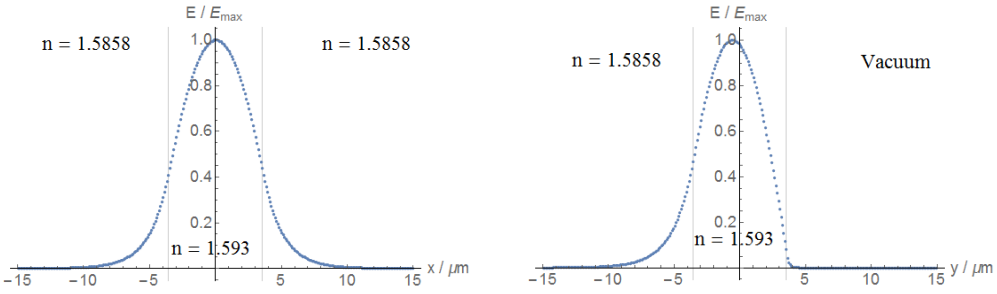

(a) (b)

Fig. 3.1: Plots of the elements of the eigenvectors of Eq.(3.1), normalised such that the maximum value of the field is 1, plotted over a). the vertical axis extending through the centre of the waveguide core, and b). the horizontal axis extending through the same point.

$N \times N$ array representing the operator matrix is populated iteratively over a nested pair of N-fold `for` loops, so as to easily identify those elements on and around the diagonal with non-zero values. Once generated, `LAPACK` functions are called to solve for the eigenvectors of the system. Eigenvectors are output as $N \times N$ matrices, from which the fundamental mode is isolated and written to file to be used to generate the trial mode in the finite-difference time-domain solver.

The code for this calculation was used to evaluate solutions of Eq.(3.1) for a set of square waveguides between 5 to 10 μm in size, located at the centre of a 30 μm by 30 μm computational cell. The resolution of the calculation is set at 10 points per μm, such that $N = 300$. This resolution is chosen to create a 1-to-1 correspondence between each element of the solution vector and each point along the sides of the computational cell, as described below. The code was run on an ordinary laptop computer, with each solution taking less than a minute to complete.

3.2.3 Finite-difference time-domain evaluations of the waveguide mode

In a finite-difference time-domain calculation, the region being investigated is discretised in the form of a rectangular grid, with discretisation points at the

corners and in the centre of each grid cell. In addition to this, the evolution of the system through time is expressed as a series of discrete steps which are further divided into half-steps. Values of the electric field are recorded at the corners of each cell, while values of the magnetic field are recorded at the cell centre. The evolution of the electric and magnetic fields is calculated from an initial electric field at time $t = 0$ using the following equations:

$$\hat{H}(\mathbf{r}_{i+\frac{1}{2},j+\frac{1}{2},k+\frac{1}{2}}, t + \frac{\delta t}{2}) = \hat{H}(\mathbf{r}_{i+\frac{1}{2},j+\frac{1}{2},k+\frac{1}{2}}, t - \frac{\delta t}{2}) - \frac{\delta t}{\mu}(\nabla \times \hat{E}(t)) \quad (3.6)$$

$$\hat{E}(\mathbf{r}_{i,j,k}, t + \delta t) = \hat{E}(\mathbf{r}_{i,j,k}, t) + \frac{\delta t}{\epsilon}(\nabla \times \hat{H}(t + \frac{\delta t}{2}) \quad (3.7)$$

where the vectors $\mathbf{r}_{i,j,k}$ and $\mathbf{r}_{i+\frac{1}{2},j+\frac{1}{2},k+\frac{1}{2}}$ are given by the coordinates (x_i, y_j, z_k) and $(x_{i+\frac{1}{2}}, y_{j+\frac{1}{2}}, z_{k+\frac{1}{2}})$ respectively, $(x_{i+\frac{1}{2}}, y_{j+\frac{1}{2}}, z_{k+\frac{1}{2}}) - (x_i, y_j, z_k) = 1/2(\delta x(i), \delta y(j), \delta z(k))$, and $\delta x, \delta y$, and δz are the grid step sizes along each axis. The discretised form of the curl operator is given by:

$$\nabla \times \hat{H}(\mathbf{r}_{i+\frac{1}{2},j+\frac{1}{2},k+\frac{1}{2}}) = \begin{pmatrix} \frac{E_z(\mathbf{r}_{i,j+1,k}) - E_z(\mathbf{r}_{i,j,k})}{\delta y} - \frac{E_y(\mathbf{r}_{i,j,k+1}) - E_y(\mathbf{r}_{i,j,k})}{\delta z} \\ \frac{E_x(\mathbf{r}_{i,j,k+1}) - E_x(\mathbf{r}_{i,j,k})}{\delta z} - \frac{E_z(\mathbf{r}_{i+1,j,k}) - E_x(\mathbf{r}_{i,j,k})}{\delta x} \\ \frac{E_y(\mathbf{r}_{i+1,j,k}) - E_y(\mathbf{r}_{i,j,k})}{\delta x} - \frac{E_x(\mathbf{r}_{i,j+1,k}) - E_x(\mathbf{r}_{i,j,k})}{\delta y} \end{pmatrix} \quad (3.8)$$

$$\nabla \times \hat{E}(\mathbf{r}_{i,j,k}) = \begin{pmatrix} \frac{H_z(\mathbf{r}_{i-\frac{1}{2},j+\frac{1}{2},k-\frac{1}{2}}) - H_z(\mathbf{r}_{i-\frac{1}{2},j-\frac{1}{2},k-\frac{1}{2}})}{\delta y} - \frac{H_y(\mathbf{r}_{i-\frac{1}{2},j-\frac{1}{2},k+\frac{1}{2}}) - H_y(\mathbf{r}_{i-\frac{1}{2},j-\frac{1}{2},k-\frac{1}{2}})}{\delta z} \\ \frac{H_x(\mathbf{r}_{i-\frac{1}{2},j-\frac{1}{2},k+\frac{1}{2}}) - H_x(\mathbf{r}_{i-\frac{1}{2},j-\frac{1}{2},k-\frac{1}{2}})}{\delta z} - \frac{H_z(\mathbf{r}_{i+\frac{1}{2},j-\frac{1}{2},k-\frac{1}{2}}) - H_x(\mathbf{r}_{i-\frac{1}{2},j-\frac{1}{2},k-\frac{1}{2}})}{\delta x} \\ \frac{H_y(\mathbf{r}_{i+\frac{1}{2},j-\frac{1}{2},k-\frac{1}{2}}) - H_y(\mathbf{r}_{i-\frac{1}{2},j-\frac{1}{2},k-\frac{1}{2}})}{\delta x} - \frac{H_x(\mathbf{r}_{i-\frac{1}{2},j+\frac{1}{2},k-\frac{1}{2}}) - H_x(\mathbf{r}_{i-\frac{1}{2},j-\frac{1}{2},k-\frac{1}{2}})}{\delta y} \end{pmatrix} \quad (3.9)$$

For the purposes of this project, simulations of light propagating down rectangular waveguides were carried out using the free `MEEP` software. The region under investigation consists of a 30 μm by 30 μm by 150 μm box, discretised at a resolution of 10 points per micron. Simulated light was propagated through the computational cell at wavelengths of 780nm and 1000nm, values chosen for their use in atomic physics for manipulating and detecting rubidium atoms. The discretisation of the computational cell is chosen such that the oscillation of light over a given wavelength can be properly represented.[1] A length of 150 μm was chosen over which to propagate the waveguide mode in order to investigate the change in said mode when propagated over long distances. The transverse dimensions of the waveguide are chosen such that the evanescent waves extending from the edges of the waveguide core decay to zero well short of the edges of the computational cell. The outermost 1-micron layer along the boundaries of the computational cell is designated a perfectly-matched layer(PML). This layer is implemented, for an incident wave, $E(x,t) = E_0 \exp[i(\omega t - \beta x)]$, normal to the boundary, by adding a linearly increasing imaginary component to the spatial coordinate x as it travels through the layer, such that the wave becomes:

$$E(x,t) = E_0 e^{i(\omega t - \beta(1+in)x)} \tag{3.10}$$

$$= E_0 e^{-n\beta x} e^{i(\omega t - \beta x)} \tag{3.11}$$

Adding this imaginary component to x thus introduces an exponential decay to the amplitude of the wave. The wave therefore disappears, rather than reflecting off the boundary of the cell, thus simulating the propagation

[1] The resolution of discretisation over the computational cell in turn influences the choice of N in Sec.3.2.2. Here, N is chosen such that the discretisation points along the 1-dimensional axis correspond exactly to the points along the identical transverse axis in the computational cell.

of the wave through the cell border into infinity.

For the purposes of this simulation, we take the transverse plane of the computational cell to be the xy-plane, and the longitudinal axis, along which the wave propagates, to be the z-axis. The simulation is initialised by placing an electromagnetically oscillating source inside the computational cell. In the case of the rectangular waveguide, this consists of a 2-dimensional square occupying the entire transverse plane of the computational cell. This square produces an electromagnetic oscillation $E(\mathbf{r}, t)$, given by:

$$E(\mathbf{r}, t) = X(x)Y(y)e^{i(\beta z - \omega t)} \tag{3.12}$$

where $X(x)$ and $Y(y)$ are the solutions to the Maxwell wave equation along the principal axis of the transverse plane calculated using the eigenvector equation described in Sec.(3.2.2), β is the wavevector of the propagation down the z-axis, and ω is the oscillation frequency.

The solutions $X(x)$ and $Y(y)$ are obtained in Sec.(3.2.2) in the form of a pair of vectors of length 300. Each element in $X(x)$ and $Y(y)$ is then associated with the $x-$ or $y-$ coordinate, respectively, of a given point in the source plane. The field amplitude at a given point, (x_i, y_i) on the source plane is then given by the product $X(x_i)Y(y_i)$, and $X(x)Y(y)$ is the mode shape function of the electromagnetic wave emitted by the source.[2]. This trial mode is then allowed to propagate down the waveguide. The Fourier components of the trial mode which do not exist in the actual mode propagate out of the guide and are lost through the PML, while the shape function associated

[2] As integrated into the default version of MEEP, amplitude functions are generated by evaluating a given analytical function at the location of each grid point inside the electromagnetic source. It is known, however, that the function is evaluated only at those points. The analytical function can therefore be replaced by a list of values of the mode shape function in which each element corresponds to a given point, or by a set of lists associated with the principal axes of the source plane, in which element corresponds to a given coordinate along that axis.

with the true mode is left behind.

It is sometimes necessary to propagate the mode over distances greater than 150 μm. This is done in some cases to allow the unwanted Fourier components of the trial mode to fully escape from the computational cell. Furthermore, by allowing the mode to propagate over large distances, it is possible to verify that the actual waveguide mode has been obtained by checking that the mode shape remains constant over those distances. The amount of memory available to carry out such calculations is however limited, which in turn limits the maximum size of the computational cell available to perform calculations. To overcome these limits, propagation over distances greater than 150 μm is simulated by retrieving the mode profile $K(x, y)$ leaving the end of one waveguide and using it to generate the mode shape function of the source at the start of a second computation. Values of the electromagnetic field are taken at discretisation points along the transverse plane near the end of the waveguide and then loaded, one-for-one, into the corresponding points on the source plane of the second simulation[3].

Computations of the propagation of the trial modes through a waveguide were carried out in parallel using 8 2.67 GHz HP Xeon cores of the `atlas4` 64-bit Linux cluster at NUS. The trial mode was propagated through the guide over 6000 individual time steps, so as to allow the mode to propagate over the entire length of the waveguide. At each of the final 20 time steps, the electromagnetic energy density at every grid point is saved to a data file. To illustrate this process, cross-sectional representations of the energy density recorded at a given timestep for a 5 μm and a 7 μm waveguide

[3] The mode shape profile extracted from the end of the first waveguide is stored as plain text in a data file. The total number of discretisation points in a transverse cross-section of the computational cell is $300^2 = 90000$, too large to be loaded into memory as a single array. Instead, a series of nested functions are used to associate a particular point on the source plane to a particular line in the data file, move the I/O port to that line, and read the contents of that line into memory.

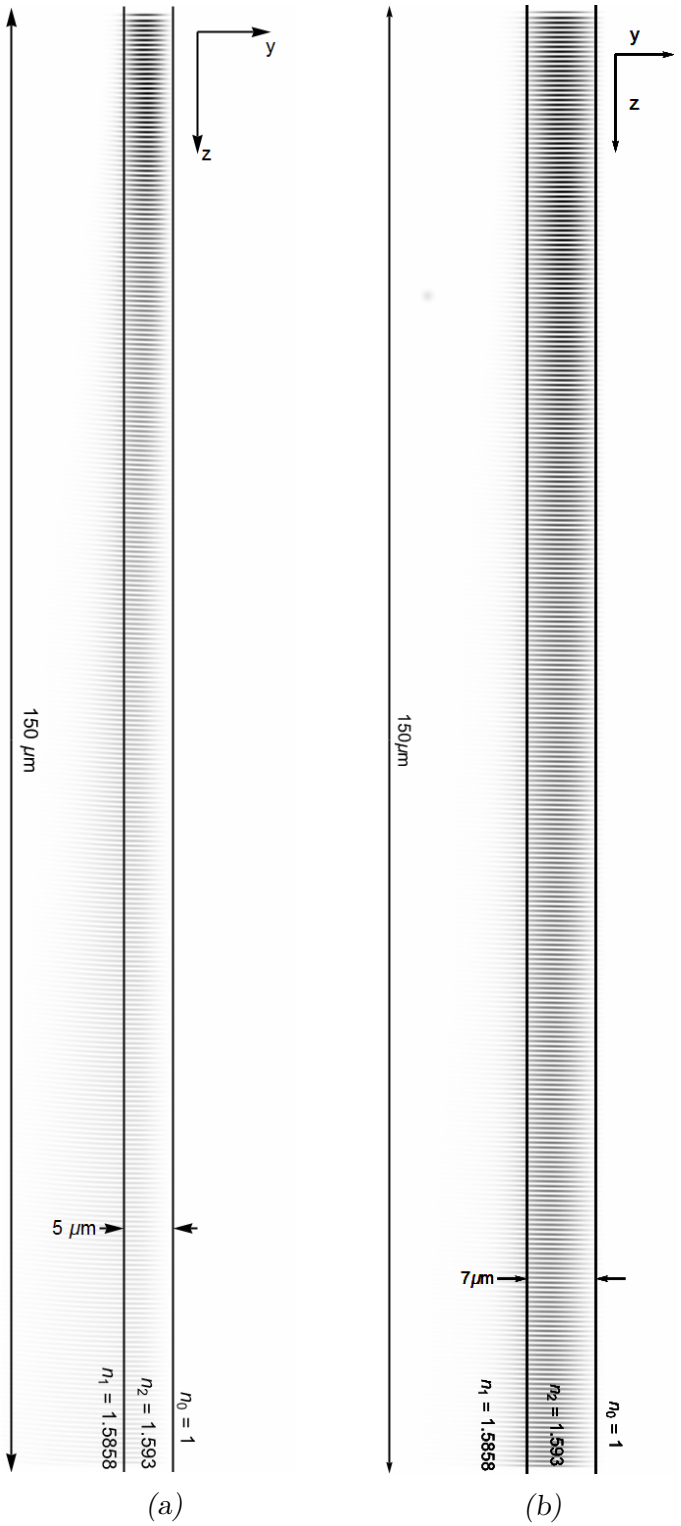

Fig. 3.2: Color plots through the yz plane of test modes propagating down waveguides from the top of the page through a). a 5 μm by 5 μm waveguide, and b). a 7 μm by 7 μm waveguide. Both images are generated using energy-density data measured over all points within the computation grid and saved as data files. Mode shapes are then taken from the end of the waveguide (at the bottom of the page) and used as trial modes for a second set of FDTD simulations used to confirm if convergence of the trial modes to the waveguide modes has taken place.

have been reproduced in Fig.(3.2). The sum of the data recorded in these files is then used to calculate the average steady-state energy density of the electromagnetic field over the entire computational cell. The evolution of the transverse energy density as the wave propagates along the cell is then quantified by taking the overlap integral between the wave profile at a given point along the guide, and the wave profile taken from the end of the guide. The ability of the guide to sustain a confined mode may then be assessed by whether or not the overlap integral remains near unity over long distances.

Simulations are carried out of square waveguides of widths between 5 μm and 10 μm. To allow each wave to propagate a sufficient distance such that the overlap integral is able to converge towards unity, at the conclusion of each simulation, mode profiles are taken from the opposite end of the waveguide from the source. These mode profiles are then used to create trial modes that are then fed into subsequent simulations of the same structure, effectively passing the wave from the end of one simulation to the next, and the overlap integrals as the waves propagate down the guide are calculated for this second set of simulations. The results of these calculations, in particular, the convergence of the overlap integrals towards unity as the wave propagates through the guide, are discussed in Sec.(4.2).

To summarise work described in this section, finite-difference time-domain simulations using `MEEP` are used to calculate eigenmodes of dielectric waveguides. The method and software are chosen for this calculation due to their simplicity, and the comprehensive and accessible documentation available for the software package. Calculations are carried out by solving the Maxwell Wave Equation in 1-dimension along the transverse axes of the guide, constructing a trial waveguide mode in two dimensions out of the solutions, and propagating this mode down a simulated guide. The change in the transverse profile of this mode is monitored using overlap integrals as the wave travels

down the guide. The eigenmode of the waveguide is then considered to be found when the overlap integral remains near unity over long distances along the guide.

3.3 Finite-difference time-domain simulations of metallic wires on waveguides

FDTD simulations of waveguides overlaid with metallic structures were also attempted using MEEP. However, typical sizes of plasmonics structures are extremely small compared to the size of the underlying waveguide. Very high resolutions are therefore required to simulate the response of plasmonic structures to light within the waveguide, which in turn require very large amounts of memory in order to compute. Simulations of waveguides incorporating metal structures carried out using MEEP were thus found to fail due to insufficient memory.

One possible cause of these failures was determined to be the sheer number of grid points which the solver was required to handle. One possible solution to this problem, therefore, was to make use of a variable grid, with high resolutions in regions where the rate of change of the electromagnetic field is large, and low resolutions in regions where the field changes slowly. Initial attempts to construct simulations making use of such a grid centered around finite-element methods. Solutions for eigenmodes of the Maxwell Wave Equation over the waveguide cross-section were first attempted by constructing a finite-element solver using the free C++ package GetFEM, in order to solve meshes generated in Gmsh [57]. By attempting to construct our own finite-element solver, we would have acquired a computational tool wholly controlled by ourselves, and which would be easily modifiable to be adapted to different problems. Additionally, the expenditure of funds to

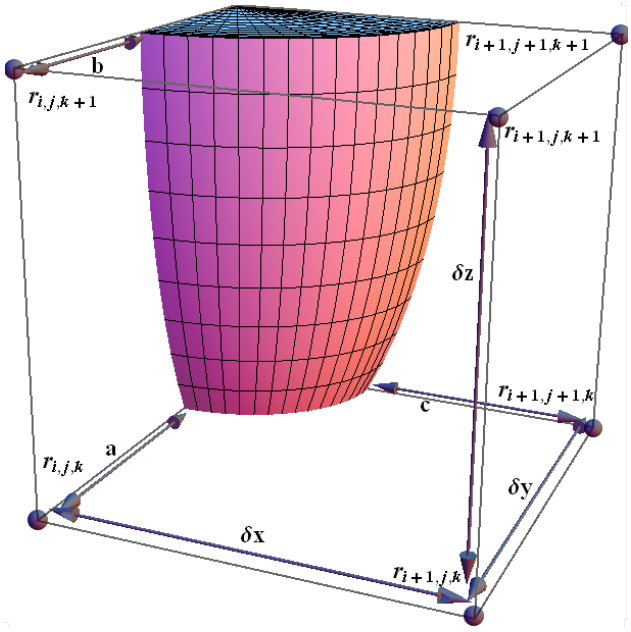

Fig. 3.3: Diagram of a single cell of the FDTD computational grid, with dimensions $\delta x \times \delta y \times \delta z$. The cell is partially occupied by a perfectly conducting metal structure such that the distance along the cell edge between the grid point $\mathbf{r}_{i,j,k}$ and the metal surface is a, the distance between $\mathbf{r}_{i,j,k+1}$ and the surface is b, and the distance between $\mathbf{r}_{i+1,j+1,k}$ and the metal surface is c.

purchase and expensive license for a commercial software solution would be avoided. However, it was found that the complexity of programming such a solver using only open source libraries would have imposed considerable delays. Rather than expend additional time and effort on programming, it was instead decided to purchase the use of a commercially available solution.

The FDTD-Solutions software package provided by Lumerical Solutions Inc. makes use of a dynamically-generated grid with variable step sizes in conjunction with a conformal mesh technique to simulate structures much smaller than the computational cell. The conformal mesh technique used by Lumerical is based on that described by Yu and Mittra [58], for perfect conductors, in which the curl operators used to generate the increments of the magnetic and electric fields are modified by the presence of a metal object intersecting the grid cell.

The modified curl operator can be demonstrated using the cell shown in Fig.(3.3). The volume of the cell is partially occupied by a perfectly-conducting structure. Taking the integral form of Faraday's Law,

$$\oint_{\delta\Sigma} \hat{E}.d\mathbf{l} = -\int_{\Sigma} \frac{\partial \hat{B}}{\partial t}.d\mathbf{A} \tag{3.13}$$

the conformal mesh is implemented by discarding those portions of the loop integral that lie within the metal structure. For the differential form of Faraday's law, this change is implemented by modifying Eq.(3.14):

$$\nabla \times H(\mathbf{r}_{i+\frac{1}{2},\hat{j+\frac{1}{2}},k+\frac{1}{2}}) = \begin{pmatrix} \frac{-\delta z E_z(\mathbf{r}_{i,j,k})}{\delta z \delta y} \_ \frac{bE_y(\mathbf{r}_{i,j,k+1}) - aE_y(\mathbf{r}_{i,j,k})}{\delta y \delta z} \\ \frac{\delta x E_x(\mathbf{r}_{i,j,k+1}) - \delta x E_x(\mathbf{r}_{i,j,k})}{\delta x \delta z} \_ \frac{\delta z E_z(\mathbf{r}_{i+1,j,k}) - \delta z E_z(\mathbf{r}_{i,j,k})}{\delta z \delta x} \\ \frac{\delta y E_y(\mathbf{r}_{i+1,j,k}) - aE_y(\mathbf{r}_{i,j,k})}{\delta y \delta x} \_ \frac{cE_x(\mathbf{r}_{i,j+1,k}) - \delta x E_x(\mathbf{r}_{i,j,k})}{\delta x \delta y} \end{pmatrix} \tag{3.14}$$

As originally formulated, the Yu and Mittra technique was used to perform calculations involving RF and microwave frequencies. The version of the technique implemented by Lumerical replaces the perfect conductors with dispersive materials, in order to reflect the response of materials at optical frequencies. Using such methods, it is possible to model very small structures as part of a much larger computational cell, rather than needing to construct a fine enough grid so as to conform to the shape of the small structures. In addition to the ability of FDTD-Solutions generate a dynamically varying grid depending on the structures present with the shell, the use of the conformal mesh technique allows small plasmonic structures to be simulated within large computational cells, while requiring significantly less memory than a similar simulation constructed using a uniform grid in `MEEP` would.

Simulations were carried out using a computational cell with dimensions 20 μm by 20 μm in the transverse directions, and 45 μm in the longitudinal

direction. The cell contains a 9 μm square waveguide of heat-cured SU-8 running down the centre of the cell, along the z-axis, surrounded on all sides except the top by a cladding of UV-cured SU-8. The top of the waveguide is exposed to vacuum. A thin gold wire, 100nm wide by 20 nm thick, is laid along the centerline of the guide. As above, the dimensions of the cell are chosen such that the waveguide mode decays to zero well short of the cell edges. Simultaneously, the cell is also sufficiently long that the behaviour of the evanescent wave as the mode propagates through the waveguide below it can be studied. Monitors were set inside the simulation to record the electric fields directly above the metal structure, as well as through a cross-section of the wire near the end of the computational cell. Top down, cross-section and perspective views of the structures being simulated, showing the planes over which electric field measurements are taken, the plane of the 2-dimensional source emitting into the waveguide, and the direction in which the source emits, are given in Fig.(3.4).

The simulations described in this thesis were run on 8 2.1 GHz Intel Xeon cores of a computational server running CentOS with 48GB RAM. The length of simulations carried out using this software was found to vary depending on the size of the metal structure emplaced on the waveguide, between 2 to 5 hours. Electric field profiles taken from the region above the metal wire were used to calculate the fluorescent response of atoms above the wire to the evanescent field of resonant light. The effects of the enhanced evanescent wave for the single-photon transition between the 5s and 5p states are discussed in Sec.(4.2). The use of this wave to excite multiple-photon transitions for low-noise fluorescent imaging are also discussed in Sec.(6.2). Finally, we calculate the dipole potentials created by the evanescent field of detuned light travelling through the guide. The results of these calculations are discussed in Chapter 5.

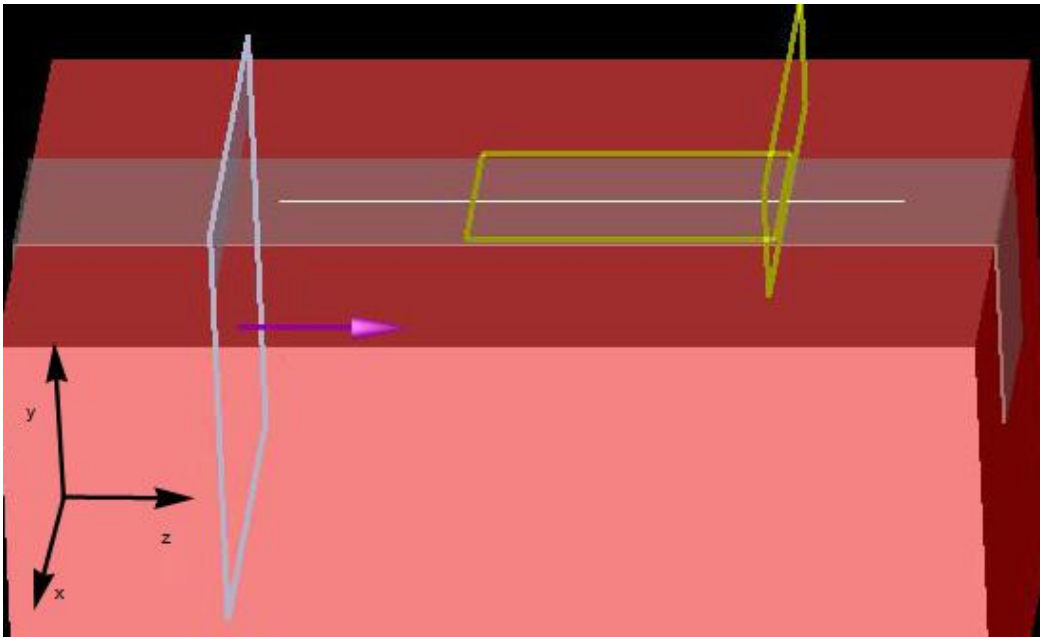

(a)

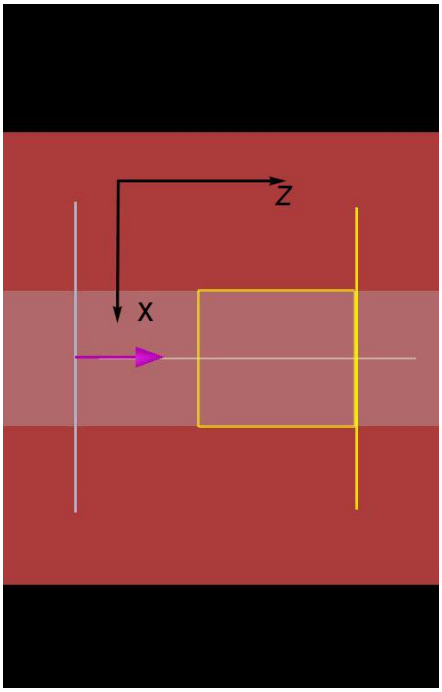

(b)

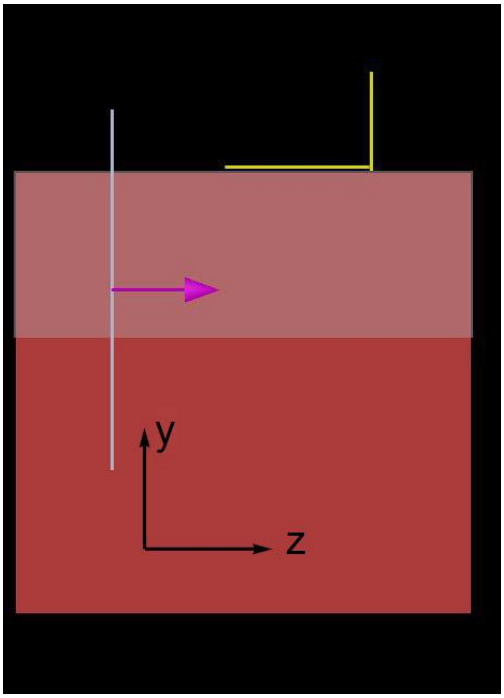

(c)

Fig. 3.4: Perspective (a), top-down (b), and cross-sectional (c) views of structures simulated using Lumerical to calculate the enhancement of the evanescent wave over a waveguide by a thin metal wire. A simulated light source is defined over the region bounded by the white wireframe, emitting down the direction of propagation indicated by the purple arrow. Values of the electric field due to the enhanced evanescent wave are recorded over the regions bounded by the yellow wireframes.

In short, in order to enhance the evanescent field over a waveguide, metal wires are laid over the top surface of the guide. While attempting to simulate such structures using `MEEP`, it was found that carrying out the simulation at the required resolutions required more computer memory than was readily available. Attempts to simulate this system making use of open-source FEM libraries also failed due to the complexity of the programming required. Simulations were finally carried out using the FDTD-Solutions software package from Lumerical Solutions Inc. Using this software package, the evanescent field over the wire due to light propagating through the waveguide underneath was calculated. The effects of the enhanced evanescent wave on the fluorescence of atoms passing over the wire, as well as the dipole force exerted by the evanescent wave of detuned light, are calculated.

4. SIMULATIONS OF WAVEGUIDES AND PLASMONIC STRUCTURES

4.1 Introduction

In previous chapters, we have outlined the motivations behind this project, in particular, the advantages of the integration of optical devices, and the enhancement of such devices through the use of metallic structures to generate strong evanescent fields using surface plasmons, as well as described the numerical methods used to simulate. In this chapter, we first present the results of finite-difference time-domain simulations of light propagating through dielectric waveguides. Simulations are carried out on a series of square waveguides with transverse dimensions between 5 and 10 μm. Changes in the shape of the mode propagating through the guide are tracked using overlap integrals between the end of the guide and various points along its length. The convergence of the mode shape to a confined eigenmode of the waveguide is determined by observation of overlap integrals close to unity over non-zero distances along the length of the guide. From the dimensions of waveguides in which such convergence is found to occur, an estimate is made of the minimum size of a square waveguide capable of supporting a confined mode.

We then present the results of FDTD simulations of a similar waveguide, with the addition of a narrow strip of metal embedded along the centerline of the top surface of that guide. The effects of the enhanced evanescent wave over the wire on the expected fluorescence of atoms passing over the guide are

calculated. In particular, we calculate the peak fluorescence over the centre of the wire against the height over the wire, as well as the enhancement of the rate of fluorescence due to the metal wire relative to the fluorescence induced by the unenhanced evanescent wave over the guide.

4.2 Finite-difference time-domain solutions of the rectangular waveguide

4.2.1 Initialisation of simulations with trial modes

To solve the confined modes of the waveguide, a trial mode is propagated down a simulated waveguide using finite-difference time-domain methods. The shape of the mode at each point along the waveguide is considered to be a sum over a Fourier series of orthonormal components. Fourier components of the trial function that are not part of a guided mode of the waveguide escape the guide and propagate out of the computational cell, leaving behind those components that do match the Fourier spectrum of the guided modes. As the trial mode moves down the guide, therefore, both the Fourier spectrum and the mode shape at each point along the guide become progressively closer to those of the guided modes associated with the guide.

Trial modes are generated by solving the Maxwell Wave Equation in 1D:

$$(\frac{\partial^2}{\partial x^2} + \frac{n(x)^2\omega^2}{c^2})E(x) = \beta^2 E(x) \tag{4.1}$$

along the transverse axes through the centre of the waveguide. The two solutions are then combined to give a trial shape function over the transverse plane of the waveguide. Numerical solutions of the equation are obtained by discretising E along the transverse axis, then solving the eigenvectors of the corresponding matrix representation of the differential operator in Eq.(4.1).

4.2.2 Simulated evolution of waveguide modes along guide

Using the procedure described in Sec.(3.2.3), finite-difference time domain calculations using the trial modes generated from 3.1 were carried out for a series of square waveguides between 5 μm and 10 μm in size. The evolution of the mode as it propagates through the computational cell is investigated by taking the overlap integral between the mode at the end of the waveguide, and the corresponding mode at all other points along the length of the waveguide:

$$\Phi(z) = \int \Psi^*(x, y, z_0)\Psi(x, y, z)dxdy \tag{4.2}$$

where x and y are the transverse coordinates of the waveguide, z is the longitudinal coordinate of the waveguide, z_0 is the value of z at the end of the waveguide, and $\Psi(x, y, z)$ is the value of the mode at a given point. Here, $\Psi(x, y, z)$ and $\Psi(x, y, z_0)$ may be expressed as sums over Fourier series of orthogonal functions. The overlap integral $\Phi(z)$ therefore expresses the degree to which the Fourier components that make up $\Psi(x, y, z)$ are similar to those which make up $\Psi(x, y, z_0)$, and thus the degree to which both the shapes and the Fourier spectra of $\Psi(x, y, z)$ and $\Psi(x, y, z_0)$ begin to resemble each other. Here, we consider a mode to have converged where $\Phi(z) > 0.95$ over a distance greater than 10 μm.

The overlap integral between the mode at z and the mode at the end of the computational cell is small where the two mode functions have very few Fourier components in common, and is close to unity where the Fourier spectrum of the two modes is very similar. Thus, the degree to which the mode changes as it travels from the source to the end of the waveguide can be measured.

Plots of the change in $\Phi(z)$ from the beginning of the waveguide to the end, for waveguides between 5 to 10 μm, are given in Fig.(4.1b). Of par-

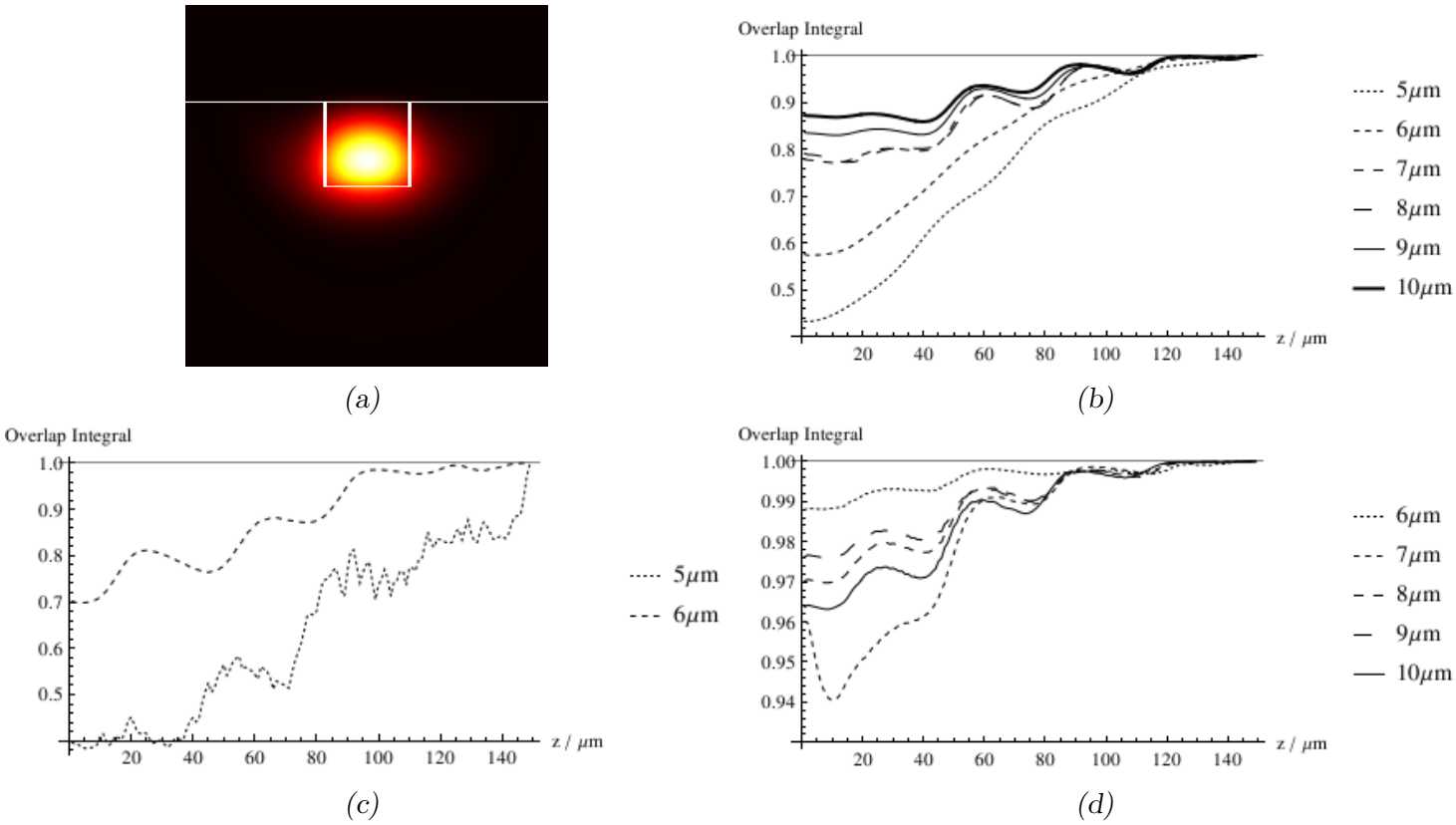

Fig. 4.1: a) Colour plot of the eigenmode of the square waveguide, calculated using FDTD simulations, with waveguide boundaries outlined in white. Modes are propagated down a waveguide, as shown in Fig.(3.2). Plots of the overlap integral between the mode at the end of the waveguide, and the corresponding mode at a point z along the guide, for b) simulations using trial modes generated using the Maxwell wave equation; c) simulations of 5 μm and 6 μm waveguides making use of wave-shapes taken from the end of b); and d) simulations of a 6 μm waveguide using a wave-shape taken from the end of c), and simulations of larger waveguides (between 7 and 10 μm) using wave shapes taken from the end of b).

ticular interest is the behaviour of $\Phi(z)$ as z increases towards the end of the waveguide. Of the waveguides tested, $\Phi(z)$ was found to approach unity closely for the 10-, 9-, 8- and 7-μm waveguides as z approached the end of the computational cell. In the case of the 5- and 6-μm waveguides, not only is the initial value of $\Phi(z)$ small compared to unity (and compared to the starting values for larger waveguides), but $\Phi(z)$ does not approach unity until the very end of the waveguide, where the overlap integral is that of the mode at the end of the waveguide with itself.

To verify the modes obtained from the first set of FDTD simulations, the mode shapes are taken from the end of the computational cell and fed back into the amplitude function of the source in a second set of simulations. This source, with its amplitude function, simulates a mode passing from one section of the waveguide to another, allowing a very long waveguide to be simulated in several shorter steps. The mode arising from the source is propagated through the waveguide a second time, and values of $\Phi(z)$ are calculated and plotted from the simulated results.

Values of $\Phi(z)$ from this second run are plotted in Fig.(4.1c) for the 5 μm and 6 μm waveguides. The modes through both waveguides were found again to vary strongly over the length of the simulation cell. The mode through the 6 μm guide was found to converge after approximately 100 μm, while the mode through the 5 μm guide did not converge at all.

The behaviour of the trial modes propagated through these two guides provides a lower limit for the dimensions of a square waveguide constructed out of differentially-cured SU-8 which is capable of supporting a confined mode. As no convergence was observed, in the case of the 5 μm waveguide, it can be concluded that no guided mode exists for a waveguide of that size. In the case of the 6 μm waveguide, convergence was achieved only after the mode was allowed to propagate over a much longer distance than was necessary in the case of the larger waveguides, from which it may be concluded that, similar to the analytic approximation discussed in Chap.(2), the approximation used to generate trial modes for the waveguide begins to break down as the size of the guide approaches the minimum, allowing strong evanescent fields to extend out of the guide core.

Values of $\Phi(z)$ from the second run of simulations for guides between 7 μm and 10 μm are plotted over z in Fig.(4.1d). The mode of the 6 μm guide is also taken from the end of the second run of simulations and used to create

a trial mode for a third run of simulations, from which the values of $\Phi(z)$ are calculated and displayed on the same plot. Values of $\Phi(z)$ close to unity are recorded across the entire length of the computational cell, for all simulated waveguides, thus confirming that convergence has been achieved, and that the shape of the mode propagating through the guide is close to that of the guided mode.

4.2.3 Analysis and conclusions

By observing the convergence of the mode shape through $\Phi(z)$, we have a rough estimate of the minimum size of the SU-8 waveguide required to support a mode. This value, between 5 and 6 μm, is considerably larger than the free-space wavelength of the light coupled into the guide, and even more so compared to the wavelength of light passing through the guide material. Below this cutoff point, the trial mode instead begins to escape out the bottom and sides of the waveguide[1]. In turn, this causes the field strengths within and around the waveguide core to weaken gradually along the length of the guide.

From Fig.(4.1a) it is also seen that the confined mode travelling through the guide is strongly asymmetric, with the region of highest electromagnetic amplitude located close to the bottom of the guide, strong evanescent waves extending out the bottom and sides of the waveguide core, and very weak fields near the top surface of the guide. This weakness of the fields near the top of the guide is particularly concerning, as the strength of the evanescent wave is critical for the potential applications of evanescent-wave devices discussed elsewhere in this thesis. This concern in turn is particularly exacerbated in the cases where the size of the waveguide does not support a confined mode, in which light escaping out the bottom and sides of the waveg-

[1] One example of this behaviour is seen in Fig.(3.2a)

uide causes the evanescent wave to weaken progressively along the length of the guide. As the strength of the dipole force potentials, and the efficiency of multiple-photon fluorescent detection both depend on the strength of the electromagnetic fields, some means of mitigating this are therefore desired.

The strong asymmetry of the waveguide mode, and the size of the waveguide required to contain it, are functions of the small refractive index contrast between the waveguide core and the cladding surrounding it, especially when compared to the large contrast between the waveguide core and the vacuum. These conditions are imposed on the waveguide by the choice of SU-8 as material with which to construct both the waveguide and its cladding. In turn, this choice of material was made because of the desire to obtain waveguides that could be easily fabricated using materials and equipment available in the wet lab at CQT.

The development of processes, materials or techniques capable of fabricating waveguides with more favorable optical properties is unfortunately beyond the scope of this thesis. Where more advanced materials and techniques become available, however, it is to be hoped that more suitable waveguides, with higher refractive index contrasts between the core and cladding, and thus allowing modes with stronger evanescent waves above the top surface, can be constructed. In lieu of the availability of such techniques, an attempt is made to strengthen the evanescent waves using metal wires implanted on the top surface of the waveguide. Strong evanescent fields are generated using surface plasmons of the metal wire excited by the light passing through the waveguide underneath. The remainder of this thesis concerns FDTD simulations of evanescent waves generated using such structures, and the applications of such waves to neutral atom physics experiments.

4.3 Evanescent-wave enhancement using metallic structures

4.3.1 Simulation and results

For this project, an attempt is made to enhance the evanescent waves travelling over the top surface of a dielectric waveguide by coupling light from the waveguide mode into the surface plasmon polaritons of a thin metallic structure. This consists here of a 100 nm by 20 nm gold wire running down the centreline of a 9 μm square waveguide. As the coupling between the waveguide mode and the surface plasmon depends on the strength of the electric field in the vicinity of the metal wire, we have chosen a sufficiently large waveguide, capable of supporting a confined mode, in order to ensure that the coupling between the waveguide mode and the plasmon remains relatively constant along the length of the guide.

Using Lumerical, simulations of light propagating down this waveguide are carried out over wavelengths between 1000 nm and 700 nm. The shape of the enhanced electric field over the guide is measured and plotted over selected regions within the computational cell. The electric field created using 1000 nm light is measured and plotted over a plane 100 nm above and parallel to the waveguide surface in Fig.(4.2b). The profile of the same field is also measured and plotted over the region of the transverse plane directly above the wire in Fig.(4.2c).

From Figs.(4.2b) and (4.2c), an enhanced evanescent wave can be seen above the wire. This wave varies as a Gaussian in the horizontal transverse direction, while decaying exponentially in the vertical direction. In addition to the enhanced evanescent wave produced by the wire, the unenhanced evanescent wave of the mode travelling through the guide is also seen extending above the guide surface. Like the enhanced wave over the wire, this wave varies as a Gaussian over the width of the waveguide, and decays exponen-

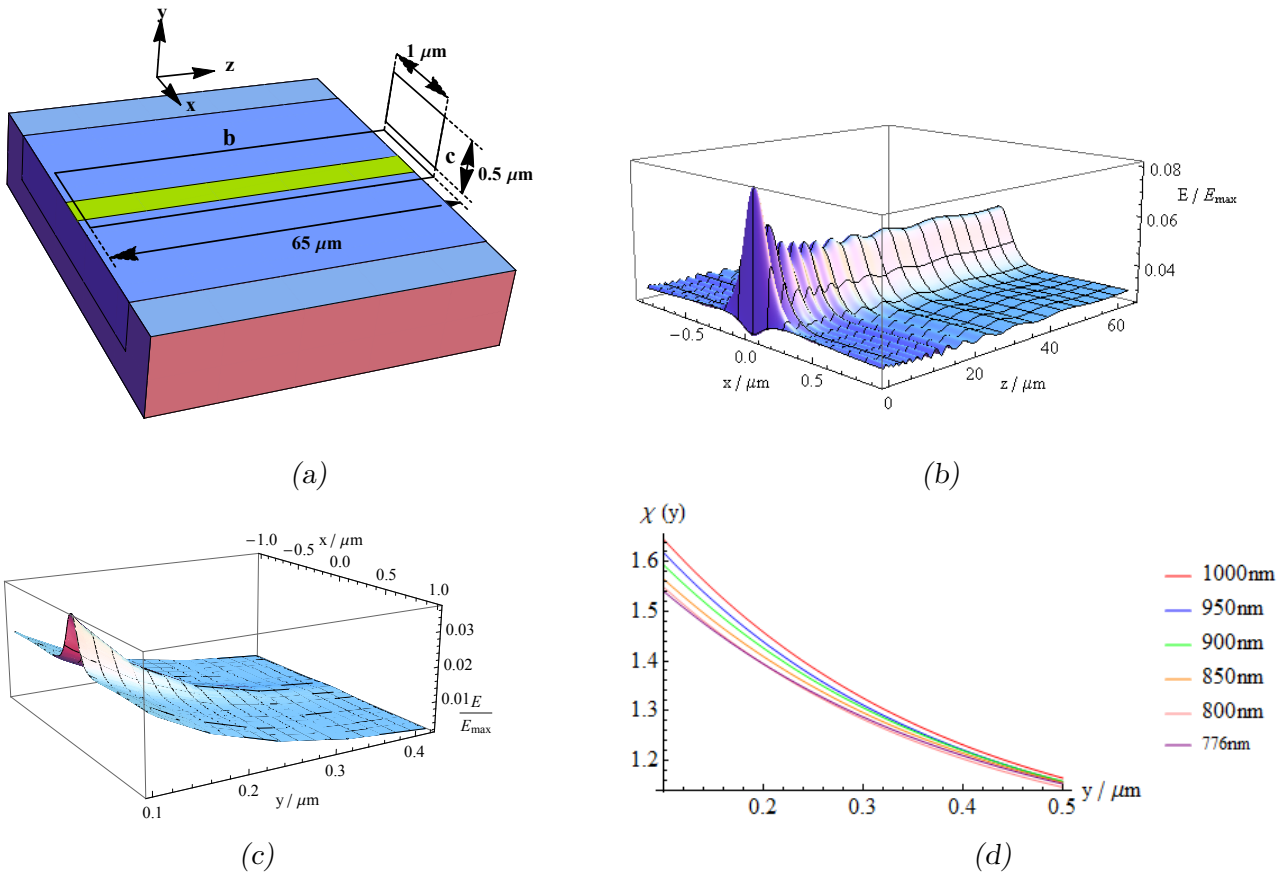

Fig. 4.2: a) Simplified diagram of gold wire over chip. The black rectangles over the chip surface define the regions over which the plots of electric field strength in b) and c) are drawn. b) Plot of electric field strength drawn over the region marked **b** in Fig.(4.2a). c) Plot of electric field strength drawn over the region marked **c** in Fig.(4.2a). d) Plot of χ, the enhancement factor of the evanescent wave above the wire as compared to the strength of the evanescent wave above the bare waveguide.

tially with distance from the guide surface. The total electric field over the waveguide may then be given by an analytical *ansatz* for the sum of these two waves:

$$E(x,y) = E_0 e^{-\frac{x^2}{2w_0^2}} e^{-K_0 y} + E_1 e^{-\frac{x^2}{2w_1^2}} e^{-K_1 y} \tag{4.3}$$

where K_0 and K_1 are decay constants depending on the wavelength coupled through the guide, E_0 and E_1 are amplitude constants for the evanescent wave, and w_0 and w_1 are width constants depending on the widths of the

	K_0 / μm^{-1}					
	1000 nm	950 nm	900 nm	850 nm	800 nm	776 nm
Eq.(2.37)	1.031	1.154	1.301	1.483	1.710	1.840
Data	10.95	11.34	11.75	12.21	12.74	12.95

Tab. 4.1: Table of values of the decay constant k_0 associated with the evanescent wave of surface plasmons in a metal wire for various wavelengths between 1000 nm and 776 nm. Values of k_0 calculated using Eq.(2.37) are recorded in the first row, while values of k_0 obtained from the data are recorded in the second row.

wire and of the waveguide respectively.

Fitting appropriate values of K_0, K_1, w_0, w_1, E_0 and E_1 to Eq.(4.3), we then calculate the enhancement factor $\chi(y)$ of the wave above the wire compared to the evanescent wave of the bare waveguide.

$$\chi(y) = \frac{E_0 e^{-K_0 y} + E_1 e^{-K_1 y}}{E_1 e^{-K_1 y}} \tag{4.4}$$

Values of $\chi(y)$ are plotted in Fig.(4.2d) between $y = 0.1\mu$m and $y = 0.5\mu$m for various wavelengths between 1000 nm and 776 nm coupled through the guide. From Fig.(4.2d), the enhancement factor is seen to be approximately 1.6 close to the waveguide surface, decaying to approximately 1.2 times at $y = 0.5\mu$m.

Values of K_1 are also obtained by fitting Eq.(4.3) to the simulation data for various wavelengths between 776 nm and 1000 nm. The fitted values of K_1 are recorded in Tab.(4.1), along with values of k_y for the same frequencies calculated using Eq.(2.37) for the sake of comparison. The same values are also plotted in Fig(4.3a), along with similar values obtained by fitting Eq. (4.3) to simulation data for a further set of wavelengths between 770 nm and 740 nm. A trial function of the form $K_1 = \sqrt{n/\lambda^2 + m}$ is in turn derived from the expression for the evanescent wave created by a surface plasmon:

$$K_1 = \sqrt{\beta^2 + {K_x}^2 - {K_0}^2} \tag{4.5}$$

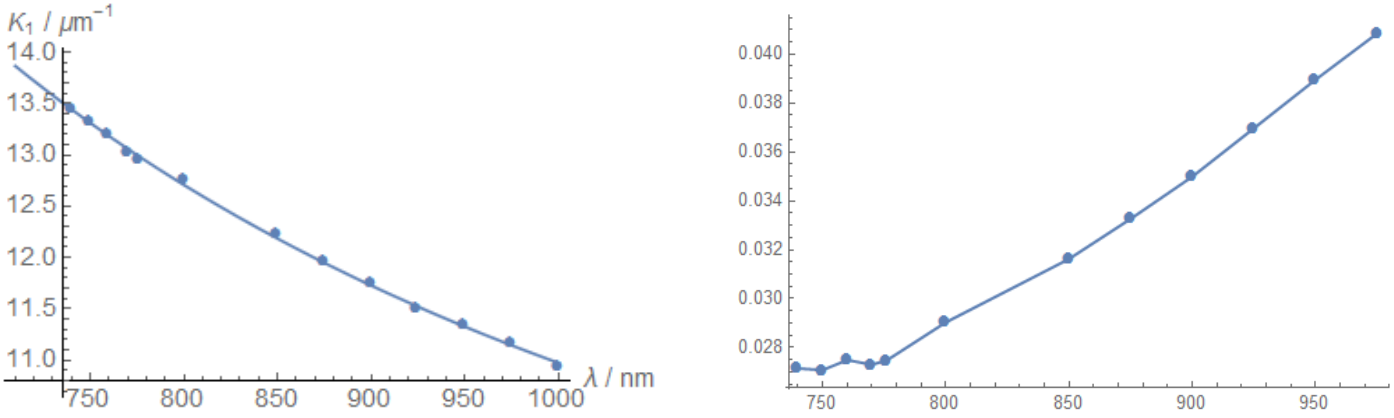

(a) *(b)*

Fig. 4.3: Plots of a),K_1 the decay constant of the enhanced evanescent wave, and b), E_0, the electric field amplitude at the surface of the wire and expressed in terms of E_{max}, the maximum strength of the waveguide mode, obtained by fitting Eq.(4.3) to data obtained from FDTD simulations.

where both β is the wavenumber of the surface plasmon in the direction of propagation, K_x is the wavenumber of the same in the horizontal transverse direction, and K_0 is the vacuum wavenumber. Fitting this expression to the data contained in Fig.(4.3a, an R-squared value of approximately 0.9999, and an Aikake information criterion of approximately -36, indicating a good fit of the model to the data values.

Additionally, in Fig.(4.3b), we also plot the electric field amplitudes obtained from the same fits of Eq.(4.3) to the same data.

It is seen from Tab.(4.1) that the decay constants associated with the evanescent waves over the wires are significantly smaller than those calculated using Eq.(2.37). As will be explained later, in Sec.(4.3.2), this is due to the manner in which the narrow geometry of the wire affects the behaviour of surface plasmons excited by the waveguide mode.

4.3.2 Analysis

The strength of the enhanced evanescent wave produced by surface plasmons in the metal wire depends on the amount of energy coupled from the

waveguide mode into the wire. Integrating the energy density of the electromagnetic wave over the region immediately surrounding the wire, and dividing by the total power coupled into the guide, the proportion of the total power coupled from the mode into the wire is found. For 10 mW of light coupled into a waveguide with 1000 nm wavelength, this proportion is found to be approximately 2.2×10^{-4}. Similarly small amounts of power compared to the total size of the mode are coupled in to the wire by modes of other frequencies. While this is still sufficient to enhance the evanescent wave significantly in the region immediately above the wire, more effective coupling between the mode and the plasmon is still to be desired, such that further enhancement of the evanescent wave is possible.

To some extent, the weak coupling of energy between the mode and the surface plasmon is due to the weakness of the electromagnetic oscillation near the top surface of the waveguide. Simply put, as the bulk of the mode energy is concentrated near the bottom of the guide, very little reaches the wire to be coupled in to the surface plasmon in the first place. Additionally, the narrowness of the thin wire itself contributes to the weakness of the coupling, due to the lack of surface area in which atoms may come into contact with the lower surface of the wire.

Another feature of note in our FDTD simulation is the size of the evanescent waves compared to those predicted by Eq.(2.37). From Tab.(4.1) it is seen that the values of K_1 produced by this simulation are considerably smaller than k_y as given by Eq.(2.37) at similar frequencies. To explain the large discrepancy between these values, some examination of the relationship between the shapes of the wave and the wire is necessary.

To avoid transverse effects on the shape of the evanescent wave , a very narrow wire was chosen for the purposes of the simulations described in this thesis. This has allowed us to obtain a smooth enhanced evanescent

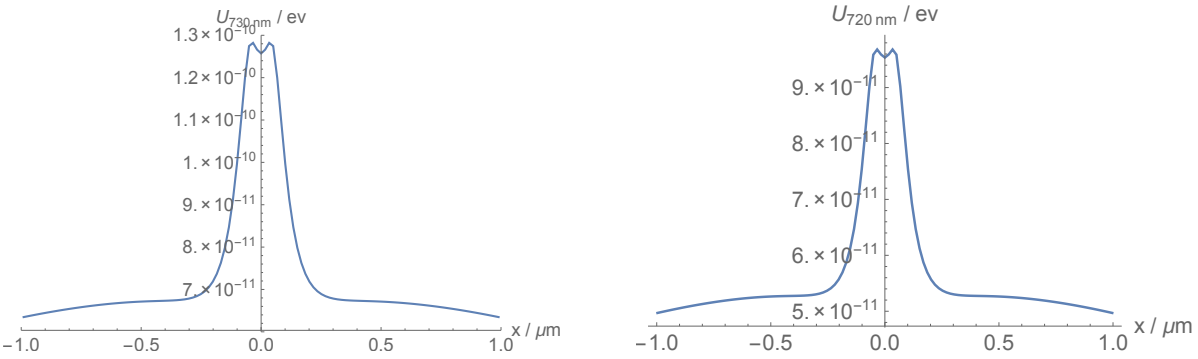

Fig. 4.4: Plots of the transverse wave shapes of evanescent waves above the metal wire produced by light coupled through the waveguide at a) $\lambda = 730$ nm and b) $\lambda = 720$ nm. At these wavelengths, higher-transverse modes of the surface plsamon are excited by the input light. This causes the analytical approximation given in Eq.(4.3) to fail.

wave, which varies as a Gaussian in the horizonal direction. Conversely, the narrowness of the wire has also resulted in a tradeoff in terms of the extent of the evanescent wave above the waveguide.

The minimum width W required to support a surface plasmon polariton on the surface of a rectangular wire is given by [59]:

$$W > \frac{\lambda}{2}\sqrt{\frac{-\left[\epsilon_0 + \mathrm{Re}(\epsilon_1)\right]}{{\epsilon_0}^2}} \tag{4.6}$$

Using values for ϵ given by [54], the minimum width of the wire required to support surface plasmon resonance of the sort described in Sec.(2.5), increases monotonically from 2.3 μm at 776 nm to 3.05 μm at 1000 nm, far larger than width of the wire chosen for this simulation. As such, the only plasmons present within the wire are non-resonant modes driven by the oscillation of light passing through the guide. The narrowness of the wire also adds a large transverse component to the wavevector of the driven plasmons. From Eq.(4.5), it is then seen that the decay constant of the evanescent wave, K_1 also increases with the transverse component K_x, and therefore that the evanescent wave decays more rapidly in vacuum.

As the wavelength of the input modes falls below 740 nm, the analytical expression Eq.(4.3) is found to fail. By inspection of the wave shapes of the evanescent wave at 730 nm and 720 nm, this is due to the presence of higher-order transverse modes of the surface plasmon being excited by the input light (Fig.(4.4)). Conversely, Eq.(4.3) describes only the evanescent wave of surface plasmons in which only the lowest-order transverse mode is excited by the input light. Because of this, wavelengths below 740 nm have been excluded from calculations carried out through the remainder of this thesis.

It can also be seen from Fig.(4.2b) that outside of the first few microns, where considerable oscillations in the electric field are observed, the strength of the enhanced wave remains relatively constant over the length of the wire. This is in contrast to the observations made in [60,61], in which the radiative modes propagating down the wire possessed a finite propagation length, over which the field strength decayed to zero. In the case of the wire over the dielectric waveguide, the field strength remains relatively constant throughout due to the waveguide mode acting as a driving force for plasma oscillations all along the wire.

While the evanescent wave over a narrow wire is both weaker and extends less far into the vacuum above the guide, subsequent chapters will show that it still remains possible to detect atoms above the wire using this wave. From Tab(4.1) and Fig.(4.3a), we also know that while the decay rates of the evanescent waves are far smaller than those associated with a guided mode, the values of these rates decrease predictably as the input wavlength increases. As subsequent chapters will show, one may take advantage of the different decay rates associated with different wavelengths to create dipole potentials in which the attractive or repulsive dipole forces are locally dominant at different locations, in turn allowing dipole potential wells capable of confining atoms within a small volume above the wire to be created. As

will also be shown in those chapters, the large values of K_1 calculated in Sec.(4.3.1) allow very tightly confining dipole potential wells to be created.

For the purposes of carrying out fluorescent imaging of trapped atoms, one may take advantage of the uniform strength of the evanescent wave to illuminate atoms along nearly the entire length of the wire, rather than as they pass through a single point, as in [29–31]. As will also be seen in subsequent chapters, not only does this relatively uniform evanescent wave allow the creation of optical dipole potentials with very tight confinements in the transverse direction, but also, in combination with an atom chip potential created by wires placed underneath the waveguide, much looser confinements in the axial direction. In Chapter 6, we discuss the use of such a potential well to create and manipulate 1-dimensional states of matter.

4.4 Enhanced evanescent waves and trapped atoms–atom fluorescence over the metal wire

Having managed to produce an enhanced evanescent wave using our metal wire, we wish to make use of it. As mentioned previously, one proposed use for such a wave is the illumination of atoms within a very small region for the purpose of low-noise fluorescent imaging. Here, we test the simplest possible implementation of the metal wire for this purpose by calculating the rate of fluorescence of a single rubidium atom illuminated by the evanescent field, generated by a mode near resonance with the 780 nm transition between the $5S_{1/2}$ and the $5P_{3/2}$ energy states[2].

The transverse cross-section of the wave above the wire shown in Fig.(4.2c)

[2] At resonance, the transition becomes saturated at extremely low intensities. While plenty of fluorescence is produced by atoms trapped above the waveguide, very little contrast exists between the region above the waveguide, and the region away from the waveguide. The mode passing through the guide is detuned from resonance in order to increase the saturation intensity and thus the contrast between those areas illuminated by the enhanced wave and those above the bare waveguide.

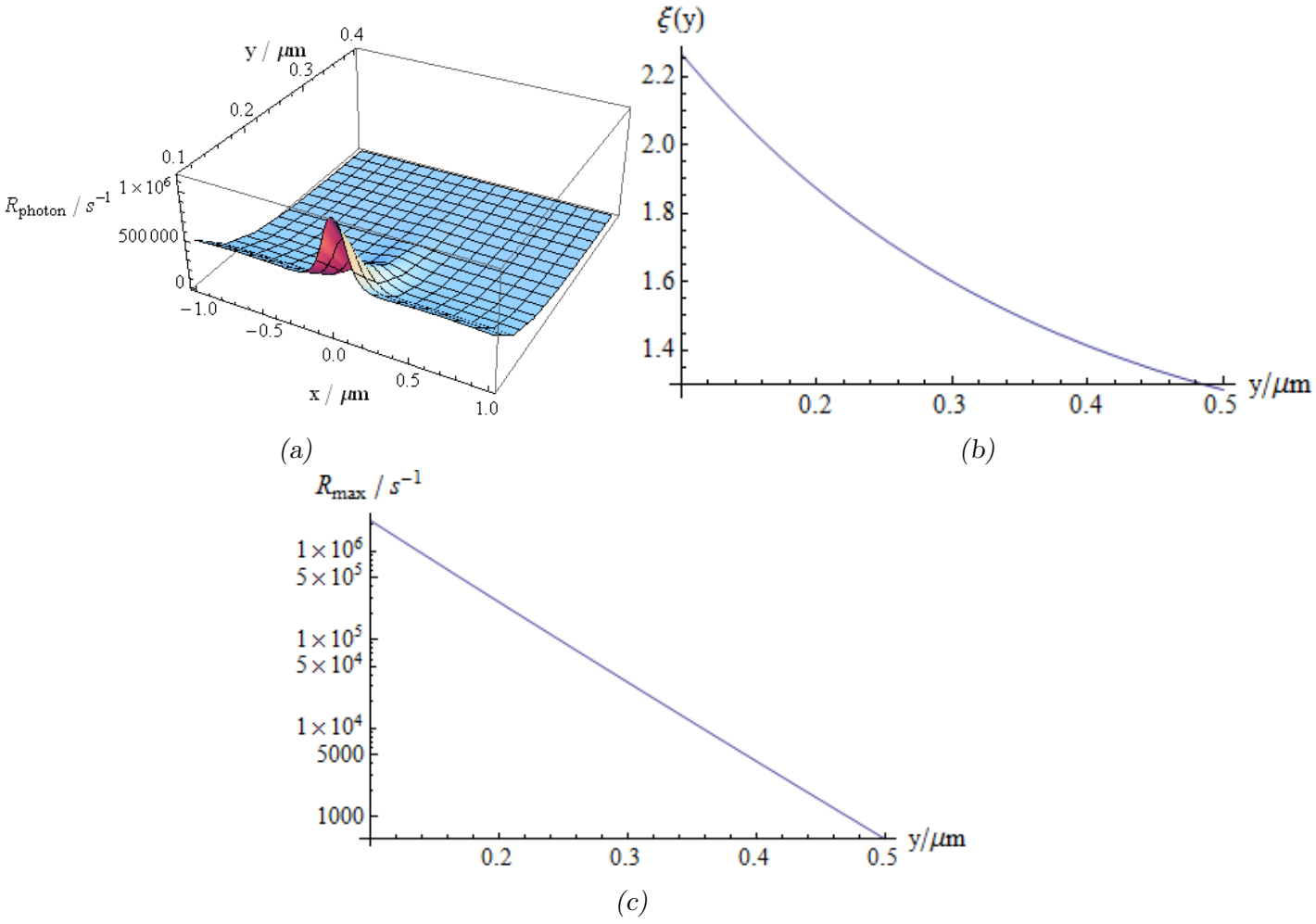

Fig. 4.5: a). 3-d plot of the rate of photons scattered per second from an atom placed inside an evanescent wave generated by resonant (780 nm) light; b). Plot of $\xi(y)$, the contrast observed between the fluorescence of the atom directly above the wire and the fluorescence immediately outside the region affected by the wire; c). Logarithmic plot of R_{photon}, rate of fluorescence over the centre of the wire in terms of photons scattered per second, against the distance of the atom from the waveguide surface.

was renormalised for a total power of 1 μW coupled into the waveguide. The total power scattered per atom at a given point was calculated using the formula:

$$\Delta P = \frac{\sigma(\omega) I}{1 + I/I_{sat}(\omega)} \tag{4.7}$$

where $I_{sat} = (\hbar\omega A_{21})/2\sigma(\omega)$ is the saturation intensity of the transition, $\sigma(\omega))$ is the frequency-dependent absorption cross-section of the transition, given by:

$$\sigma(\omega) = \frac{\Omega^2}{4\delta^2 + \Gamma^2} \frac{\hbar\omega A_{780nm}}{I}, \tag{4.8}$$

and $\Omega = eXE_0/\hbar$ is the Rabi frequency, X is the off-diagonal matrix element between the ground and excited states, E_0 is the electric field amplitude of the incident light, δ is the detuning of the light from resonance, and $\Gamma = A_{780nm}$ is the radiative decay rate from the excited state, equivalent in a two-level system to the Einstein A coefficient between those levels.

Where the incident intensity I is large compared to I_{sat}, Eq.(4.7) approximates to a constant:

$$\delta P \simeq \sigma(\omega) I_{sat} \tag{4.9}$$

Conversely, where I is small compared to I_{sat}, the effective power of light scattered per atom is approximated by:

$$\Delta P \simeq \sigma(\omega) I \tag{4.10}$$

As I increases relative to I_{sat}, therefore, the rate of change of δP falls towards 0, and thus, the effect of the enhanced evanescent wave on the rate of fluorescence is correspondingly decreased. To maximise the effect of our

enhanced evanescent wave, in these calculations, the power coupled through the guide has been set to 1 μW. In turn, this produces an evanescent wave in which I is much smaller than I_{sat}, in which the power of the light scattered of an atom is described by Eq.(4.10), and thus, we obtain the largest possible enhancement of the scattering rate above the atom wire as compared to the bare waveguide.

Dividing ΔP by $\hbar\omega_0$, the total rate at which photons are scattered per atom is found and plotted in Fig.(4.5a), over the same region as in Fig.(4.2c).

To determine the degree to which the fluorescence of the atom is enhanced by the presence of the metal wire, it is first noted that the shape of the data from Fig.(4.5a) may be described using a fitted function similar to that given by Eq.(4.3).:

$$R_{photon} = R_0 e^{-\frac{x^2}{2W_0^2}} e^{-\kappa_0 y} + R_1 e^{-\frac{x^2}{2W_1^2}} e^{-\kappa_1 y} \tag{4.11}$$

where, as in Eq.(4.3), κ_0 and κ_1 are the decay constants of the intensity, W_0 and W_1 are width parameters determined by the size of the metal wire and the guide respectively, and R_0 and R_1 are amplitude parameters of the exponentials. Numerical data on the fluorescence rate of the 780nm transition is calculated from the electric field data produced by the FDTD simulation. The expression in Eq.(4.11) is fitted to the data, and the enhancement factor of the atom fluorescence due to the metal wire, ξ, is calculated using:

$$\xi(y) = \frac{R_0 e^{-\kappa_0 y} + R_1 e^{-\kappa_1 y}}{R_1 e^{-\kappa_1 y}} \tag{4.12}$$

This gives the relative strength of the fluorescence over the metal wire as compared to that over a bare waveguide, which is equivalent here to the contrast observed as an atom crosses the region above the wire.

A plot of ξ over the distance of the atom from the surface of the waveguide,

from 0.1 μm to 0.5 μm, is given in Fig.(4.5b), accompanied by a logarithmic plot of the peak fluorescence over the centre of the wire, plotted over the same domain. From Fig.(4.5b), the fluorescence of the atom is enhanced by the presence of the wire by a factor of approximately 2.25 times at a distance of 0.1 μm, declining exponentially to approximately 1.35 times at 0.5 μm from the waveguide surface. Similarly, the rate at which the atom fluoresces varies from the order of several millions at 0.1 μm from the waveguide surface, to several hundreds at 0.5 μm.

Close to the surface of the waveguide, our evanescent wave atom detector is capable of imaging atoms over the wire with high contrast compared to surrounding regions. This is especially useful in the case of experiments similar to those described in [29] and [31], in which a very small region is probed using tightly-focused light. As in [29] and [31], focusing the incident light in a very small area increases the signal-to-noise ratio of fluorescent imaging within that region(Eq.(2.20), allowing atom clouds to be probed at very high resolutions, down to the level of individual atoms. In contrast to [29] and [31], however, waveguides such as those simulated here may be fabricated over a wide range of heights above the the surface of an atom chip. Previous realisations of 1-dimensional atom clouds with high transverse confinements have been carried out with chip-to-atom distances between 15 [18] to 50 μm [62]. By using the techniques described in Sec.(2.4), it is possible to construct waveguides such that the evanescent field over the plasmonic wire intersects the region in which the atoms are confined, which in turn may be at any height above the chip within the range established by [18] and [62]. Using these methods, atoms confined at closer distances to the atom chip than the radius of an optical fibre may therefore be detected via fluorescent imaging.

5. MANIPULATION OF ATOMS THROUGH METAL-ENHANCED EVANESCENT WAVES

5.1 Introduction

As described in Chapter 4, a metallic wire emplaced over a waveguide is capable of generating a very localised, enhanced evanescent field immediately above it. This field can then be used to manipulate clouds of atoms at high resolutions. In this chapter, one such application of locally enhanced evanescent fields over a metal wire is explored. Starting from simulations of the evanescent field from light coupled into the waveguide at 776 nm wavelength, and also at 1000 nm wavelength, the dipole forces exerted by the detuning of these wavelengths from the 780 nm transition of rubidium are calculated. As these wavelengths are detuned in opposite direction, they exert opposite forces on any atoms above the wire. When both wavelengths are coupled down the same guide simultaneously, the resulting potential is the sum of the individual potentials generated by each frequency. By tuning the relative powers of the beams coupled down the waveguide, this combined potential can then be induced to take the form of a 1-dimensional potential well running directly above the wire.

Having obtained a 1-dimensional potential well, we next calculate he trap depths, the height of the trap over the wire, and the trapping frequencies over a range of values for the strength of the modes coupled into the waveguide. Using a harmonic approximation, the ground state energy levels associ-

ated with the trapping frequencies are calculated, and compared to the trap depths. From this, the number of trapped states available to each potential well is also determined.

The parameters of traps created by coupling other wavelengths of light down the waveguides are also explored and compared with those of the original trap. Finally, a mechanism is proposed for finely controlling the parameters of the trapping potential by superposing potential wells created using different wavelengths over each other.

5.2 The theory of the evanescent wave dipole potential

Before presenting the results of our simulations, we briefly outline the theory describing the behaviour of the evanescent-wave dipole trap. From Eq.(4.3), we know that the strength of the enhanced evanescent wave decreases exponentially with height above the wire. The dipole force potential exerted on a rubidium atom is mainly due to the interaction of incident light with the 5s-5p transition:

$$U_\lambda = \frac{\hbar\Omega^2}{4\delta} \tag{5.1}$$

where $\Omega = eXE_0/\hbar$ is the Rabi frequency; δ is the detuning of the mode from 780 nm, the wavelength of the transtions; e is the electron charge; and X is the transition dipole moment of the 780 nm transition in rubidium[1]. From Eq.(5.1), one can also see that the dipole force potential experienced by an atom in the evanescent field also decreases exponentially with distance over the wire.

When light at two different wavelengths is coupled down a waveguide on which a metal wire has been mounted, each wavelength produces an enhanced

[1] In this thesis, we use $X = 4.227ea_0$, from [63]

evanescent wave above the wire. In turn, the evanescent wave associated with each wavelength exerts a dipole force on atoms trapped above the wire. The total dipole force potential experienced by an atom varies with distance above the wire as the sum of two exponentials:

$$U_{tot} = U_1 e^{-K_1 y} + U_2 e^{-K_2 y} \tag{5.2}$$

where U_1 and U_2 are the strengths of the potential exerted by each wavelength at the wire surface, and K_1 and K_2 are the exponential decay constants associated with the same wavelengths. For two oppositely detuned wavelengths, the combined potential has a minima located at:

$$y_0 = \frac{1}{K_1 - K_2} \ln \frac{-U_1 K_1}{U_2 K_2}, \tag{5.3}$$

forming a potential well with a depth given by:

$$U_{min} = U_1 \left(\frac{-U_1 K_1}{U_2 K_2} \right)^{\frac{-K_1}{K_1 - K_2}} + U_2 \left(\frac{-U_1 K_1}{U_2 K_2} \right)^{\frac{-K_2}{K_1 - K_2}} \tag{5.4}$$

$$= U_2 \left(1 - \frac{K_1}{K_2} \right) \left(\frac{-U_1 K_1}{U_2 K_2} \right)^{\frac{-K_2}{K_1 - K_2}} \tag{5.5}$$

and a vertical trapping frequency given by:

$$\omega = \frac{1}{\sqrt{m_{Rb}}} \left(U_1 {K_1}^2 \left(\frac{-U_1 K_1}{U_2 K_2} \right)^{\frac{-K_1}{K_1 - K_2}} + U_2 {K_2}^2 \left(\frac{-U_1 K_1}{U_2 K_2} \right)^{\frac{-K_2}{K_1 - K_2}} \right)^{\frac{1}{2}} \tag{5.6}$$

$$= \frac{1}{\sqrt{m_{Rb}}} \left[U_2 K_1 K_2 \left(1 - \frac{K_1}{K_2} \right) \left(\frac{-U_1 K_1}{U_2 K_2} \right)^{\frac{-K_2}{K_1 - K_2}} \right]^{\frac{1}{2}} \tag{5.7}$$

where m_{Rb} is the mass of the rubidium atom.

In subsequent sections of this chapter, the characteristics of dipole po-

tential wells generated using evanescent waves of oppositely-detuned modes coupled simultaneously down a waveguide are calculated–in particular, the depth of the trap, as well as the trapping frequencies associated with the potential well. These characteristics are varied, first by adjusting the relative power of modes coupled into the waveguide, and next by coupling light at different wavelengths into the guide. Using these two methods, U_1 and U_2, and in the case of the different wavelengths, K_1 and K_2, may be varied, and in turn, the depth and trapping frequencies of the resulting potential may be adjusted. Here, we examine the changes in these quantities with respect to changes in the power and the wavelength, derive means of comparing and contrasting the performance of these wells under different conditions, and, with the help of the equations above, attempt to explain the behaviour of these wells as those conditions change. Additionally, by use of finite-difference time-domain simulations, we obtain values of K_1, K_2, U_1 and U_2 for a variety of wavelengths coupled through the waveguide, and use these to calculate actual values for the trap depths and transverse frequencies associated with dipole force potential wells created using these wavelengths.

5.3 Simulations of the EM field for 1000 nm and 776 nm light

The fields used in this chapter are obtained by simulating modes of 1000 nm and 776 nm light coupled down identical waveguides, with identical metal wires laid down on top of the guide. Cross-sections of the field surrounding the metal wire are taken from the furthest end of the computational cell. The electric field values are over these cross sections are then normalised for a total power through the waveguide of 10 mW. Using the normalised electric field values, the dipole potential due to the fields are calculated from Eq.(5.1). By inspection, the shape of the dipole force potential over the wire

is found to be similar in form to the expression for electric field strength given in Eq.(4.3), and a similar expression is therefore introduced to describe this potential:

$$U_\lambda(x,y) = U_{max_1} e^{-\frac{x^2}{2w^2}} e^{-k_1 y} + U_{max_2} e^{-k_2 y} \tag{5.8}$$

The expression above is then fitted to the values of the dipole force potential calculated using Eq.(5.1).

From Eq.(5.1) U_λ scales with $|E|^2$, and thus scales linearly with p_λ, the power of the mode coupled into the wire at wavelength λ. Using the expression U_λ obtained by fitting Eq.(5.8) to data calculated from the evanescent field of light coupled into the waveguide at 10mW, it is then possible to calculate the potential due to light coupled into the waveguide at arbitrary P_λ simply by scaling U_λ by the ratio of P_λ to 10m mW. The combined dipole potential due to light of wavelengths 1000 nm and 776 nm coupled into the waveguide is then given by:

$$U_{tot}(x,y) = \frac{p_{1000nm}}{p_n(1000nm)} U_{1000nm}(x,y) + \frac{p_{776nm}}{p_n(776m)} U_{776nm}(x,y) \tag{5.9}$$

where U_{1000nm} and U_{776nm} are the dipole potentials of waveguide modes with wavelength 1000 nm and 776 nm, obtained by fitting Eq.(5.8) to dipole force potentials calculated using Eq.(5.1) from FDTD simulations of light coupled through the guide, with the power coupled into the waveguide normalised at 10 mW. p_{1000nm} and p_{776nm} are the power coupled into the wire from each waveguide mode, and $p_n(\lambda)$ is the power coupled into the wire from a mode with wavelength λ travelling through the guide at 10mW.

Potential wells may be generated by selecting appropriate values for

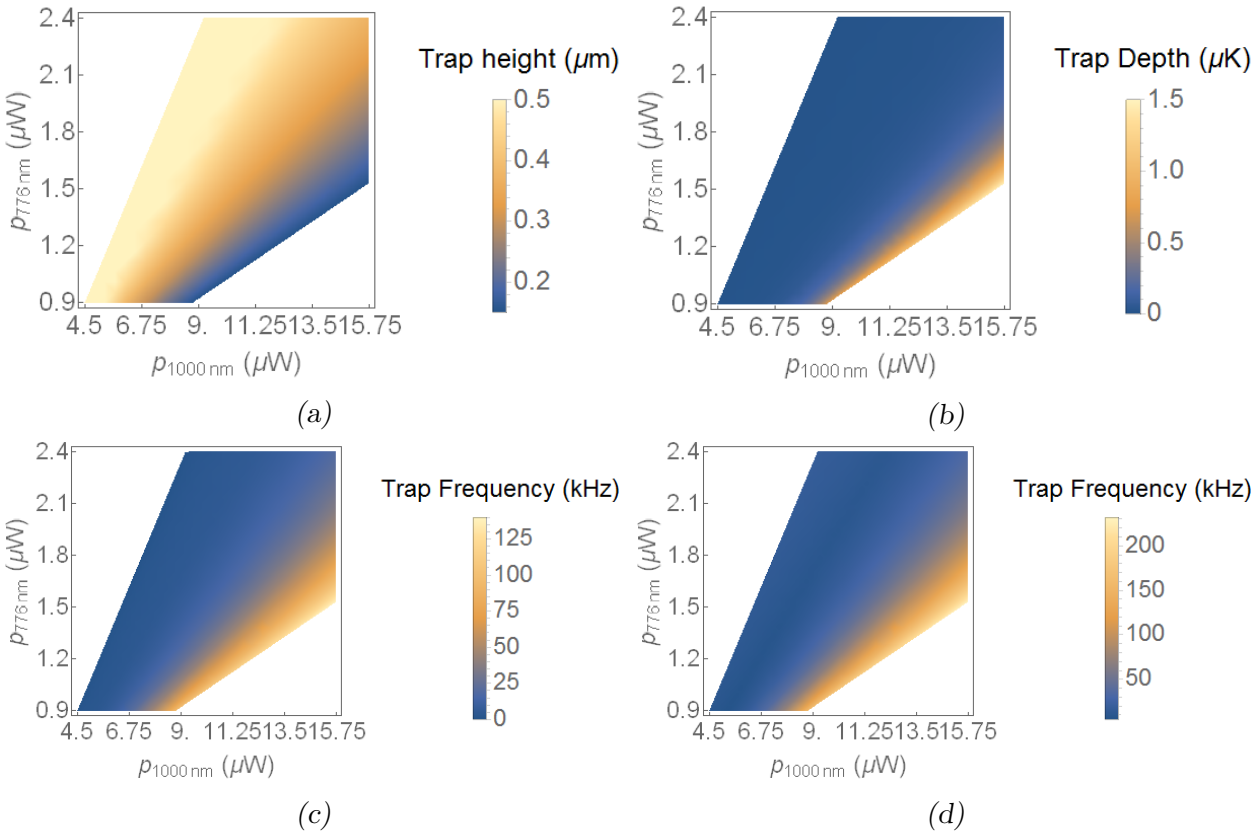

Fig. 5.1: Density plots of the a) the height of the trap minima above the chip surface; b) the depth of the trap in μK; c) the horizontal trapping frequency of the potential well; d) the vertical trapping frequency of the well, plotted in terms of p_{1000nm}, the power of the 1000 nm mode coupled into the metal wire, and p_{776nm}, the power of the 776 nm mode coupled into the wire.

p_{1000nm} and p_{776nm}. The associated minima of wells generated over a range of values of p_{1000nm} and p_{776nm} are located, and the associated trapping frequency of each well is calculated. Density plots of these quantities, expressed in terms of the power coupled into the wire from each mode, are given in Fig.(5.1), with regions in which no potential well exists omitted from the graph.

As atoms approach a chip surface, they begin to experience a van der Waals interaction with said surface. As the strength of this interaction increases as the distance to the chip surface decreases, the attractive force of the interaction can overcome the repulsion of the trapping potential, breaking the atoms out of the trap and pulling them into the chip surface. Those regions of the graph in which the bottom of the potential well approaches closer to the chip surface than 150 nm are therefore also omitted from Fig.(5.1)

From Fig. (5.1), it is seen that, similar to an atom chip trap, as the trapping frequencies are increased, the bottom of the trap moves closer to the waveguide surface. When combined with the minimum separation of 150 nm between the trap bottom and the surface, this imposes an upper limit on the transverse frequency and depth of the trap. Within this limit, however, transverse trapping frequencies of up to 125 kHz in the horizontal direction, determined by the width of the wire, and 250 kHz in the vertical have been achieved, along with maximum trap depths of 1.6 μK. These frequencies are considerably larger than those obtained by previous experiments using atom chips for the tight confinement of 1-dimensional gases, with values ranging from the order of several kHz [17, 44, 64] to the order of several tens of kHz [18], as well as high-frequency optical dipole traps also possessing trapping frequencies on the order of tens of kHz [65]. This is also comparable to the trapping frequencies on the order of hundreds of kilohertz obtained by Kinoshita *et. al.* [39] using a crossed-beam optical lattice of blue detuned

wavelengths.

Conversely, trap depths between 1 to 9 μK have been reported for previous experiments involving 1-d gases on an atom chip [64]. The trap depths observed in Fig.(5.1) exist on the low end of this scale. It should be noted, however, that from Fig.(5.1), the amount of power coupled into the wire due to each mode is only on the order of several μW. By increasing the power coupled into the wire from the waveguide, both deeper and tighter traps than those described by the values quoted here may be attained.

As the value of p_{1000nm} through the wire increases, it becomes possible to achieve higher transverse trapping frequencies and trap depths while still remaining above the 150 nm limit. It is also noted, however, that as the tightness and depth of the trap increase, the trap itself becomes more sensitive to changes in p_{1000nm} and p_{776nm}. From Eq.(5.5), we have:

$$\frac{\partial U_{min}}{\partial U_1} = \left(\frac{-K_2}{K_1 - K_2}\right) {U_1}^{\frac{-K_1}{K_1-K_2}} {U_2}^{\frac{K_1}{K_1-K_2}} \times \left[\left(\frac{-K_1}{K_2}\right)^{\frac{-K_1}{K_1-K_2}} + \left(\frac{-K_1}{K_2}\right)^{\frac{-K_2}{K_1-K_2}}\right] \quad (5.10)$$

and:

$$\frac{\partial U_{min}}{\partial U_2} = \left(\frac{K_1}{K_1 - K_2}\right) {U_1}^{\frac{-K_2}{K_1-K_2}} {U_2}^{\frac{K_2}{K_1-K_2}} \times \left[\left(\frac{-K_1}{K_2}\right)^{\frac{-K_1}{K_1-K_2}} + \left(\frac{-K_1}{K_2}\right)^{\frac{-K_2}{K_1-K_2}}\right] \quad (5.11)$$

Let us consider the case in which $K_1 > K_2$. U_1 is then identified as the repulsive component of the combined potential, and U_2 is the attractive component. From Fig(5.1), we know that the bottom of the potential well

approaches the waveguide surface as U_2 increases and U_1 decreases. Furthermore, by inspection of Eqs.(5.10) and (5.11), we know that the gradients $\partial U_{min}/\partial U_1$ and $\partial U_{min}/\partial U_2$ also become large for large U_2 and small U_1. Under such conditions, the potential well becomes very sensitive to perturbations such as trap noise. To safely trap atoms within a potential well created using the evanescent waves of oppositely detuned waveguide modes, very stable laser sources are therefore required in order to avoid such large perturbations in the trapping potential.

In summary, by coupling two oppositely-detuned frequencies of light down the same waveguide, it is possible, by tuning the relative powers of those frequencies, to create a potential well using the dipole potentials induced by the wire-enhanced evanescent waves. Using this method, it is possible to achieve high trapping frequencies. However as the frequency increases, the potential becomes more sensitive to perturbations. Thus, stable power sources are required to avoid unwanted excitations of atoms within the trap.

5.4 The dipole potential well and the harmonic approximation

It has been established in the previous section that potential wells with strong trapping frequencies may be realised using a dual-wavelength evanescent wave dipole trap. The depth of the dipole potentials relative to the power coupled into the metal wire is also found to be on the order of several μK for several tens of μW. However, the characteristics of the potential well at a given power also depend heavily on the relative powers of the red- and blue-detuned wavelengths that are coupled into the wire.

Before continuing, it is necessary to digress shortly regarding the approximation we have made in order to assess the energy level characteristics of

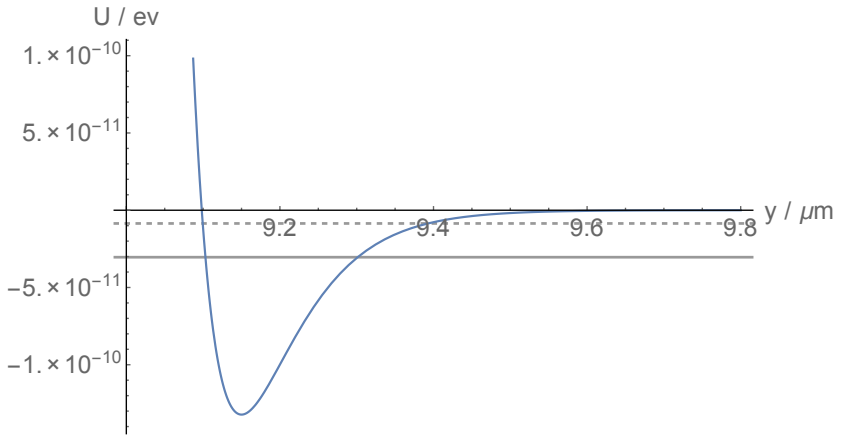

Fig. 5.2: Plot of the combined dipole force potential along the y-axis created by enhanced evanescent waves of red- and blue-detuned modes over a metal wire. The dashed horizontal line indicates the ground state energy obtained by treating the dipole potential as a harmonic potential well, while the solid line indicates the ground state energy obtained by solving Schrodinger's equation numerically in this potential.

trapped atoms in a potential well. In this thesis, we have used the formula for the energy levels of trapped states in a harmonic potential as a convenient means of estimating the energy levels of the ground state of trapped atoms:

$$E_{n_x n_y} = (n_x + \frac{1}{2})\hbar\omega_x + (n_y + \frac{1}{2})\hbar\omega_y \tag{5.12}$$

It must also be noted, however, that due to the shallowness of the trap, atoms within the trap do not truly experience a harmonic potential, even within the ground state. In turn, this affects the value of the energy associated with each trapped state. As can be seen in Fig.(5.2), the true value of the ground state energy, obtained by solving Schrodinger's equation for a rubidium atom trapped in the dipole potential well, is significantly lower than that predicted by the harmonic approximation.

Conversely, it is far less complicated computationally to extract the harmonic frequencies of a dipole potential well before using those to calculate the energy of the ground state than it is to numerically solve the Schrodinger equation for what may possibly be a large eigensystem before extracting the

correct eigenvalues from a large set of solutions. This is especially true when it is necessary to determine the characteristics of potential wells over a large range of values for p_{1000nm} and p_{776nm}. From Fig.(5.2), the ground state energy obtained from the harmonic approximation is slightly larger, though still relatively close to the value obtained by solving Schrodinger's equation numerically. Thus, for the sake of simplicity, in this thesis we have used the harmonic approximation as a reasonable, though conservative estimate of the ground state energy.

Returning to the matter of the number of trapped states which can be supported in a given dipole potential well, we recall from Eqs.(5.5) and (5.7) that the depth of the potential well increases linearly with p_{1000nm} or p_{776nm}, while the transverse trapping frequencies increase with the square root of p_{1000nm} and p_{776nm}, and that consequently, the transverse trapping frequency is proportional to the square root of the trap depth. Similarly, the ground state energy of atoms trapped within the well also varies with the square root of the power coupled into the guide.

Using the ratio of trap depth to the ground state energy predicted by the harmonic approximation, one may make a rough estimate of the values of p_{1000} relative to p_{776} that allow a trapped state to exist. The minimum values of p_{1000} and p_{776}, and the relative sizes of in these quantities at which a trapped state can exist, are found by plotting Fig.(5.3b) over the region in which the ratio of trap depth to the harmonic ground state energy is greater than 1.

Having studied the characteristics of potential wells created using two oppositely-detuned waveguide modes, we now wish to optimise the trapping characteristics of these wells. As shown in previous sections, one may increase both the depth and the trapping frequencies associated with the potential well simply by increasing the power coupled into the waveguide.

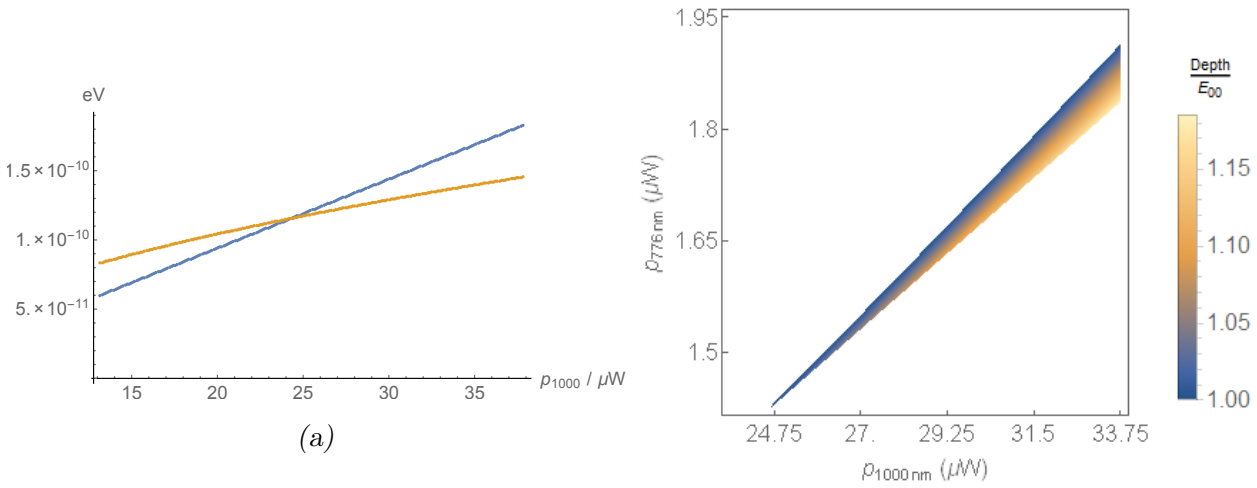

Fig. 5.3: a)Plots of the ground state energy and the trap depth against p_{1000nm} calculated using the harmonic approximation for a dipole potential well with a bottom located at $y = 150$nm; b) Density plot of the ratio of trap depth to ground state energy, plotted around the point at which this ratio crosses over from less than unity to greater than unity. For clarity, only those regions in which the ratio of trap depth to ground state energy exceeds unity, and in which the bottom of the trap is further than 150nm from the surface are included in the plot.

Alternatively, however, from Eqs.(5.5) and (5.7), one may instead attempt to optimise the trap depths and trapping frequencies associated with the evanescent wave dipole trap by adjusting the wavelength of light coupled in to the waveguide. In the next section, we investigate the effects on the characteristics of the well of changing the wavelengths of the input modes. Characteristics of potential wells created using wavelengths of red-detuned light between 1000nm and 850nm and of blue-detuned light between 740 and 776 nm are calculated, and compared with those associated with the potential wells previously investigated.

5.5 Potential wells using alternative wavelengths

5.5.1 Introduction

Having examined the characteristics and the feasibility of our dipole trapping potential using light coupled into the waveguide at 1000nm and 776nm, we now wish to conduct a more general survey on the characteristics of dipole potentials produced using different wavelengths. In this section, two sets of simulations are carried out. First, a set of dipole potential wells are simulated in which the repulsive potential is provided by blue-detuned light at 776nm, while the wavelength of the red-detuned light is varied between 1000nm and 850nm. Next, we simulate a set of dipole potentials in which the wavelength of the red-detuned light is held at constant at 1000nm, while that of the blue-detuned light is varied between 740nm and 776nm

To provide a numerical basis for this comparison, and taking the data calculated and displayed in Figs.(5.1) and (5.3b) as a basis, several characteristic quantities are proposed that may be derived from the behaviour of the potential well. First, it is noted that the lower right portions of the graphs displayed in Figs.(5.1) and (5.3b) are cut off, as the values within those regions are associated with potential wells in which the trap bottom is less than 150nm above the wire. The edge of this cutoff therefore corresponds to the line along which the height of the trap bottom above the chip surface is 150nm. From Eq.(5.3), one may see that in order to maintain constant y_0 as U_1 and U_2 increase, the ratio U_1K_1/U_2K_2 must remain constant. We also recall from Eq.(5.1) that U_λ, the potential experienced by an atom due to the evanescent wave associated with the mode with wavelength λ, scales linearly with p_λ, the power of the mode coupled through the guide. From these observations, and by inspection of the cutoff line in Figs.(5.1) and (5.3b), one may conclude that this line therefore corresponds to a linear relationship

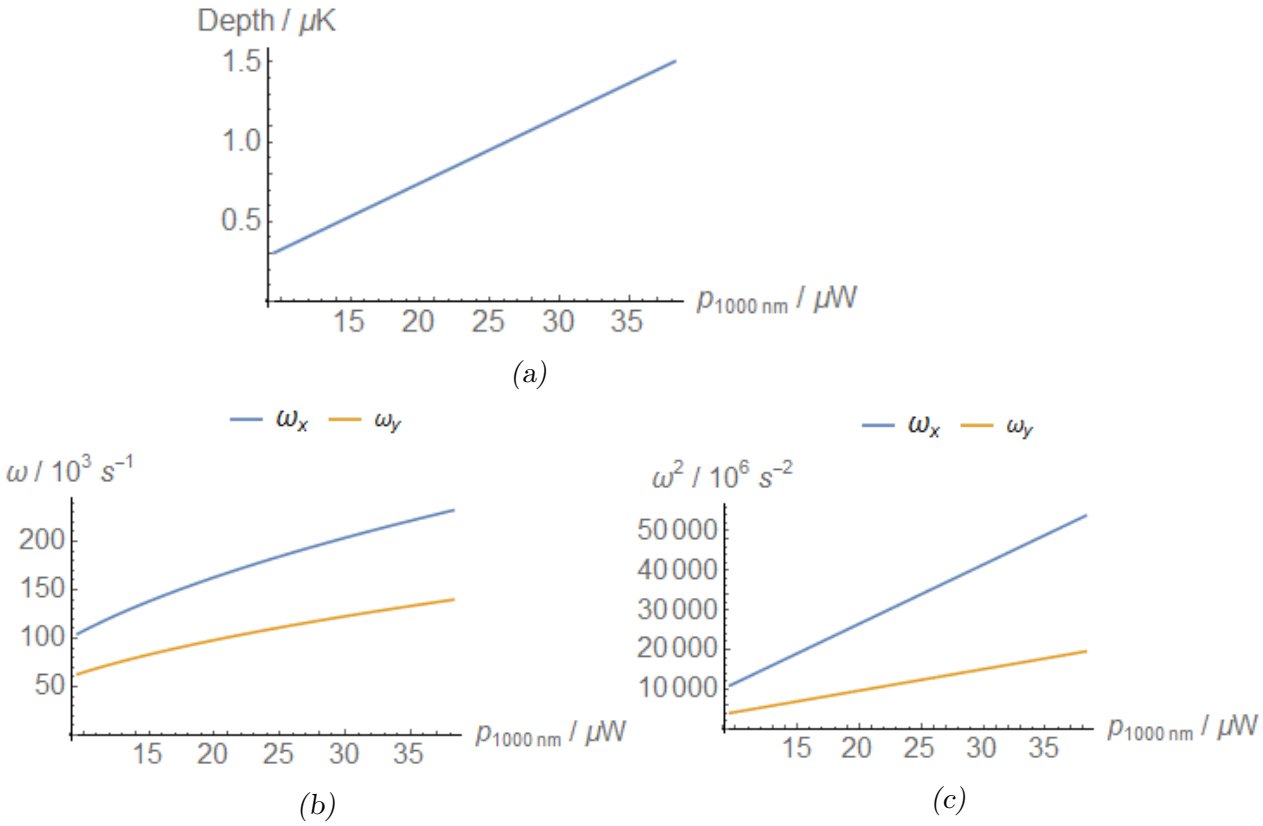

Fig. 5.4: Plots of a). the trap depth, in μK; b) the transverse trapping frequencies; and c) the squares of the transverse trapping frequencies, plotted along the line in Figs.(5.1) and (5.3) corresponding to those values of p_{1000nm} and p_{776nm} at which the trap bottom is 150nm away from the chip surface. As this line is defined by a linear relationship between p_{1000nm} and p_{776nm}, these values can simply be plotted against the corresponding value of p_{1000nm} or p_{776nm}. Here, the data is plotted against p_{1000nm}. Similarly, gradients of the lines in (5.4a) and (5.4c) may also be calculated against p_{1000nm}

between p_{1000nm} and p_{776nm}.

It is also observed that the trap depth appears to increase linearly along this line, while the transverse trapping frequencies associated with the potential well appear to increase as square root functions along the same line (Fig.(5.4)). In turn, this agrees with the expressions for U_0 and F given in Eqs.(5.5) and (5.7).

From these observations, we therefore propose that the quantities used to characterise the behaviour of the dipole traps be derived from the gradient

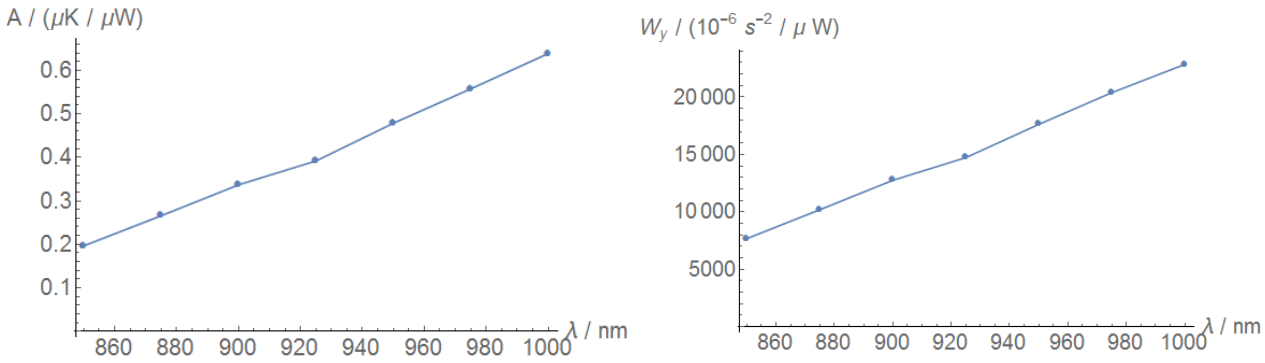

Fig. 5.5: Plots of partial derivatives characterising the behaviour of dipole traps created using oppositely-detuned waveguide modes. Here, the blue-detuned wavelength of light is held constant, while the red-detuned mode through the waveguide is varied at 50nm intervals between 850 and 1000nm. Values plotted here are: a) A, the partial derivative of the trap depth, and b), W_y, the partial derivative of the square of the transverse frequency in the vertical direction. All partial derivatives are calculated relative to p_{776nm}, the power of the blue-detuned mode coupled through the waveguide.

of the trap depth along the line corresponding to a trap height of 150nm, as well as the gradient of the square of the trapping frequencies along the same line. As this line is defined by a linear relationship between p_{1000nm} and p_{776nm}, the calculation of our characteristic quantities may be simplified by mapping a given point on the line to the corresponding value of p_{1000nm} or p_{776nm}. Using this mapping, our characteristic quantities can then be found by taking the partial derivative of the trap depth or the square of the frequency with respect to p_{1000nm} or p_{776nm}.

5.5.2 *Characteristics and behaviour of potential wells using different wavelengths*

In this section, we study the trap depths and frequencies of potential wells where the wavelength of blue-detuned light is held constant at $\lambda = 776$nm, while the wavelength of the red-detuned light is varied at 25nm intervals between 800 nm and 1000 nm. Similarly, we also calculate the trap depths and

trapping frequencies of potential wells in which the wavelength of red-detuned light is held constant at 1000 nm, while the wavelength of blue-detuned light is varied at 10nm intervals between 770nm and 740nm. To provide some basis whereby potential wells formed using different wavelengths may be compared to each other, we propose the figures of merit A and W_y, where:

$$A(\lambda_a) = \frac{\partial U_{min}}{\partial p_{\lambda_b}} \tag{5.13}$$

and

$$W_y(\lambda_a) = \frac{\partial \omega}{\partial p_{\lambda_b}} \tag{5.14}$$

Here, λ_b refers to the wavelength of the input mode which is held constant, while λ_a refers to the wavelength of the oppositely-detuned mode which is varied in each set of calculations. Plots of A and W_y are for the case where the blue-detuned light is held constant at 776 nm and the wavelength of the red-detuned mode is adjusted between 1000 nm and 850 nm are given in Fig(5.5).

From Figs.(5.5a) and (5.5b), we find A and W_y both increase linearly with λ, the wavelength of the red-detuned mode. In concrete terms, this means that the depth of the well increases faster with p_{776nm} as the wavelength of the red-detuned light moves farther from resonance. Similarly, the transverse trapping frequencies of the potential well also increase faster with p_{776nm} as the red-detuned light is moved further from resonance.

We next calculate the trap depths and frequencies associated with potential wells created using red-detuned light held constant at $\lambda = 1000$nm, while varying the wavelength of blue-detuned light at 10 nm intervals between 740 nm and 776 nm. The partial derivatives A and W_y for this set of simulations are calculated relative to p_{1000nm}, and recorded in Fig.(5.6).

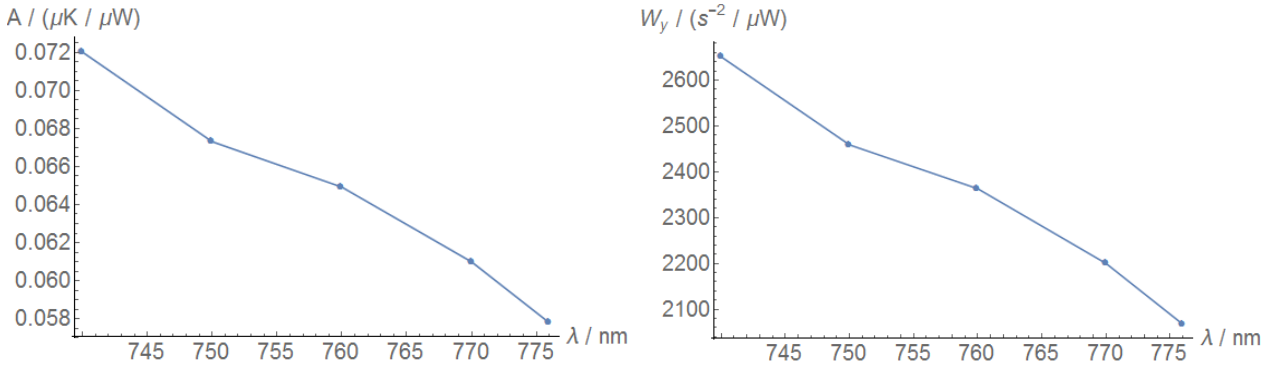

Fig. 5.6: Plots of partial derivatives characterising the behaviour of dipole traps. In this plot, the red-detuned wavelength of light is held constant, while the wavelength of the blue-detuned light is varied in 10 nm intervals between 740 nm and 776 nm. As in Fig.(5.5), the values plotted here are: a) A, the partial derivative of the trap depth, and b), W_y, the partial derivative of the square of the transverse frequency in the vertical direction.

Similar to the behaviour observed in Fig.(5.5), A and W_y increase monotonically as the blue-detuned light is moved further from resonance. As in the case of the red-detuned light, the depth and the trapping frequency associated with the potential well increase faster with p_{1000} as the wavelength of the blue-detuned light is moved away from resonance.

By maximising the detuning of the waveguide modes, one maximises not only the transverse trapping frequencies associated with that potential well, but also the depth of the trap. More importantly, we know from Eqs.(5.5) and (5.7) that the trap depth varies linearly with the power coupled into the guide and that the trapping frequency varies with the root of the power. By increasing the detuning of the waveguide modes in either direction, not only are the transverse frequencies and the trap depth maximised, but also the ratio of the trap depth to the ground-state energy of atoms trapped within the well. In turn, this minimises the probability of atoms escaping from the potential well. From the evidence of the results presented here, therefore, one may optimize the characteristics of an evanescent wave dipole potential

well by making use of waveguide modes that are detuned as far as possible from resonance in both directions.

5.6 Conclusion

In this chapter, we have made use of the results of FDTD simulations of the enhanced evanescent wave of light detuned from resonance above a metal wire to calculate the dipole force potentials exerted by the evanescent wave on a rubidium atom. By combining evanescent waves created by two separate wavelengths of light, each detuned in opposite directions from resonance, a cylindrical dipole force potential well may be created above and parallel to the metal wire. The characteristics of this potential well, such as the trap depth, the distance of the trap bottom from the waveguide surface, and the transverse trapping frequencies, may be manipulated by adjusting the power of the red- and blue-detuned waveguide modes relative to each other.

First, we calculate the characteristics of a dipole potential well created using the enhanced evanescent waves of 1000 nm and 776 nm light coupled down the same waveguide. The trap depths and transverse trapping frequencies of the potential created by linear combinations of the potentials of these evanescent waves are calculated from analytical approximations fitted to the data over a range of values for the power of each wavelength coupled down the guide. To minimise loss of atoms from the potential well via van der Waals interactions with the surface of the wire, a minimum separation of 150nm is imposed between the trap bottom and the surface. Conversely, both the trap depth and the transverse trapping frequencies increase as the separation between the trap bottom and the wire surface decreases.

Having calculated the characteristics of dipole potential wells created using the evanescent waves of two oppositely-detuned modes of light, we then

investigate the way in which those characteristics affect the trapping performance of the well. In particular, we investigate the energy-level spectrum available to atoms trapped within a given potential well. Using a harmonic approximation, the ground-state energies of the potential well are calculated from the transverse trapping frequencies and compared to the trap depths over a range of input powers for the two modes of light.

Having studied the characteristics of dipole potential wells created using evanescent waves of light at 1000 nm and 776 nm, we next study the characteristics of dipole potential wells created using different wavelengths of light. To obtain some means of comparison between potential wells created using different wavelengths, it is proposed to use A, the partial derivative of the trap depth relative to the input power of one of the modes, and W_y, the partial derivative of the squares of the transverse trapping frequencies relative to the same input power. First, red-detuned modes of light between 850 and 1000 nm are tested, while the wavelength of the blue-detuned mode remains constant at 776 nm. From these calculations, it is found that both A and W_y increase linearly as the wavelength of the red-detuned mode increases. In physical terms, this means that it is possible to generate a deeper, tighter potential well for a given input power using a longer wavelength than it is using a shorter one.

The characteristics of dipole potential wells in which the red-detuned wavelength is held constant, while the blue-detuned wavelength is gradually moved away from resonance are also investigated. Calculations are carried out for potential wells created using blue-detuned modes of light between 740 and 776 nm, and a red-detuned mode held constant at 100 0nm. Just as in the previous set of calculations, it was found that, as the blue-detuned light moved further from resonance, A and W_y increased. Taking the results of the previous two paragraphs together, it therefore appears that one may optimise

a dipole potential well created using evanescent waves of oppositely-detuned waveguide modes by using the widest available detuning of those modes.

6. FUTURE APPLICATIONS OF THE EVANESCENT WAVE DEVICE

6.1 Introduction

As seen in Chapters. 4 and 5, metal wires over waveguides are capable of producing enhanced evanescent fields within a small region, and furthermore, when modes of two different frequencies are coupled down the same waveguide, each frequency being detuned in the opposite direction from a selected transition, the dipole potentials induced by each mode over the wire combine to form a very tight, one-dimensional potential well over said wire. In this chapter, potential applications of this device are discussed, in particular the use of the enhanced evanescent wave to excite multiple-photon transitions for the purposes of low-noise fluorescent imaging of atoms, as well as the use of the tightly-confining potential described in Chapter. 5 to create a Tonks-Girardeau gas, a unique state of matter consisting of a string of tightly confined in a 1-dimensional potential.

Firstly, we discuss the use of the enhanced evanescent wave to excite transitions between the 5s state of rubidium and the 4d state via a two-photon absorption process. Fluorescence caused by spontaneous emission from these excited states produces photons with different energies from the incident photons. Photons scattered from other sources can then easily be filtered out of the captured image of the atoms, thus removing noise from that image. The rates of fluorescence produced by spontaneous emission

from the excited state are calculated for the two-photon transition, in order to assess the feasibility of carrying out imaging of trapped atoms using these transitions.

Secondly, the characteristics of the tightly-confining 1-dimensional potential calculated in Chapter 5 are analysed. In particular, the transverse dimensions of the potential, $a_\perp$, and the 1-dimensional scattering length of rubidium in that potential, a_1 are derived from the transverse trapping frequencies. Values of γ, a dimensionless parameter that depends on $a_\perp$, a_1, and the 1-dimensional density of atoms, and which characterises the states of atom gases in 1-dimensional potentials, are taken from experimental realizations of a Tonks-Girardeau gas [39, 40]. Comparable values of γ are derived from the values of $a_\perp$ and a_1 obtained in Chapter 5, and the maximum atom densities required to achieve those values are compared to the observed values from [40] and [39]. Finally, we discuss the integration of atom chip structures with the evanescent-wave dipole trap, in particular, the use of such structures to manipulate trapped atoms and their parameters along the axial direction.

6.2 Fluorescent atom imaging using multiple-photon resonances

6.2.1 Introduction

From Chapter. 4, the metal wire above the waveguide is capable of enhancing the evanescent wave within a small region over the centerline of the guide. In that chapter, the use of this enhanced wave to in turn locally enhance the rate of fluorescence over the wire was investigated. By passing trapped atoms across the wire and observing the change in fluorescence as they pass through the enhanced evanescent wave, experiments such as single-photon detection, correlation measurements of trapped atoms, and atom spectroscopy may be

carried out, in a similar manner to those described in [29, 31]. In contrast to [31] and [29], the waveguide may be fabricated at an arbitrary distance over the chip wires, allowing atoms to be illuminated at similarly arbitrary distances from the chip surface.

While use of the enhanced evanescent wave above the wire to perform fluorescence imaging of atoms may allow trapped atom clouds to be imaged at high resolutions, even down to the level of single atoms, the quality of images obtained using this method may remain less than ideal. In particular, noise is introduced to the image by the scattering of photons from sources other than the atoms, such as from defects on the waveguide surface. In addition to this, as the atoms move further from the waveguide surface, the contrast between the fluorescence over the wire and the fluorescence away from the wire decreases. Two things therefore are desired–first, that some means be found of distinguishing between photons scattered from atoms and photons scattered from other sources, and secondly that some means be found of increasing the factor by which the fluorescence of those atoms is enhanced by the wire. One possible method of accomplishing this is to make use of multiple-photon resonances between atomic energy levels. Two or more photons are absorbed by atoms to induce a single transition to an excited state, which then decays, emitting a single photon possessing the combined energy of the absorbed photons. Photons scattered off other sources retain their original energy, and thus can be easily filtered out of the image, eliminating any noise due to said scattering. Furthermore, as will be shown below, the effective Rabi frequencies of these transitions scale nonlinearly with the incident intensity. The response of such transitions to a slight increase in the intensity is therefore stronger than the response associated with a direct transition.

In this section, we study the use of the enhanced evanescent wave to

induce multiple-photon transitions. In particular, we consider the absorption of two photons of wavelength 1032 nm to excite electrons from the 5s to the 4d state of rubidium by stimulated Raman passage, with the 5p state acting as an intermediate level.

6.2.2 Stimulated Raman passage via the enhanced evanescent wave

Let us consider a three-level atom with ground and excited states $|1\rangle$ and $|2\rangle$, with an intermediate state $|i\rangle$ between them, and illuminated by light at frequency ω. The atom experiences a Hamiltonian given by:

$$i\hbar\frac{d\psi}{dt} = -\frac{\hbar^2}{2m}\nabla^2\psi + e\mathbf{r}\cdot\mathbf{E}_0\cos(\omega t)\psi \tag{6.1}$$

or, in matrix form,

$$i\hbar\frac{d}{dt}\begin{pmatrix} A_{|1\rangle}(t) \\ A_{|i\rangle}(t) \\ A_{|2\rangle}(t) \end{pmatrix} = \mathscr{H}\begin{pmatrix} A_{|1\rangle}(t) \\ A_{|i\rangle}(t) \\ A_{|2\rangle}(t) \end{pmatrix} \tag{6.2}$$

$$= \begin{pmatrix} E_{|1\rangle} & u_{1i}\cos(\omega t) & 0 \\ u_{i1}\cos(\omega t) & E_{|i\rangle} & u_{i2}\cos(\omega t) \\ 0 & u_{2i}\cos(\omega t) & E_{|2\rangle} \end{pmatrix}\begin{pmatrix} A_{|1\rangle}(t) \\ A_{|i\rangle}(t) \\ A_{|2\rangle}(t) \end{pmatrix} \tag{6.3}$$

where $u_{jk} = E_0 X_{jk}$, and X_{jk} is the transition dipole moment between the states $|j\rangle$ and $|k\rangle$.

Perturbation theory predicts that the wavefunction of the atom with respect to $|1\rangle$ and $|i\rangle$ is:

$$|\Psi\rangle = e^{-i\frac{E_1 t}{\hbar}}|1\rangle - \frac{\Omega_{1i}}{2(\omega_{1i}-\omega)}(1 - e^{i\frac{(E_i - E_1 - \hbar\omega)t}{\hbar}})e^{-i\frac{E_i t}{\hbar}}|i\rangle \tag{6.4}$$

where Ω_{1i} is the Rabi frequency of transitions between $|1\rangle$ and $|i\rangle$, and $\hbar\omega_{1i}$

is the energy of the transition between $|1\rangle$ and $|i\rangle$. The transition between $|i\rangle$ and $|2\rangle$ under illumination from light at frequency ω is described by a similar wavefunction $\Phi = c_i\,|i\rangle + c_2\,|2\rangle$, in which the rate of change of the amplitude c_2 is given by:

$$i\dot{c_2}(t) = \Omega_{i2}\cos(\omega t)e^{i\frac{(E_2-E_i)t}{\hbar}}c_i(t) \tag{6.5}$$

By taking the amplitude of the $|i\rangle$ term in Eq.(6.4) and substituting it for c_i in Eq.(6.5), a new expression for $\dot{c_2}$ is obtained. Upon integrating, and making use of the rotating-wave approximation for $E_2 - E_1 \simeq 2\hbar\omega$, the following expression for c_2 is obtained:

$$c_2(t) \simeq \frac{\hbar^2\Omega_{1i}\Omega_{i2}}{4(E_i - E_1 - \hbar\omega)(E_2 - E_1 - 2\hbar\omega)}(1 - e^{i\frac{(E_2-E_1-2\hbar\omega)t}{\hbar}}) \tag{6.6}$$

Reasoning from the similarity between this expression and the corresponding one for excitation with a single photon, this transition possesses an effective Rabi frequency given by:

$$\Omega_{eff} = \frac{\hbar\Omega_{1i}\Omega_{i2}}{2(E_i - E_1 - \hbar\omega)} \tag{6.7}$$

By further analogy with the equations for single-photon excitation, counterparts for various quantities associated with said excitation can be calculated for the two-photon transition. These include the components of the Bloch vectors, and from these, the absorption cross-section σ.

The form of the expressions for these quantities is nearly identical to those for the corresponding values related to the single-photon transition, and the quantities themselves can be written simply by replacing terms in the expressions for the single-photon transition with values corresponding to

the multiple-photon transition. For example, the absorption cross section σ for an atom illuminated by light at frequency ω, which excites a transition between two states $|1\rangle$ and $|2\rangle$, is given by:

$$\sigma = \frac{\Omega^2/4}{(\omega - \omega_0)^2 + \Gamma^2/4} \frac{A_{21}\hbar\omega}{I} \tag{6.8}$$

where Ω is the Rabi frequency of the transition, $\omega_0 \simeq \omega$ is the frequency of the transition, and A_{21} is the Einstein coefficient govening spontaneous emission between $|2\rangle$ and $|1\rangle$. If instead we have a transition between $|1\rangle$ and $|2\rangle$ where $\omega_0 \simeq 2\omega$, the corresponding expression for σ becomes:

$$\sigma = \frac{{\Omega_{eff}}^2/4}{(2\omega - \omega_0)^2 + \Gamma^2/4} \frac{2A_{21}\hbar\omega}{I} \tag{6.9}$$

$$= \frac{\pi^2 c^2}{\omega^2} A_{21} \widetilde{g}_H(2\omega - \omega_0) \tag{6.10}$$

where Ω_{eff} is given by Eq.(6.7) and $\widetilde{g}$ is the line shape function. The only changes to this expression are that Ω is replaced by Ω_{eff}, and the $\hbar\omega$ term representing the energy of each scattered photon is replaced by $2\hbar\omega$, representing the absorption of two photons in the transition, and the scattering of the sum of their energies in a single photon.

Substituting Eq.(6.7) into Eq.(6.10) gives an expression for σ:

$$\sigma = \frac{\pi^2 c^2}{\omega^2} A_{21} \frac{\hbar^3 \omega^3 {\Omega_{1i}}^2 {\Omega_{i2}}^2}{4\pi^2 c^2 (E_i - E_1 - \hbar\omega)^2 \left[(2\omega - \omega_0)^2 + \Gamma^2/4\right]} \tag{6.11}$$

We then recall from Eq.(4.8) that $\Omega_{ij} = eX_{ij}\mathcal{E}/\hbar$, and additionally, that

$$X_{ij} = \sqrt{\frac{A_{ij}\pi\epsilon_0\hbar c^3}{e^2\omega^3}} \tag{6.12}$$

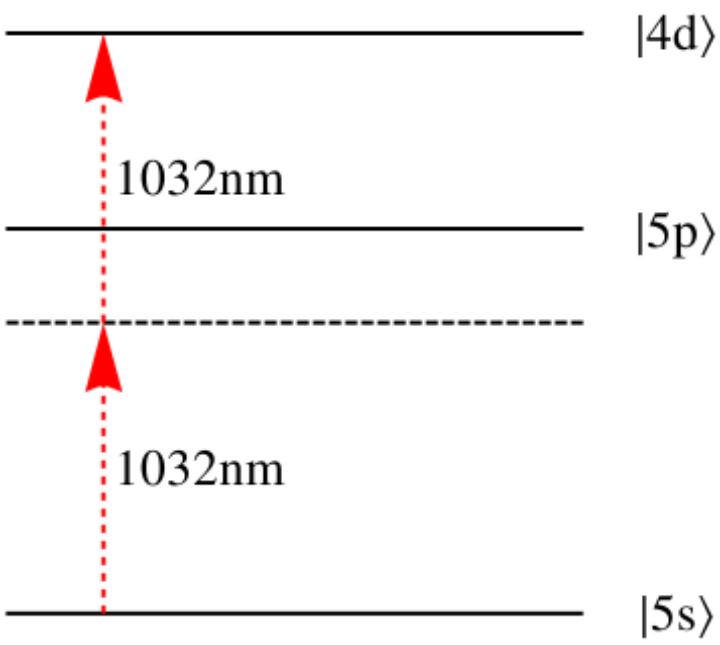

Fig. 6.1: Energy-level schematic for the two-photon transition between the 5s and 4d state of rubidium. Incoming photons at 1032nm excite electrons through the 5s to 4d transition by coupling both end states to the intermediate 5p state.

Substituting Eq.(6.12) into the expression for Ω_{ij}, and then substituting the resulting expression into Eq.(6.11) we obtain the following expression for $\widetilde{g}(2\omega - \omega_0)$:

$$\widetilde{g}(2\omega - \omega_0) = \frac{\hbar A_{2i} A_{i1} c^3 \epsilon_0 \mathcal{E}^2}{(2(E_i - E_1 - \hbar\omega)^2)\left[(2\omega - \omega_0)^2 + \Gamma^2/4\right]\omega^3} \tag{6.13}$$

where A_{2i} and A_{i1} are the Einstein coefficients for spontaneous decay between the excited state, the intermediate level and the ground state, Γ is the decay coefficient between the states $|2\rangle$ and $|1\rangle$, and $\mathcal{E}$ is the electric field amplitude of the incident light.

By substituting Eq.(6.10) into Eq.(4.7), the rate of fluorescence induced by the enhanced evanescent wave produced by light coupled into the waveguide at 1032 nm is calculated (Fig.(6.2a)). As in Chapter. 4, the enhance-

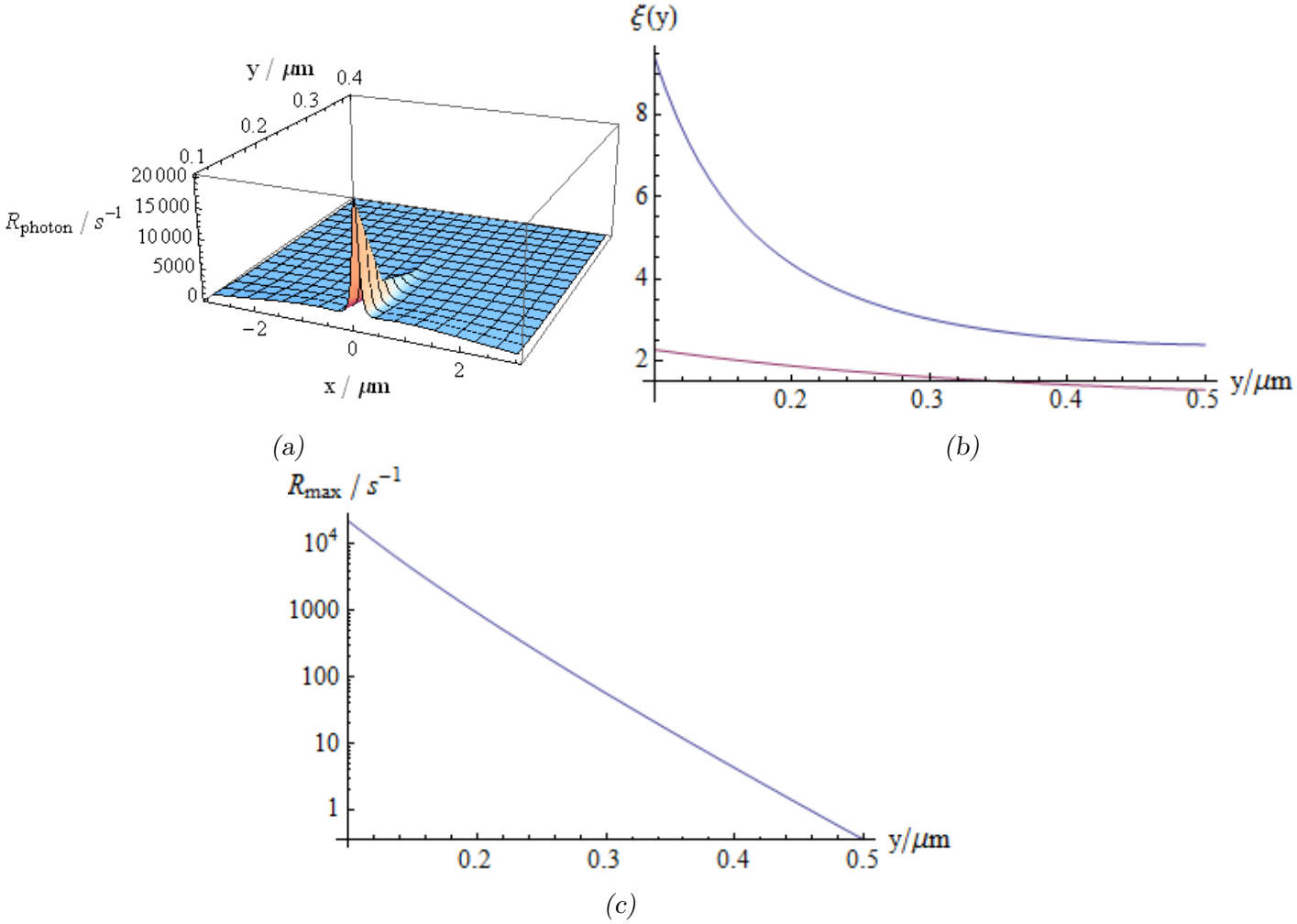

Fig. 6.2: a). 3-d plot of the fluorescence rate of 780 m due to the two-photon transition excited by the evanescent wave of 1032 nm light. Atoms are excited from the 5s to the 4d ground state via the absorption of two 1032 nm photons before decaying first to the 5p, then back to the ground state, emitting first a 1529 nm photon, and then a 780nm photon. b). Plot of $\xi(y)$, the contrast observed between the fluorescence of the atom directly above the wire and the fluorescence immediately outside the region affected by the wire; c). Logarithmic plot of fluorescence per atom over the centre of the wire in terms of photons scattered per second, against the distance of the atom from the waveguide surface.

ment factor of the fluorescence due to the metal wire is calculated and plotted, using parameters obtained by fitting the numerical data to Eq.(4.3). Finally, we plot logarithmically the peak fluorescence rates above the centre of the guide. For the purposes of comparison, the values of ξ obtained for the direct 780 nm transition in Sec. (4.4) are plotted along the same axes in Fig.(6.2b).

From Fig(6.2b), it can be seen that the fluorescence of the atom between the 4d and 5s states is considerably enhanced by the presence of the wire, by approximately 9.5 times at 0.1 μm from the waveguide surface, declining exponentially to approximately 2.4 times at 0.5 μm from the surface. By comparison with the line taken from Fig.(4.5b), it is seen that, as predicted, the effect of the metal wire is stronger with regard to the two-photon transition than it is for the direct transition between the 5s and 5p state.

While the presence of the metal wire allows the fluorescence of the atom due to the stimulated Raman passage between the 5s and 4d states to be strongly enhanced, the actual response of the transition to incident light is far less strong than in the case of a direct transition. From Eq(6.13), the absorption cross-section σ of the two-photon transition varies as the inverse of the detuning between the incident light and the energy level difference between the ground state and the intermediate level, which in the case of the 5s to 4d transition in rubidium is the detuning between light at 1032 nm and at 780 nm. To achieve the fluorescence rates recorded in Fig.(6.2a) and Fig.(6.2c), it was necessary to normalize the power through the waveguide at 10 mW, several orders of magnitude larger than the 1 μW which was used in Chapter. 4. Even having coupled such power through the waveguide and into the metal wire, the rates of fluorescence achieved over the wire remains considerably smaller than those recorded in Fig.(4.5). Furthermore, the rate of fluorescence over the wire decays even faster as the height of the atoms above the waveguide surface increases–from Fig.(6.2c), the rate at which

photons are emitted over the wire declines to less that one per second at approximately 0.46 μm above the surface.

To all appearances, while the presence of the wire does enhance the fluorescence of the stimulated Raman passage between the 5s and 4d state, the actual rate at which photons are scattered by the incident light remains small. This rate, however, responds more strongly to changes in the electric field amplitude of incident light, behaving quadratically rather than linearly as in the case of the direct 5s-5p transition. For the purposes of allowing such a device to become feasible, further optimisation of the coupling from the waveguide into the wire, in order to increase the strength of the enhanced evanescent field, is expected to yield twin benefits in the form of increased scattering over the wire, as well as a stronger contrast between the enhanced and unenhanced regions of the evanescent wave.

6.2.3 Conclusion

The high intensities of the evanescent field obtained by coupling light from the mode of a dielectric waveguide to the surface plasmon of a metal structure emplaced on top of a waveguide raise the possibility that low-noise fluorescent imaging of trapped atoms may be performed by exciting multiple-photon transitions that then decay, releasing high-energy photons that can be easily separated from the much less energetic incident photons. As the intensities of the light increase, higher-order transitions become available, and thus the separation between the incident and emitted photons increases.

The rate of fluorescence due to the two-photon transition between the 5s and 4d states of rubidium was found to be strongly enhanced over the wire. However, to achieve significant rates of fluorescence, it was necessary to increase the power coupled through the waveguide by a factor of 10^4 over the value used in Sec. (4.4). Furthermore, the fluorescence decays rapidly

with distance above the surface of the waveguide.

Using two photons to induce transitions between the 5s and 4d state, fluorescence rates on the order of several thousands of photons per second can be observed, albeit only within a short distance of the wire. This transition may therefore be impractical when attempting to detect atoms confined much further from the waveguide. Where the atoms are confined much closer to the waveguide surface, such as in the case of the dipole potential discussed in Chapter 5, the two-photon transition is capable of inducing fluorescence with sufficient frequency that atoms may be detected over the wire. It is noted, in fact, that the wavelength of the incident light exciting the two-photon transition is very close to that of the red-detuned light used in Chapter 5. The possibility then suggests itself that the same wavelength may be used in an evanescent-wave dipole trap not only to provide an attractive potential in the direction of the waveguide surface, but also to excite two-photon transitions for fluorescent imaging, allowing atoms in this potential to be easily imaged.

6.3 Tight dipole trapping and the Tonks-Girardeau gas

6.3.1 Introduction

As discussed in Chapter. 5, very tight 1-dimensional potential wells, running above and parallel to the centerline of the waveguide, can be generated using the enhanced evanescent fields of modes of two different frequencies of light coupled down the same waveguide. Within these tight trapping potentials, only one transverse energy level is available to be occupied by trapped atoms. Atoms trapped in this potential therefore fulfil the condition necessary for the creation of a 1-dimensional gas–namely, that transverse energy levels higher than the ground state remain inaccessible to trapped atoms. One unique state of matter which has been investigated in recent years is the Tonks-

Girardeau gas [39,40], consisting of a collection of bosonic atoms, held in the ground state of a 1-dimensional trapping potential with comparable trapping frequencies to the potential well investigated in Chapter. 5.

One consequence of this tight confinement of atoms in the Tonks-Girardeau gas is that atoms are unable to pass each other along the length of the 1-dimensional potential. The gas therefore takes the form of a truly one-dimensional line of atoms along the centre of the trapping potential. More importantly, the bosonic atoms that make up the Tonks-Girardeau gas exhibit quasi-fermionic behaviour–while multiple atoms in the gas are able to occupy the same momentum state, a kind of "exclusion principle" is in effect, the interaction between atoms preventing those atoms from occupying the same location within the gas.

6.3.2 The wavefunction of a Tonks-Girardeau gas

A Tonks-Girardeau gas is a collection of bosonic atoms described by the solution of the 1-dimensional, many-body Schrodinger equation,

$$-\sum_{j=1}^{n} \frac{\hbar^2}{2m} \frac{\partial^2 \psi}{\partial {x_j}^2} + V\psi = E\psi \tag{6.14}$$

where ψ is the wavefunction of the system, a is the size of the impenetrable core of each atom, and x_1 to x_n are the spatial coordinates of the n particles making up the system. The impenetrability of the atoms is expressed by specifying the following condition for the solution:

$$\psi(x_1, x_2, \ldots, x_n | x_j = x_l) = 0, 1 \leq l < j \leq n \tag{6.15}$$

If one ignores the fact that the gas is made up of bosonic atoms, the wavefunction of a free fermionic gas is a solution of the above equation that obeys the condition given by (6.15). This wavefunction is given for a gas of

N atoms by the well-known Slater determinant of the first N single-particle solutions of the Schrodinger equation in a potential V:

$$\psi_f(x_1, x_2, \ldots, x_N) = \frac{1}{\sqrt{N!}} \begin{vmatrix} \psi_1(x_1) & \psi_2(x_1) & \ldots & \psi_N(x_1) \\ \vdots & & & \vdots \\ \psi_1(x_N) & \psi_2(x_N) & \ldots & \psi_N(x_N) \end{vmatrix} \tag{6.16}$$

By defining an anti-symmetric function,

$$A(x_1, x_2, \ldots, x_N) = \prod_{j>l} \frac{x_j - x_l}{|x_j - x_l|} \tag{6.17}$$

this anti-symmetric fermionic wavefunction can be transformed to a symmetric solution of equation (6.14) that obeys (6.15), with similar eigenvalues to those of the Fermi wavefunction [38].

$$\psi_b = A\psi_f = |\psi_f| \tag{6.18}$$

6.3.3 Momentum distribution functions of a Tonks-Girardeau gas

While the spatial distribution of a Tonks-Girardeau gas resembles that of a gas of free fermions, the momentum distribution of the same gas does not resemble the classical distribution of a Fermi gas. Rather, the momentum distribution is strongly peaked around zero. The momentum distribution, $n(k)$, is obtained from the Fourier transformation of the density matrix $\rho(x, x')$ [66]:

$$n(k) = \int_{-\infty}^{\infty} dx \int_{-\infty}^{\infty} dx' \rho(x, x') e^{-ik(x-x')} \tag{6.19}$$

where $\rho(x, x')$ is given by:

$$\rho(x,x') = N \int \psi_B i(x, x_2, x_3, \ldots, x_N)\psi_B(x', x_2, x_3, \ldots, x_N)dx_2 dx_3 \ldots dx_N \tag{6.20}$$

An analytic expression for this integral in the thermodynamic limit ($N \to \infty, L \to \infty$) was obtained by Vaidya and Tracy [66], which when substituted into the momentum distribution equation yielded a distribution strongly-peaked about the origin.

6.3.4 Tonks-Girardeau gases in real traps–the Lieb-Liniger parameter

The interaction that governs collisions between impenetrable atoms at low energies is given by the Huang pseudopotential [67]:

$$U(r) = g\delta(r)(\frac{\partial}{\partial r}r\psi) \tag{6.21}$$

with ψ being the collective wavefunction of the colliding atoms. The scattering amplitudes of atoms interacting with this pseudopotential were examined by Olshanii [16], for a gas of atoms at low energies within an elongated, narrow harmonic potential. The energy of the atoms was limited by the gap between the ground and first excited states of the transverse wavefunction, confining them to the transverse ground state. As the atomic energies approach zero, the variations of the scattering amplitudes converge with those arising from a δ-function interaction:

$$U(r) = g\delta(r) \tag{6.22}$$

Analysis of a one-dimensional gas with δ-function interactions was carried out by Lieb and Liniger [68]. For a gas of atoms within a 1-dimensional potential V, the Hamiltonian is:

$$H = -\frac{\hbar^2}{2m}\sum_{i=1}^{N}\frac{\partial^2\psi}{\partial x_i^2} + (V + g_1\sum_{i<j}\delta(x_j - x_i)) \tag{6.23}$$

From their examination of the solutions for this Hamiltonian, Lieb and Liniger isolated a single parameter governing the behaviour of the gas: $\gamma = g_1/\rho_{1D}$, where g_1 is the coupling paramter between atoms in the 1-dimensional gas, and ρ_{1D} is the 1-dimensional density of atoms along the length of the trap. For $\gamma = \infty$, the solution is that of the Tonks-Girardeau gas. One consequence of this result is that the behaviour of the gas moves closer to the Tonks-Girardeau solution as the 1-dimensional density of the gas decreases. Further work by Lieb and Seiringer defined a spectrum of behaviours as the value of γ increased from zero to infinity [69], transiting from the ideal gas state through the Gross-Pitaevskii and Thomas-Fermi regimes before arriving in the Tonks-Girardeau state.

Thus, the conditions necessary to obtain a Tonks-Girardeau gas from a gas of neutral atoms within a harmonic potential become known–firstly, that the energy of the gas is sufficiently low to prohibit excitation into higher transverse energy states, and secondly that the interatomic coupling constant is sufficiently high, and the density of the gas is sufficiently low, that the ratio of these two quantities approaches infinity.

6.3.5 Tuning the Lieb-Liniger parameter–coupling constants and atom trap parameters

For a gas of atoms within an elongated harmonic potential, the 1-dimensional interatomic coupling constant, g_1, is given by [16]:

$$g_1 = -\frac{2\hbar^2}{ma_1} \tag{6.24}$$

where a_1 is the 1-dimensional scattering length of collisions between the

atoms. a_1 is in turn given by:

$$a_1 = -\frac{a_\perp^2}{2a}(1 - C\frac{a}{a_\perp}) \tag{6.25}$$

where a is the free-space scattering length between two atoms, $C = 1.46$ (from [16]), $a_\perp = \sqrt{2\hbar/m\omega_\perp}$ is the size of the transverse ground state of the potential, and $\omega_\perp$ is the frequency of oscillation of the transverse ground state. As $\omega_\perp$ increases, $a_\perp$ goes to zero, and g_1 goes to infinity. The Lieb-Liniger parameter, γ, may therefore be tuned either by changing the transverse tightness of the 1-dimensional confinement, or simply by adjusting the number of atoms in the trap. At low γ, the kinetic term in Eq. (6.23) dominates over the interaction between the atoms, and the atoms exist in a quasi-condensate state, macroscopically occupying the lowest energy levels of the confining potential. As γ increases, the interaction term g_1 begins to dominate over the kinetic energy of the atoms. At higher values of γ, the atoms are no longer able to interpenetrate with each other, and the motion of atoms along the axis of the 1-dimensional potential is frozen out by the inter-atomic repulsions.

It must be noted that previous discussion has pointed out that the potential experienced by atoms inside the dipole potential well is not truly harmonic. In Eq.(6.25), $a_\perp$ is defined as the width of a harmonic potential well at the ground state energy defined by $\hbar\omega_\perp$. As in Sec.(5.4), to properly calculate $a_\perp$, it is first necessary to numerically solve Schrodinger's equation for the ground state energy. The resulting value may then be plugged into Eq.(5.9), which may then in turn be solved for the size of the potential well associated with that ground state energy. As also noted in Sec.(5.4), this method of finding the ground state energy associated with a given potential well is more computationally complex than simply making use of a harmonic

approximation to estimate said energy. In the interests of simplifying our calculation, therefore, we again make use of the harmonic approximation for our potential well in the calculations that follow.

It must also be noted that the expression given by Eq.(6.25) was derived for the case of a 1-dimensional atom gas trapped in an infinite harmonic potential [16]. More specifically, part of this derivation involves an expansion of the transverse wavefunctions of trapped atoms as a series over the eigenstates of the harmonic potential. It is obvious that any real potential well must deviate in some way from this simplified model. However, to generalise the method used in [16] for a real, possibly anharmonic potential well is however not an easy task. Hence, for the sake of simplicity, we have simply used the expression given in Eq.(6.25).

As a final aside, we must also note that, as the depth of a potential well is increased, so does the accuracy with which the lowest energy states within the well may be estimated by the harmonic approximation. If we recall from Eq.(5.5) that the depth of the dipole potential well is directly proportional to the power coupled into the wire, it is therefore possible to maximise the validity of the harmonic approximation, and thus the validity of predictions made using Eq.(6.25), simply by increasing the power coupled into the wire from both modes, thereby creating a deeper, tighter trap.

6.3.6 1-dimensional gases in the dipole potential

From previous subsections, the parameters of a trapping potential required to create a Tonks-Girardeau gas are known–first that the density of the atoms within the trap is very small, and that the transverse trapping frequencies of the trap are very large. From Chapter. 5, very high trapping frequencies have been shown to be feasible using the dipole trap created from enhanced evanescent waves over a waveguide. With such a trap, therefore, it in turn

becomes feasible to prepare a Tonks-Girardeau gas.

A more rigorous criterion for the formation of a Tonks-Girardeau gas is given by [16]:

$$k_z \left| a_1 \right| \ll 1 \tag{6.26}$$

where $\hbar k_z$ is the axial momentum of atoms within the gas. For a box of length L, with periodic boundary conditions, the wave number k_z is bounded by the limit:

$$|k_z| < \frac{\pi(N-1)}{L} \tag{6.27}$$

where N is the average number of atoms within the length L.

Some comparison can be made to results obtained by [40] and [39] using the parameters calculated in Chapter. 5. From both [40] and [39], atom gases are found in the Tonks-Girardeau state at $\gamma = 5.5$, where $\gamma = -\pi/k_z a_1$.

From the transverse trapping frequencies obtained in Chapter. 5, the maximum linear density of atoms along the long axis of the trap required to produce $\gamma \geq 5.5$ is calculated and plotted in Fig.(6.3), over the same range of values as Fig.(5.3).

By comparison, the atom density of approximately 77 atoms per hundred microns was reported by [39]. It is therefore possible, using the evanescent wave dipole trap, to produce a 1-dimensional potential well capable of confining a gas of neutral atoms in the Tonks-Girardeau regime, with similar or higher γ, and with similar or higher atom densities than those achieved in [39]. These densities are furthermore considerably higher than those achieved in [40], in which high γ was achieved for very low densities[1] through the use of a red-detuned standing-wave dipole potential along the

[1] On the order of 20 atoms over a total length of 160 μm.

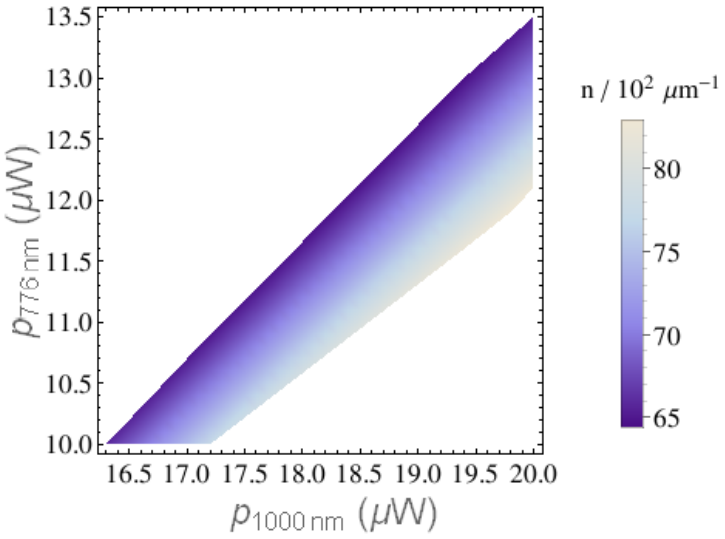

Fig. 6.3: Density plot of the maximum atom density required to achieve $\gamma = 5.5$ over p_{1000nm} and p_{776nm}, the total powers coupled into the waveguide from the 1000 nm and 776 nm modes respectively.

long axis of the potential well.

The dual-wavelength dipole trap above the metal wire produces an isolated trapping potential, as opposed to the large array of 1-dimensional wells produced by the intersecting optical lattices in [40] and [39]. In addition to this, the close proximity of the trap bottom to the metal wire further allows the imaging of atoms within the trap using the fluorescent methods discussed in Chapter. 4, as well as in Sec.6.2.2.

Integration of the dual-wavelength dipole trap with atom chip structures placed directly under the waveguide allows us to add an axial confinement to the 1-dimensional trapping potential. This in turn allows us to control the 1-dimensional atom density ρ_{1D}, and through this, the Lieb-Liniger parameter γ, by manipulating the length L of the confining potential. In the concluding chapter of this thesis, we propose a simple device incorporating both atom-chip and optical components for the purpose of manipulating a 1-dimensional atom cloud in this manner.

6.4 Conclusion

To summarise this chapter, we have investigated the fluorescence of atoms above the metal wire due to the excitation of two-photon transitions by the enhanced evanescent wave. Here, we consider excitations due to a two-photon absorption process between the 5s and 4d states of rubidium. Using the two-photon process, fluorescence rates on the order of thousands of photons per second were observed close to the waveguide surface, but were found to decay very rapidly with increasing height over the waveguide surface.

Additionally, the characteristics of a gas of atoms confined in the 1-dimensional trapping potential discussed in Chapter 5 were examined. Scattering lengths and interaction parameters between atoms inside this potential were calculated. These values were then used to derive values of the maximum atom density necessary to match parameters taken from [40] and [39], focusing particularly on the parameter γ used to characterise the state of a 1-dimensional atom gas. At $\gamma = 5.5$, the maximum density of the atom cloud is found to be larger than the values reported by [40] and [39] for similar γ.

7. CONCLUSION AND OUTLOOK FOR FUTURE WORK

7.1 Overview of previous work and conclusions

In this thesis, we have studied the use of metal wires emplaced over square waveguides to enhance the evanescent waves of light passing through the guides. We have then assessed the use of these enhanced evanescent waves to detect atoms held closely over the waveguide surface. In particular, we have calculated the effects of the enhanced evanescent wave on the fluorescence rates of rubidium atoms scattering 780 nm light. In addition to this, we have also investigated the absorption of two photons of 1032 nm light between the 5s and 4d states of rubidium, and the subsequent re-emission of a 1529 nm photon and a 780nm photon, as a means of eliminating noise from fluorescent detection of trapped atoms.

We have also considered the use of dipole potentials created by superposing evanescent waves of oppositely-detuned waveguide modes to create potential wells capable of tightly confining atoms in the transverse direction. The characteristics of these wells, and the way in whicch they may be manipulated by changing the relative input powers of the oppositely-detuned waveguide modes have been studied. Changes in the characteristics of the dipole potential wells as the wavelengths of the input modes are altered have also been calculated and analysed. Finally, by studying the interactions between individual atoms trapped within the dipole potential well, and the way in which these interactions change with atom density, it is found possi-

ble to make use of the dipole potential well to trap atoms in an impenetrable 1-dimensional state which has only previously been achieved using optical lattice techniques.

The analyses carried out in this thesis were performed for the purpose of evaluating the feasibility of using plasmonic structures in atom physics experiments. In following sections, we suggest several possible avenues of investigation following the research carried out in this thesis.

7.2 Manipulation of 1-dimensional gases over an atom chip

Let us consider a square waveguide over which a thin metal wire is emplaced, and into which is coupled two oppositely-detuned modes of light. The enhanced evanescent waves over the thin wire create the tightly-confining, 1-dimensional potential well discussed here as well as in Chap. 5. Let this waveguide then be emplaced over the surface of an atom chip. An array of parallel straight wires located a distance δL from each other is also emplaced on the atom chip surface, below and running perpendicular to the waveguide. Atoms trapped in the 1-dimensional potential well can then be confined magnetically along the long axis of the potential by passing current through any two selected wires within this array. By selecting an appropriate value for L, the resulting potential well may possess trapping frequencies on the order of hundreds of kilohertz in the transverse direction, but only on the order of a few hertz in the longitudinal direction.

The 1-dimensional atom density ρ_{1D} may also be manipulated using this device. Let us consider a 1-dimensional gas confined axially inside the evanescent-wave trap by magnetic fields of currents passing through two wires a distance $n\delta L$ apart. The size of the axial confinement may then be increased by ramping down the current in one of the wires, and ramping up current in

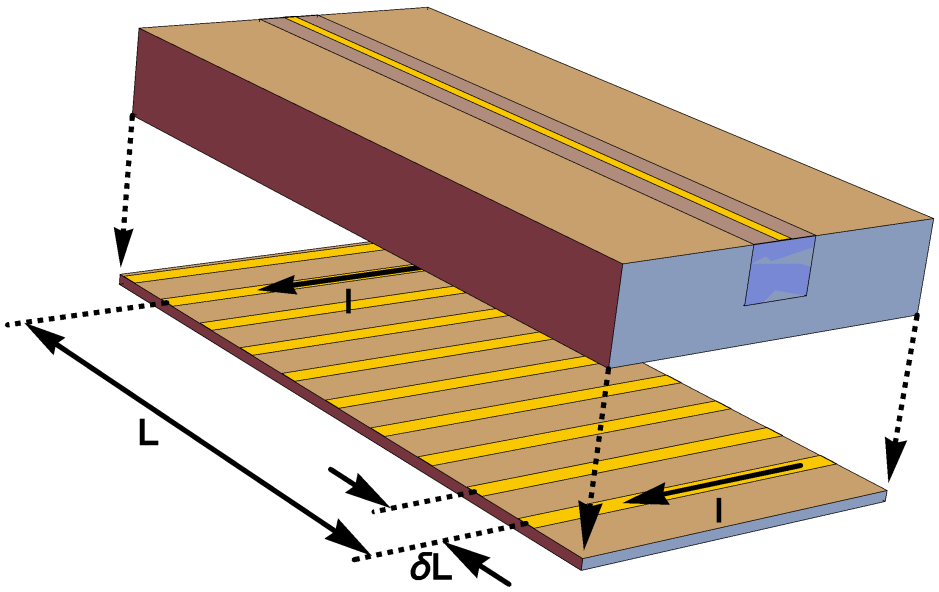

Fig. 7.1: Diagram of device proposed in Sec.(7.2), consisting of an array of metal wires emplaced on an atom chip surface below a waveguide, over which is also emplaced a thin metal wire. Atoms are confined over the plasmonic wire by the evanescent wave dipole trap described in Chapter 5. A current I is passes through two wires in the array located a distance L away from each other. Atoms within the evanescent wave trap are then confined along the direction of the waveguide by the magnetic potentials created by this current.

another such that the distance between the two current-carrying wires is now $(n+1)\delta L$. By adjusting the length of the confinement in this manner, we therefore are able to also adjust the 1-dimensional atom density ρ_{1D}, and by adjusting ρ_{1D}, are able to manipulate the parameter γ describing the state of the 1-dimensional gas.

Additionally, it is also possible to use this arrangement to shift 1-dimensional atom clouds up and down the length of the waveguide. To do this, one may simply ramp down the current flowing through the two wires providing the confining magnetic potential, while at the same time ramping up the two

wires adjacent to the originals in the desired direction of motion. Similar to the magnetic conveyor belt experiments performed by Reichel *et. al.* [9–11], this may allow 1-dimensional gases to be first created over one region of the chip, then moved over to a different section of the chip containing equipment for carrying out experiments on the gas.

7.3 Shaping potentials via machining of the plasmonic wire

By interrupting or corrugating the wire along the waveguide, one may in turn shape the evanescent-wave potential well in various ways. One may use such a break in the wire, for example to set up a potential barrier between one portion of the waveguide and another. This barrier may in turn form a tunnelling junction between waveguide sections, which may then be used to investigate tunnelling behaviour of atoms in 1-dimensional gases.

More complex effects may be achieved by making use of periodic interruptions of the wire. This in turn results in a periodic series of potential wells. Possible applications of interest for such structures include investigation of atom tunnelling through multiple potential barriers and bunching of atoms into 1-dimensional potential wells of arbitrary lengths.

The narrow widths of the structures studied in this thesis enable us to emplace multiple wires side by side on top of the waveguide. This in turn allows us to study atoms trapped in two-dimensional lattices over the waveguide surface.

7.4 Single atom trapping using surface plasmons focused to a point

In the case of a plasmonic structure in the shape of a long isoceles triangle, surface plasmons travelling up from the base of the triangle are focused by the sides of the triangle into the apex. The concentration of plasmons within the tip produces a strong evanescent field in the region directly above the apex [70,71]. A similar focusing effect may be achieved by placing a triangular structure over our waveguide. By coupling oppositely-detuned states of light down the same guide, a tightly-confining, near-spherical potential well may be created, in a manner similar to the 1-dimensional potential well produced by the wire over the waveguide. Using this potential, a single-atom trap similar to the plasmonic fibre-tip trap propsed by Chang *et. al.* [72] may be implemented.

It may be possible to use this device, in conjunction with the method described in Sec.(7.2), to separate a single atom from the 1-d gas. One possible configuration would be to have the metal wire emerge from the apex of the triangle. A 1-dimensional atom gas may be moved magnetically up the wire until the first atom falls into the spherical potential well above the triangle apex. The gas is then moved magnetically away from the triangle, leaving the single atom isolated.

BIBLIOGRAPHY

[1] J. Fortágh and C. Zimmermann, "Magnetic microtraps for ultracold atoms," *Reviews of Modern Physics*, vol. 79, no. 1, pp. 235–289, Feb. 2007. [Online]. Available: http://link.aps.org/doi/10.1103/RevModPhys.79.235

[2] H. Ott, J. Fortágh, G. Schlotterbeck, A. Grossmann, and C. Zimmermann, "Bose-Einstein condensation in a surface microtrap," *Physical Review Letters*, vol. 87, no. 23, p. 230401, Nov. 2001. [Online]. Available: http://link.aps.org/doi/10.1103/PhysRevLett.87.230401

[3] W. Hänsel, P. Hommelhoff, T. W. Hänsch, and J. Reichel, "Bose-Einstein condensation on a microelectronic chip," *Nature*, vol. 413, no. 6855, pp. 498–501, Oct. 2001. [Online]. Available: http://www.nature.com/nature/journal/v413/n6855/full/413498a0.html

[4] A. E. Leanhardt, A. P. Chikkatur, D. Kielpinski, Y. Shin, T. L. Gustavson, W. Ketterle, and D. E. Pritchard, "Propagation of Bose-Einstein condensates in a magnetic waveguide," *Physical Review Letters*, vol. 89, no. 4, p. 040401, Jul. 2002. [Online]. Available: http://link.aps.org/doi/10.1103/PhysRevLett.89.040401

[5] D. Cassettari, A. Chenet, R. Folman, A. Haase, B. Hessmo, P. Krüger, T. Maier, S. Schneider, T. Calarco, and J. Schmiedmayer, "Micromanipulation of neutral atoms with nanofabricated structures,"

Applied Physics B, vol. 70, no. 5, pp. 721–730, Apr. 2000. [Online]. Available: http://link.springer.com/article/10.1007/s003400050886

[6] N. H. Dekker, C. S. Lee, V. Lorent, J. H. Thywissen, S. P. Smith, M. Drndi, R. M. Westervelt, and M. Prentiss, "Guiding neutral atoms on a chip," *Physical Review Letters*, vol. 84, no. 6, pp. 1124–1127, Feb. 2000. [Online]. Available: http://link.aps.org/doi/10.1103/PhysRevLett.84.1124

[7] D. Cassettari, B. Hessmo, R. Folman, T. Maier, and J. Schmiedmayer, "Beam splitter for guided atoms," *Physical Review Letters*, vol. 85, no. 26, pp. 5483–5487, Dec. 2000. [Online]. Available: http://link.aps.org/doi/10.1103/PhysRevLett.85.5483

[8] D. Müller, E. A. Cornell, M. Prevedelli, P. D. D. Schwindt, Y.-J. Wang, and D. Z. Anderson, "Magnetic switch for integrated atom optics," *Physical Review A*, vol. 63, no. 4, p. 041602, Mar. 2001. [Online]. Available: http://link.aps.org/doi/10.1103/PhysRevA.63.041602

[9] J. Reichel, W. Hänsel, and T. W. Hänsch, "Atomic micromanipulation with magnetic surface traps," *Physical Review Letters*, vol. 83, no. 17, pp. 3398–3401, Oct. 1999. [Online]. Available: http://link.aps.org/doi/10.1103/PhysRevLett.83.3398

[10] W. Hänsel, J. Reichel, P. Hommelhoff, and T. W. Hänsch, "Magnetic conveyor belt for transporting and merging trapped atom clouds," *Physical Review Letters*, vol. 86, no. 4, pp. 608–611, Jan. 2001. [Online]. Available: http://link.aps.org/doi/10.1103/PhysRevLett.86.608

[11] P. Hommelhoff, W. Hänsel, T. Steinmetz, T. W. Hänsch, and J. Reichel, "Transporting, splitting and merging of atomic ensembles in a chip

trap," *New Journal of Physics*, vol. 7, no. 1, p. 3, Jan. 2005. [Online]. Available: http://iopscience.iop.org/1367-2630/7/1/003

[12] Y.-J. Wang, D. Z. Anderson, V. M. Bright, E. A. Cornell, Q. Diot, T. Kishimoto, M. Prentiss, R. A. Saravanan, S. R. Segal, and S. Wu, "Atom michelson interferometer on a chip using a bose-einstein condensate," *Physical Review Letters*, vol. 94, no. 9, p. 090405, Mar. 2005. [Online]. Available: http://link.aps.org/doi/10.1103/PhysRevLett.94.090405

[13] Y. Shin, C. Sanner, G.-B. Jo, T. A. Pasquini, M. Saba, W. Ketterle, D. E. Pritchard, M. Vengalattore, and M. Prentiss, "Interference of Bose-Einstein condensates split with an atom chip," *Physical Review A*, vol. 72, no. 2, p. 021604, Aug. 2005. [Online]. Available: http://link.aps.org/doi/10.1103/PhysRevA.72.021604

[14] T. Schumm, S. Hofferberth, L. M. Andersson, S. Wildermuth, S. Groth, I. Bar-Joseph, J. Schmiedmayer, and P. Krüger, "Matter-wave interferometry in a double well on an atom chip," *Nature Physics*, vol. 1, no. 1, pp. 57–62, Sep. 2005. [Online]. Available: http://www.nature.com/nphys/journal/v1/n1/full/nphys125.html

[15] A. Günther, S. Kraft, M. Kemmler, D. Koelle, R. Kleiner, C. Zimmermann, and J. Fortágh, "Diffraction of a Bose-Einstein condensate from a magnetic lattice on a microchip," *Physical Review Letters*, vol. 95, no. 17, p. 170405, Oct. 2005. [Online]. Available: http://link.aps.org/doi/10.1103/PhysRevLett.95.170405

[16] M. Olshanii, "Atomic scattering in the presence of an external confinement and a gas of impenetrable bosons," *Physical Review*

Letters, vol. 81, no. 5, pp. 938–941, Aug. 1998. [Online]. Available: http://link.aps.org/doi/10.1103/PhysRevLett.81.938

[17] J. Estève, J.-B. Trebbia, T. Schumm, A. Aspect, C. I. Westbrook, and I. Bouchoule, "Observations of Density Fluctuations in an Elongated Bose Gas: Ideal Gas and Quasicondensate Regimes," *Physical Review Letters*, vol. 96, no. 13, p. 130403, Apr. 2006. [Online]. Available: http://link.aps.org/doi/10.1103/PhysRevLett.96.130403

[18] T. Jacqmin, J. Armijo, T. Berrada, K. V. Kheruntsyan, and I. Bouchoule, "Sub-Poissonian fluctuations in a 1d Bose gas: From the quantum quasicondensate to the strongly interacting regime," *Physical Review Letters*, vol. 106, no. 23, p. 230405, Jun. 2011. [Online]. Available: http://link.aps.org/doi/10.1103/PhysRevLett.106.230405

[19] J. Reichel and J. Thywissen, "Using magnetic chip traps to study Tonks-Girardeau quantum gases," *Journal de Physique IV (Proceedings)*, vol. 116, p. 10, 2004.

[20] J. Fortágh, H. Ott, S. Kraft, A. Günther, and C. Zimmermann, "Surface effects in magnetic microtraps," *Physical Review A*, vol. 66, no. 4, p. 041604, Oct. 2002. [Online]. Available: http://link.aps.org/doi/10.1103/PhysRevA.66.041604

[21] A. E. Leanhardt, Y. Shin, A. P. Chikkatur, D. Kielpinski, W. Ketterle, and D. E. Pritchard, "Bose-Einstein condensates near a microfabricated surface," *Physical Review Letters*, vol. 90, no. 10, p. 100404, Mar. 2003. [Online]. Available: http://link.aps.org/doi/10.1103/PhysRevLett.90.100404

[22] J. Estève, C. Aussibal, T. Schumm, C. Figl, D. Mailly, I. Bouchoule, C. I. Westbrook, and A. Aspect, "Role of wire imperfections in

micromagnetic traps for atoms," *Physical Review A*, vol. 70, no. 4, p. 043629, Oct. 2004. [Online]. Available: http://link.aps.org/doi/10.1103/PhysRevA.70.043629

[23] J.-B. Trebbia, C. L. Garrido Alzar, R. Cornelussen, C. I. Westbrook, and I. Bouchoule, "Roughness suppression via rapid current modulation on an atom chip," *Physical Review Letters*, vol. 98, no. 26, p. 263201, Jun. 2007. [Online]. Available: http://link.aps.org/doi/10.1103/PhysRevLett.98.263201

[24] S. Groth, P. Krüger, S. Wildermuth, R. Folman, T. Fernholz, J. Schmiedmayer, D. Mahalu, and I. Bar-Joseph, "Atom chips: Fabrication and thermal properties," *Applied Physics Letters*, vol. 85, no. 14, pp. 2980–2982, Oct. 2004. [Online]. Available: http://scitation.aip.org/content/aip/journal/apl/85/14/10.1063/1.1804601

[25] P. Krüger, L. M. Andersson, S. Wildermuth, S. Hofferberth, E. Haller, S. Aigner, S. Groth, I. Bar-Joseph, and J. Schmiedmayer, "Potential roughness near lithographically fabricated atom chips," *Physical Review A*, vol. 76, no. 6, p. 063621, Dec. 2007. [Online]. Available: http://link.aps.org/doi/10.1103/PhysRevA.76.063621

[26] D. A. Smith, S. Aigner, S. Hofferberth, M. Gring, M. Andersson, S. Wildermuth, P. Krüger, S. Schneider, T. Schumm, and J. Schmiedmayer, "Absorption imaging of ultracold atoms on atom chips," *Optics Express*, vol. 19, no. 9, pp. 8471–8485, Apr. 2011. [Online]. Available: http://www.opticsexpress.org/abstract.cfm?URI=oe-19-9-8471

[27] W. S. Bakr, J. I. Gillen, A. Peng, S. Fölling, and M. Greiner, "A quantum gas microscope for detecting single atoms in a Hubbard-

regime optical lattice," *Nature*, vol. 462, no. 7269, pp. 74–77, Nov. 2009. [Online]. Available: http://www.nature.com/nature/journal/v462/n7269/abs/nature08482.html

[28] M. Wilzbach, A. Haase, M. Schwarz, D. Heine, K. Wicker, X. Liu, K.-H. Brenner, S. Groth, T. Fernholz, B. Hessmo, and J. Schmiedmayer, "Detecting neutral atoms on an atom chip," *Fortschritte der Physik*, vol. 54, no. 8-10, p. 746764, Aug. 2006. [Online]. Available: http://onlinelibrary.wiley.com/doi/10.1002/prop.200610323/abstract

[29] D. Heine, M. Wilzbach, T. Raub, B. Hessmo, and J. Schmiedmayer, "Integrated atom detector: Single atoms and photon statistics," *Physical Review A*, vol. 79, no. 2, p. 021804, Feb. 2009. [Online]. Available: http://link.aps.org/doi/10.1103/PhysRevA.79.021804

[30] M. Wilzbach, D. Heine, S. Groth, X. Liu, T. Raub, B. Hessmo, and J. Schmiedmayer, "Simple integrated single-atom detector," *Optics Letters*, vol. 34, no. 3, pp. 259–261, Feb. 2009. [Online]. Available: http://ol.osa.org/abstract.cfm?URI=ol-34-3-259

[31] D. Heine, W. Rohringer, D. Fischer, M. Wilzbach, T. Raub, S. Loziczky, X. Liu, S. Groth, B. Hessmo, and J. Schmiedmayer, "A single-atom detector integrated on an atom chip: fabrication, characterization and application," *New Journal of Physics*, vol. 12, no. 9, p. 095005, Sep. 2010. [Online]. Available: http://iopscience.iop.org.libproxy1.nus.edu.sg/1367-2630/12/9/095005

[32] P. Quinto-Su, M. Tscherneck, M. Holmes, and N. Bigelow, "On-chip optical detection of laser cooled atoms," *Optics Express*, vol. 12, no. 21, pp. 5098–5103, Oct. 2004. [Online]. Available: http://www.opticsexpress.org/abstract.cfm?URI=oe-12-21-5098

[33] S. Eriksson, M. Trupke, H. F. Powell, D. Sahagun, C. D. J. Sinclair, E. A. Curtis, B. E. Sauer, E. A. Hinds, Z. Moktadir, C. O. Gollasch, and M. Kraft, "Integrated optical components on atom chips," *The European Physical Journal D - Atomic, Molecular, Optical and Plasma Physics*, vol. 35, no. 1, pp. 135–139, Jun. 2005. [Online]. Available: http://link.springer.com/article/10.1140/epjd/e2005-00092-x

[34] J. P. Dowling and J. Gea-Banacloche, "Evanescent light-wave atom mirrors, resonators, waveguides, and traps," in *Advances In Atomic, Molecular, and Optical Physics*, Benjamin Bederson and Herbert Walther, Ed. Academic Press, 1996, vol. Volume 37, pp. 1–94. [Online]. Available: http://www.sciencedirect.com/science/article/pii/S1049250X08600981

[35] F. Le Kien, V. I. Balykin, and K. Hakuta, "Atom trap and waveguide using a two-color evanescent light field around a subwavelength-diameter optical fiber," *Physical Review A*, vol. 70, no. 6, p. 063403, Dec. 2004. [Online]. Available: http://link.aps.org/doi/10.1103/PhysRevA.70.063403

[36] G. Sagué, E. Vetsch, W. Alt, D. Meschede, and A. Rauschenbeutel, "Cold-atom physics using ultrathin optical fibers: Light-induced dipole forces and surface interactions," *Physical Review Letters*, vol. 99, no. 16, p. 163602, Oct. 2007. [Online]. Available: http://link.aps.org/doi/10.1103/PhysRevLett.99.163602

[37] P. Öhberg and L. Santos, "Dynamical transition from a quasi-one-dimensional Bose-Einstein condensate to a Tonks-Girardeau gas," *Physical Review Letters*, vol. 89, no. 24, p. 240402, Nov. 2002. [Online]. Available: http://link.aps.org/doi/10.1103/PhysRevLett.89.240402

[38] M. Girardeau, "Relationship between systems of impenetrable bosons and fermions in one dimension," *Journal of Mathematical Physics*, vol. 1, no. 6, pp. 516–523, Nov. 1960. [Online]. Available: http://jmp.aip.org/resource/1/jmapaq/v1/i6/p516_s1

[39] T. Kinoshita, T. Wenger, and D. S. Weiss, "Observation of a one-dimensional Tonks-Girardeau gas," *Science*, vol. 305, no. 5687, pp. 1125–1128, Aug. 2004. [Online]. Available: http://www.sciencemag.org/content/305/5687/1125.abstract

[40] B. Paredes, A. Widera, V. Murg, O. Mandel, S. Fölling, I. Cirac, G. V. Shlyapnikov, T. W. Hänsch, and I. Bloch, "Tonks-Girardeau gas of ultracold atoms in an optical lattice," *Nature*, vol. 429, no. 6989, pp. 277–281, May 2004. [Online]. Available: http://www.nature.com/nature/journal/v429/n6989/abs/nature02530.html

[41] E. Haller, M. Gustavsson, M. J. Mark, J. G. Danzl, R. Hart, G. Pupillo, and H.-C. Ngerl, "Realization of an Excited, Strongly Correlated Quantum Gas Phase," *Science*, vol. 325, no. 5945, pp. 1224–1227, Sep. 2009. [Online]. Available: http://www.sciencemag.org/content/325/5945/1224

[42] A. Haase, D. Cassettari, B. Hessmo, and J. Schmiedmayer, "Trapping neutral atoms with a wire," *Physical Review A*, vol. 64, no. 4, p. 043405, Sep. 2001. [Online]. Available: http://pra.aps.org/abstract/PRA/v64/i4/e043405

[43] J. Denschlag, D. Cassettari, A. Chenet, S. Schneider, and J. Schmiedmayer, "A neutral atom and a wire: towards mesoscopic atom optics," *Applied Physics B*, vol. 69, no. 4, pp. 291–301, Sep.

1999. [Online]. Available: http://link.springer.com/article/10.1007/s003400050809

[44] S. Hofferberth, I. Lesanovsky, B. Fischer, T. Schumm, and J. Schmiedmayer, "Non-equilibrium coherence dynamics in one-dimensional bose gases," *Nature*, vol. 449, no. 7160, pp. 324–327, Sep. 2007. [Online]. Available: http://www.nature.com/nature/journal/v449/n7160/full/nature06149.html

[45] W. Ketterle, D. Durfee, and S. Kurn, "Making, probing and understanding bose-einstein condensates," in *Bose-Einstein Condensation in Atomic Gases (Proceedings of the International School of Physics "Enrico Fermi," Course CXL)*, M. Inguscio, S. Stringari, and C. Wieman, Eds. IOS Press, 1999.

[46] M. R. Andrews, M.-O. Mewes, N. J. v. Druten, D. S. Durfee, D. M. Kurn, and W. Ketterle, "Direct, Nondestructive Observation of a Bose Condensate," *Science*, vol. 273, no. 5271, pp. 84–87, Jul. 1996. [Online]. Available: http://www.sciencemag.org/content/273/5271/84

[47] J. F. Sherson, C. Weitenberg, M. Endres, M. Cheneau, I. Bloch, and S. Kuhr, "Single-atom-resolved fluorescence imaging of an atomic Mott insulator," *Nature*, vol. 467, no. 7311, pp. 68–72, Sep. 2010. [Online]. Available: http://www.nature.com/nature/journal/v467/n7311/full/nature09378.html

[48] M. Karski, L. Förster, J. M. Choi, W. Alt, A. Widera, and D. Meschede, "Nearest-neighbor detection of atoms in a 1D optical lattice by fluorescence imaging," *Physical Review Letters*, vol. 102, no. 5, p. 053001, Feb. 2009. [Online]. Available: http://link.aps.org/doi/10.1103/PhysRevLett.102.053001

[49] E. Marcatili, "Dielectric rectangular waveguide and directional coupler for integrated optics," *Bell System Technical Journal, The*, vol. 48, no. 7, pp. 2071–2102, Sep. 1969.

[50] A. Macleod, "9 - optical thin films," in *Handbook of Thin Film Deposition (Third Edition)*. William Andrew Publishing, 2012, pp. 271–311. [Online]. Available: http://www.sciencedirect.com/science/article/pii/B9781437778731000097

[51] D. M. Mattox, "Chapter 10 - atomistic film growth and some growth-related film properties," in *Handbook of Physical Vapor Deposition (PVD) Processing (Second Edition)*, D. M. Mattox, Ed. William Andrew Publishing, 2010, pp. 333–398. [Online]. Available: http://www.sciencedirect.com/science/article/pii/B9780815520375000101

[52] B. H. Ong, X. Yuan, S. Tao, and S. C. Tjin, "Photothermally enabled lithography for refractive-index modulation in SU-8 photoresist," *Optics Letters*, vol. 31, no. 10, pp. 1367–1369, May 2006. [Online]. Available: http://ol.osa.org/abstract.cfm?URI=ol-31-10-1367

[53] H. Raether, "Surface plasmons on smooth surfaces," in *Surface Plasmons on Smooth and Rough Surfaces and on Gratings*, ser. Springer Tracts in Modern Physics. Springer Berlin Heidelberg, Jan. 1988, no. 111, pp. 4–39. [Online]. Available: http://link.springer.com/chapter/10.1007/BFb0048319

[54] R. L. Olmon, B. Slovick, T. W. Johnson, D. Shelton, S.-H. Oh, G. D. Boreman, and M. B. Raschke, "Optical dielectric function of gold," *Physical Review B*, vol. 86, no. 23, p. 235147, Dec. 2012. [Online]. Available: http://link.aps.org/doi/10.1103/PhysRevB.86.235147

[55] X.-Q. Sheng and W. Song, *Essentials of Computational Electromagnetics*. John Wiley & Sons, 2012.

[56] A. F. Oskooi, D. Roundy, M. Ibanescu, P. Bermel, J. D. Joannopoulos, and S. G. Johnson, "Meep: A flexible free-software package for electromagnetic simulations by the FDTD method," *Computer Physics Communications*, vol. 181, no. 3, pp. 687–702, Mar. 2010. [Online]. Available: http://www.sciencedirect.com/science/article/pii/S001046550900383X

[57] C. Geuzaine and J.-F. Remacle, "Gmsh: A 3-d finite element mesh generator with built-in pre- and post-processing facilities," *International Journal for Numerical Methods in Engineering*, vol. 79, no. 11, pp. 1309–1331, Sep. 2009. [Online]. Available: http://onlinelibrary.wiley.com/doi/10.1002/nme.2579/abstract

[58] W. Yu and R. Mittra, "A conformal FDTD software package modeling antennas and microstrip circuit components," *IEEE Antennas and Propagation Magazine*, vol. 42, no. 5, pp. 28–39, Oct. 2000.

[59] R. Zia, M. D. Selker, and M. L. Brongersma, "Leaky and bound modes of surface plasmon waveguides," *Physical Review B*, vol. 71, no. 16, p. 165431, Apr. 2005. [Online]. Available: http://link.aps.org/doi/10.1103/PhysRevB.71.165431

[60] R. Zia and M. Brongersma, "Chapter 7 - metal stripe surface plasmon waveguides," in *Nanophotonics with Surface Plasmons*, ser. Advances in Nano-Optics and Nano-Photonics, V. M. S. Kawata, Ed. Elsevier, 2007, pp. 191–218. [Online]. Available: http://www.sciencedirect.com/science/article/pii/B9780444528384500084

[61] R. Zia, J. A. Schuller, and M. L. Brongersma, "Near-field characterization of guided polariton propagation and cutoff in surface plasmon waveguides," *Physical Review B*, vol. 74, no. 16, p. 165415, May 2006. [Online]. Available: http://link.aps.org/doi/10.1103/PhysRevB.74.165415

[62] J. J. P. v. Es, P. Wicke, A. H. v. Amerongen, C. Rétif, S. Whitlock, and N. J. v. Druten, "Box traps on an atom chip for one-dimensional quantum gases," *Journal of Physics B: Atomic, Molecular and Optical Physics*, vol. 43, no. 15, p. 155002, Aug. 2010. [Online]. Available: http://iopscience.iop.org/0953-4075/43/15/155002

[63] D. Steck, "Rubidium 87 d line data." [Online]. Available: http://george.ph.utexas.edu/~dsteck/alkalidata/rubidium87numbers.pdf

[64] A. H. van Amerongen, "One-dimensional Bose gas on an atom chip," *Annales de Physique*, vol. 33, no. 3, pp. 1–94, Feb. 2009. [Online]. Available: http://www.annphys.org/index.php?option=com_article\&access=doi\&doi=10.1051/anphys/2009001\&Itemid=129l

[65] T. Meyrath, F. Schreck, J. Hanssen, C. Chuu, and M. Raizen, "A high frequency optical trap for atoms using Hermite-Gaussian beams," *Optics express*, vol. 13, no. 8, pp. 2843–2851, Apr. 2005.

[66] H. G. Vaidya and C. A. Tracy, "One particle reduced density matrix of impenetrable bosons in one dimension at zero temperature," *Journal of Mathematical Physics*, vol. 20, no. 11, pp. 2291–2312, Nov. 1979. [Online]. Available: http://jmp.aip.org/resource/1/jmapaq/v20/i11/p2291_s1

[67] K. Huang and C. N. Yang, "Quantum-mechanical many-body problem with hard-sphere interaction," *Physical Review*, vol. 105, no. 3, pp.

767–775, Feb. 1957. [Online]. Available: http://link.aps.org/doi/10.1103/PhysRev.105.767

[68] E. H. Lieb and W. Liniger, "Exact analysis of an interacting Bose gas. I. The general solution and the ground state," *Physical Review*, vol. 130, no. 4, pp. 1605–1616, May 1963. [Online]. Available: http://link.aps.org/doi/10.1103/PhysRev.130.1605

[69] E. H. Lieb, R. Seiringer, and J. Yngvason, "One-dimensional bosons in three-dimensional traps," *Physical Review Letters*, vol. 91, no. 15, p. 150401, Oct. 2003. [Online]. Available: http://link.aps.org/doi/10.1103/PhysRevLett.91.150401

[70] E. Verhagen, A. Polman, and L. K. Kuipers, "Nanofocusing in laterally tapered plasmonic waveguides," *Optics Express*, vol. 16, no. 1, p. 45, Jan. 2008. [Online]. Available: http://www.opticsinfobase.org/abstract.cfm?URI=oe-16-1-45

[71] E. Verhagen, M. Spasenovi, A. Polman, and L. K. Kuipers, "Nanowire plasmon excitation by adiabatic mode transformation," *Physical Review Letters*, vol. 102, no. 20, p. 203904, May. [Online]. Available: http://link.aps.org/doi/10.1103/PhysRevLett.102.203904

[72] D. E. Chang, J. D. Thompson, H. Park, V. Vuletić, A. S. Zibrov, P. Zoller, and M. D. Lukin, "Trapping and manipulation of isolated atoms using nanoscale plasmonic structures," *Physical Review Letters*, vol. 103, no. 12, p. 123004, Sep. 2009. [Online]. Available: http://link.aps.org/doi/10.1103/PhysRevLett.103.123004